

AD A 038870

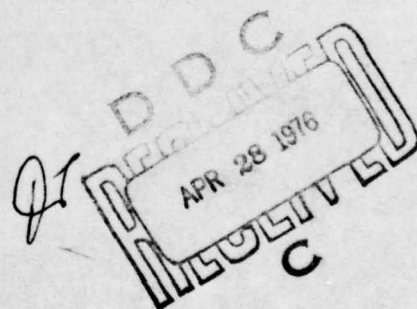
RADC-TR-77-73
Final Report



**MULTIPATH DISPERSION IN LOW VISIBILITY
OPTICAL COMMUNICATION CHANNELS**

**Research Laboratory of Electronics
Massachusetts Institute of Technology**

Approved for public release;
distribution unlimited.



AD No. _____
DDC FILE COPY

**ROME AIR DEVELOPMENT CENTER
AIR FORCE SYSTEMS COMMAND
GRIFFISS AIR FORCE BASE, NEW YORK 13441**

This technical report has been reviewed and approved for publication.

APPROVED:

DALLAS HAYES

APPROVED:

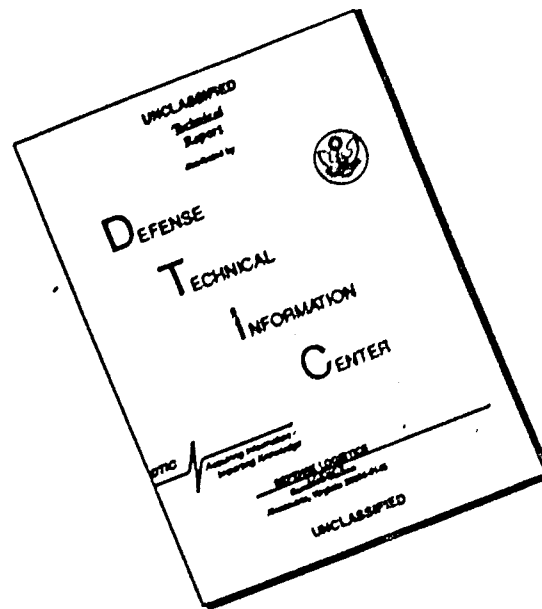
ALLAN C. SCHELL
Acting Chief
Electromagnetic Sciences Division

FOR THE COMMANDER:

Plans Office

ACCESSION for		White Section	<input type="checkbox"/>
NTIS	DOC	Both Section	<input type="checkbox"/>
UNANNOUNCED			
JUSTIFICATION			
BY			
DISTRIBUTION AVAILABILITY CODES			
DECL		APPL	DECL
A			

DISCLAIMER NOTICE



THIS DOCUMENT IS BEST QUALITY AVAILABLE. THE COPY FURNISHED TO DTIC CONTAINED A SIGNIFICANT NUMBER OF PAGES WHICH DO NOT REPRODUCE LEGIBLY.

Unclassified

RADC/OI 77-102

SECURITY CLASSIFICATION OF THIS PAGE (When Data Entered)

19 REPORT DOCUMENTATION PAGE		READ INSTRUCTIONS BEFORE COMPLETING FORM	
1. REPORT NUMBER RADC-TR-77-73	2. GOVT ACCESSION NO.	3. RECIPIENT'S CATALOG NUMBER	
4. TITLE (and Subtitle) MULTIPATH DISPERSION IN LOW VISIBILITY OPTICAL COMMUNICATION CHANNELS.		5. TYPE OF REPORT & PERIOD COVERED Final Report, 1 Jul 75-30 Sep 76	
7. AUTHOR(s) R. S. Kennedy and J. H. Shapiro		6. PERFORMING ORG. REPORT NUMBER	
9. PERFORMING ORGANIZATION NAME AND ADDRESS Research Laboratory of Electronics Massachusetts Institute of Technology Cambridge, Mass. 02139		8. CONTRACT OR GRANT NUMBER(s) Contract F19628-76-C-0054	
11. CONTROLLING OFFICE NAME AND ADDRESS Deputy for Electronic Technology (RADC/ETEP) Hanscom AFB MA 01731 Monitor/Dallas Hayes		10. PROGRAM ELEMENT, PROJECT, TASK AREA & WORK UNIT NUMBERS 61102F 21530202 1702	
14. MONITORING AGENCY NAME & ADDRESS (if different from Controlling Office)		12. REPORT DATE 11 February 1977	
		13. NUMBER OF PAGES 92 1289p.	
		15. SECURITY CLASS. (of this report) Unclassified	
		15a. DECLASSIFICATION/DOWNGRADING SCHEDULE	
16. DISTRIBUTION STATEMENT (of this Report) Approved for public release; distribution unlimited			
17. DISTRIBUTION STATEMENT (of the abstract entered in Block 20, if different from Report)			
18. SUPPLEMENTARY NOTES			
19. KEY WORDS (Continue on reverse side if necessary and identify by block number) Optical communication Low visibility communication Optical scatter Time dispersion Multiple scatter Atmospheric optics Transport equation			
20. ABSTRACT (Continue on reverse side if necessary and identify by block number) The potential for optical communication through low-visibility scattering atmospheres is the underlying concern of this investigation. To access that potential, the effects of the channel upon the optical signal propagating through it must be determined. The work reported here is primarily concerned with one of those effects: the time dispersion, or multipath spread, of the transmitted signal. The investigation was primarily an experimental one, utilizing the existing propagation facility operating over a thirteen kilometer experimental path.			

DD FORM 1473 1 JAN 73

EDITION OF 1 NOV 65 IS OBSOLETE
S/N 0102-014-6601

Unclassified

SECURITY CLASSIFICATION OF THIS PAGE (When Data Entered)

304050


over
Jmcc

20.

between the MIT campus and a field station located at an Air Force site in suburban Boston. Experiments were performed at visible and near infrared wavelengths, with highly collimated transmitting beams. Measurements of the multipath spread for various receiver fields of view and at various off-axis angles were made.

Little multipath and angular spread was observed within the realm of atmospheric conditions for which a detectable signal could be obtained. For optical thicknesses less than ten, the on-axis measurements are consistent with the hypothesis that the received signal is dominated by unscattered radiation; however, the off-axis measurements suggest that the scattered field itself may be only slightly spread in time and angle.

Guided by the observed narrowness of the angular spectrum, an approximation to the linear transport equation was developed. The resulting equation is more amenable to solution than is the full transport equation. Here it is solved for isotropic scatter. For such scattering it is found that substantial spreading in both time and angle will occur when the optical thickness becomes appreciably greater than one. This, in combination with the data collected, suggests that nonisotropic scattering encountered in the atmosphere is responsible for the absence of spreading.

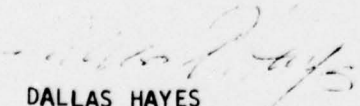


Unclassified

EVALUATION

1. This report is the Final Report on the contract. It covers research done on optical communication channels during the 15 month period 1 July 1975 to 30 September 1976. The objective of the research is to determine the effect of low-visibility scattering atmospheres upon optical signals. There exists the potential for improving the operability of line-of-sight optical communication links by exploiting the scattered component of the received optical signal in addition to the unscattered part. Experiments were conducted under this contract to determine the basic properties of the scattered part of the transmitted optical signal.

2. The above work is of value since it provides basic knowledge on optical communication channels under low-visibility conditions which will allow the scattered part of the transmitted signal to be useful in communication links in addition to the unscattered part. This research may make the development of new more sensitive optical receivers possible which will increase the range of optical communication channels designed for USAF use.


DALLAS HAYES
Project Engineer
Microwave Detection Techniques
Electromagnetics Sciences Division

SUMMARY

The potential for optical communication through low-visibility scattering atmospheres is the underlying concern of this investigation. To access that potential, the effects of the channel upon the optical signal propagating through it must be determined. The work reported here is primarily concerned with one of those effects: the time dispersion, or multipath spread, of the transmitted signal.

The investigation was primarily an experimental one, utilizing the existing propagation facility operating over a thirteen kilometer experimental path between the MIT campus and a field station located at an Air Force site in suburban Boston. Experiments were performed at visible and near infrared wavelengths, with highly collimated transmitting beams. Measurements of the multipath spread for various receiver fields of view and at various off-axis angles were made.

Little multipath and angular spread was observed within the realm of atmospheric conditions for which a detectable signal could be obtained. For optical thicknesses less than ten, the on-axis measurements are consistent with the hypothesis that the received signal is dominated by unscattered radiation; however, the off-axis measurements suggest that the scattered field itself may be only slightly spread in time and angle.

Guided by the observed narrowness of the angular spectrum, an approximation to the linear transport equation was developed. The resulting equation is more amenable to solution than is the full transport equation. Here it is solved for isotropic scatter. For such scattering it is found that substantial spreading in both time and angle will occur when the optical thickness becomes appreciably greater than one. This, in combination with the data collected, suggests that nonisotropic scattering encountered in the atmosphere is responsible for the absence of spreading.

TABLE OF CONTENTS

	<u>Page</u>
SUMMARY	iii
LIST OF TABLES	v
LIST OF FIGURES	vi
LIST OF PERSONNEL	viii
CHAPTER I. INTRODUCTION	1
CHAPTER II. EXPERIMENTS	5
A. Propagation-Link Specifications	5
1. Ruby Link	5
2. Holmium Link	10
3. Synchronization Link	13
B. Propagation-Link Predictions	14
1. Lincoln Laboratory Simulation	14
2. Transmission-Fraction Analysis	17
C. Propagation-Link Measurements	23
1. Multipath and Angular Spread	24
2. Transmission-Fraction Comparison	24
CHAPTER III. A THEORETICAL APPROACH	44
A. The Transport Equation	44
1. Formulation	45
2. The Channel Frequency Response	46
B. An Approximation to the Transport Equation	48
1. A Narrow Spectrum Approximation	48
2. The Solution for $P(\vec{r}, s)$ and $P(\vec{r}, \vec{\Omega}, s)$	51
C. Isotropic Scatter	54
1. Isotropic Point Source	54
2. Ray Source	63
3. The Angular Spectrum	66
References	68
APPENDIX I	71

LIST OF TABLES

<u>Number</u>		<u>Page</u>
1	Diffusion-Regime Multipath Predictions	22
2	Ruby Laser Multipath Observations	26
3	Ruby Laser Transmission Data	36
4	Holmium Laser Transmission Data: 1 mRad FOV	37
5	Holmium Laser Transmission Data: 20 mRad FOV	38

LIST OF FIGURES

<u>Number</u>		<u>Page</u>
1	Profile of terrain along propagation path.	6
2	View from top of M. I. T.'s Earth Sciences Building looking across Cambridge toward test site on Prospect Hill, Waltham.	7
3	View from Waltham test site looking towards M. I. T. and downtown Boston.	8
4	Ruby-link block diagram.	9
5	Receiver telescope and associated electronics for the ruby link.	11
6	Holmium-link block diagram.	12
7	Timing jitter measurement.	15
8	Receiver-plane transmission fractions.	19
9	Receiver-pupil transmission fractions.	20
10	Receiver focal-plane transmission fractions.	21
11	Clear-weather ruby pulse.	25
12	Type ii ruby pulse.	25
13	Type iii ruby pulse.	25
14	Clear-weather ruby link signal vs receiver field of view.	28
15	Clear-weather holmium link signal vs receiver field of view.	29
16	Low-visibility ruby link signal vs receiver field of view.	30
17	Low-visibility ruby link signal vs receiver field of view.	31
18	Low-visibility holmium link signal vs receiver field of view.	32
19	Low-visibility holmium link signal vs receiver field of view.	33
20	Low-visibility holmium link signal vs receiver field of view, with transmitter aimed up 4 mRad.	35

<u>Number</u>		<u>Page</u>
21	Ruby-link signal vs optical thickness (based on Table 3).	39
22	Holmium-link signal vs optical thickness (based on Table 4).	40
23	Holmium-link signal vs optical thickness (based on Table 5).	41
24	Conditions for which $P(\vec{r}, \vec{\Omega}, 0)$ will be narrow. At each point $\vec{r} - \nu \vec{\Omega}$ outside the shaded region, either $\vec{\Omega}_{\vec{r}}$ and $\vec{\Omega}$ must differ by more than θ_s or $P(\vec{r} - \nu \vec{\Omega}, 0)$ must be approximately zero.	50
25	The exponent η versus β/a for $\omega_m = 0$.	58
26	The cutoff frequency $\omega_c/\beta c$ versus β/a .	59
27	The real part of η as a function of $\omega_m/(c\beta)$ for $(\alpha-\beta)/\beta = 0, 0.04$, and 0.11 .	60
28	The imaginary part of η as a function of $\omega_m/(c\beta)$ for $(\alpha-\beta)/\beta = 0, 0.4$, and 0.11 .	61
29	The imaginary part of η as a function of $\omega_m/(c\beta)$ for $(\alpha-\beta)/\beta = 0.04$ and 0.11 .	62
I-1	Contour of integration in the cut plane.	72
I-2	Locus of $[2j(\omega/\gamma)]^{-1} \ln \{ [1 + (j\omega/\gamma)]/[1 - (j\omega/\gamma)] \}$ for ω on the contour of Fig. I-1.	75

LIST OF PERSONNEL

Faculty and Research Staff

D. J. Epstein
H. P. Jenssen
R. S. Kennedy

A. Linz
J. H. Shapiro
C. Warde

Graduate Students

S. L. Bates
J. A. Machado Mata
P. Moroney
N. S. Myung

W. H. Paik
W. S. Ross
S. V. Sperry
M. Tebyani

CHAPTER I. INTRODUCTION

The apparent limitations imposed upon atmospheric optical communication systems by low-visibility weather conditions (haze, rain, fog, snow, etc.) have been widely noted. In particular, for a conventional line-of-sight link, whose receiver responds only to the unscattered light arriving along the boresight from the transmitter, the major effect of low-visibility atmospheric propagation is to increase the path loss by a factor of $\exp(-\alpha L)$, where L is the path length and α is the extinction coefficient of the atmosphere at the wavelength of interest. Although the relationship between α and visibility is tenuous, at best, some appreciation for the magnitude of the attenuation is provided by the commonly accepted approximation that, at visible wavelengths, $\exp(-\alpha L)$ will be on the order of 10^{-2} when the operating range L equals the visibility [1, 2].

At most visible wavelengths, and at many infrared wavelengths, the extinction coefficient α is due in large measure to scattering rather than absorption [3, 4]. Thus, there exists the potential for improving the operability of line-of-sight optical links by exploiting the scattered component of the received optical field, in addition to the unscattered component [5-8]. The extent to which utilization of scattered light will significantly improve low-visibility communication performance depends upon the energy contained in the scattered component of the received field and upon the way in which this energy is divided between the statistical degrees of freedom of the field. These quantities are, in turn, related to the characteristics of the scattering particles and to the geometry of the channel in a very complicated way. Nevertheless, some basic features can be discerned.

It is reasonable to assume that when multiple-scattering effects predominate, as it is likely they will in a low-visibility atmospheric channel, the optical complex field envelopes received on two orthogonal polarizations will be independent identically-distributed zero-mean complex-Gaussian random processes whose statistics are completely characterized by a space-time correlation function [9-11]. When the particle scattering function is sharply peaked in the forward direction, various analytic techniques (which have been used to study wave propagation through atmospheric turbulence) may be applied to explicitly determine the desired space-time correlation function [12, 13]. At

present, however, multiple-scattering theory is too complicated to permit such an explicit determination in the general case, wherein the forward-scattering assumption is no longer applicable [9-11].

Fortunately, previous experience with radio-frequency scattering channels suggests that detailed knowledge of the channel correlation function may not be necessary. In particular, specification of "physical" parameters such as multipath spread (time dispersion), Doppler spread (frequency dispersion), and angular spread (spatial-frequency dispersion) can suffice for both the design of receiver structures and performance calculations [5, 14]. Indeed, based on reasonable, but as yet unverified, statistical assumptions, two possible receiver structures for exploiting the information contained in the scattered field have been identified [5, 6, 8].

The first structure is a wide field-of-view direct detection system that counts photon arrivals in the entire time-frequency-spatial frequency region over which scattered signal light is expected. The performance obtainable with this receiver will depend critically upon the development of improved wide-angle narrow-band optical filters to discriminate against background light, or operation at wavelengths where such light is negligible. Under favorable conditions, the direct-detection performance can approximate that of the optimum one-shot quantum-mechanical receiver. The second candidate receiver is a spatial phase-compensation (mode-compression) receiver, similar to systems previously recommended for atmospheric turbulence (clear-weather) applications [15-17], but with many more phase-controllable elements. The theoretical utility of mode compression rests on the assumptions that channel fluctuations occur slowly relative to the desired information rate, and that the uncompensated system is background-limited. The practicality of the phase-compensation receiver will depend upon the ease with which a large number of phase elements may be reliably estimated and controlled.

In the context of the foregoing receiver structures, the importance of the channel spread parameters (multipath, Doppler, etc.) is apparent, and the need for experimental measurements manifest. The degree to which these receivers will extend the operability of atmospheric links depends overwhelmingly on the degree to which, under low-visibility conditions, the energy contained in the scattered component of the received field substantially exceeds the energy contained in the unscattered component. For example, it can be argued that for a

beam source embedded in an infinite lossless homogeneous scattering medium, the received energy at path length L will, as visibility decreases, ultimately reduce to the level of a free-space omnidirectional radiator. Whether or not the scattered-field energy still dominates the unscattered energy by a wide margin in the more typical case of a partially absorbing inhomogeneous scattering medium with boundaries, remains to be determined (cf. Chap. II).

Given that there is sufficient energy in the scattered field to warrant the use of a low-visibility (wide field-of-view or mode-compression) receiver, the ease with which such a system may be implemented depends, primarily, on the angular spread of the scattered light. This angular spread must be accommodated by the optical filter in the wide field-of-view receiver. This angular spread, measured in units of diffraction-limited fields of view, determines the required number of phase controllers in the mode-compression receiver. In either case, the implementation burden is an increasing function of angular spread.

Finally, assuming that a substantial amount of scattered energy can be collected over an acceptable (vis-a-vis implementation) field of view, the primary limitation on the two candidate low-visibility receivers may be due to multipath spread. In particular, to achieve data rates in excess of the reciprocal multipath spread for the full (uncompensated) receiver field of view requires an additional level of system complexity to overcome intersymbol interference. Moreover, because multipath spreads in excess of one microsecond have been measured in a cloud propagation experiment [18, 19], the data rate constraint on simple receivers may be severe.

The preceding considerations have led us to make the nature of the scattered-energy distribution a central concern of our ongoing experimental and theoretical research on the possibilities for improved optical communication in low-visibility environments [6, 20]. The objectives of the experimental program have been to:

- 1) measure the ratio of scattered to unscattered radiation collected by a receiver as a function of its field of view, and meteorological conditions;
- 2) measure the angular spectra of pulsed and cw optical signals as functions of meteorological conditions;
- 3) measure the multipath spread of pulsed optical signals as a function of

- meteorological conditions; and
- 4) measure the Doppler spread of cw optical signals as a function of meteorological conditions.

The approach taken in the theoretical work has been to solve the linear-transport equation, subject to approximations motivated by experimental results, for the parametric dependence of angular spread, beam spread, and multipath spread on the total extinction, albedo, particle scattering function, and source geometry.

We shall report here on the experimental and theoretical studies of multipath spread. These studies were funded by the Air Force Electronic Systems Division under Contract F 19628-76-C-0054 [21].

CHAPTER II. EXPERIMENTS

As previously noted, multiple-scattering theory (in its present state) does not provide an explicit determination of the critical spread parameters which characterize the low-visibility atmospheric channel. We have therefore been pursuing, under National Science Foundation and Air Force Electronic Systems Division funding [21, 22], an experimental program aimed at measuring these spread parameters. In this chapter, our multipath measurements will be discussed beginning with a description of the propagation geometry and measurement apparatus.

A. Propagation-Link Specifications

The multipath data reported in the sequel was obtained on a propagation facility established under NSF funding over a 13.6 km line-of-sight path between the optical communications laboratory atop the Earth Sciences building at M.I.T. and the Air Force Millimeter-Wave Observatory atop Prospect Hill in Waltham Mass. The latter location has been made available to us through the generous cooperation of Dr. E. E. Altshuler and his group at the Deputy for Electronic Technology. A profile of the terrain along the path is shown in Fig. 1, and photographs of the views along the path from each terminal are shown in Figs. 2 and 3.

This propagation facility comprises four links utilizing continuous-wave helium neon, pulsed ruby, and pulsed holmium lasers. Multipath measurements were made exclusively with the ruby link. However, important corroborating evidence was obtained from holmium-link angular spectra. These two links are described below.

1. Ruby Link

A block diagram of the ruby link is shown in Fig. 4. The transmitter is a Q-switched Spacerays ruby laser, which is located at M. I. T. This laser delivers pulses of nominal 0.5 J energy and 70 nsec duration at a rate of 10 per minute. The transmitter beam divergence is controlled by a beam-expansion telescope. Initial measurements were made with a 1.8 mRad full width to half maximum (FWHM) beam divergence; the telescope was later modified to yield

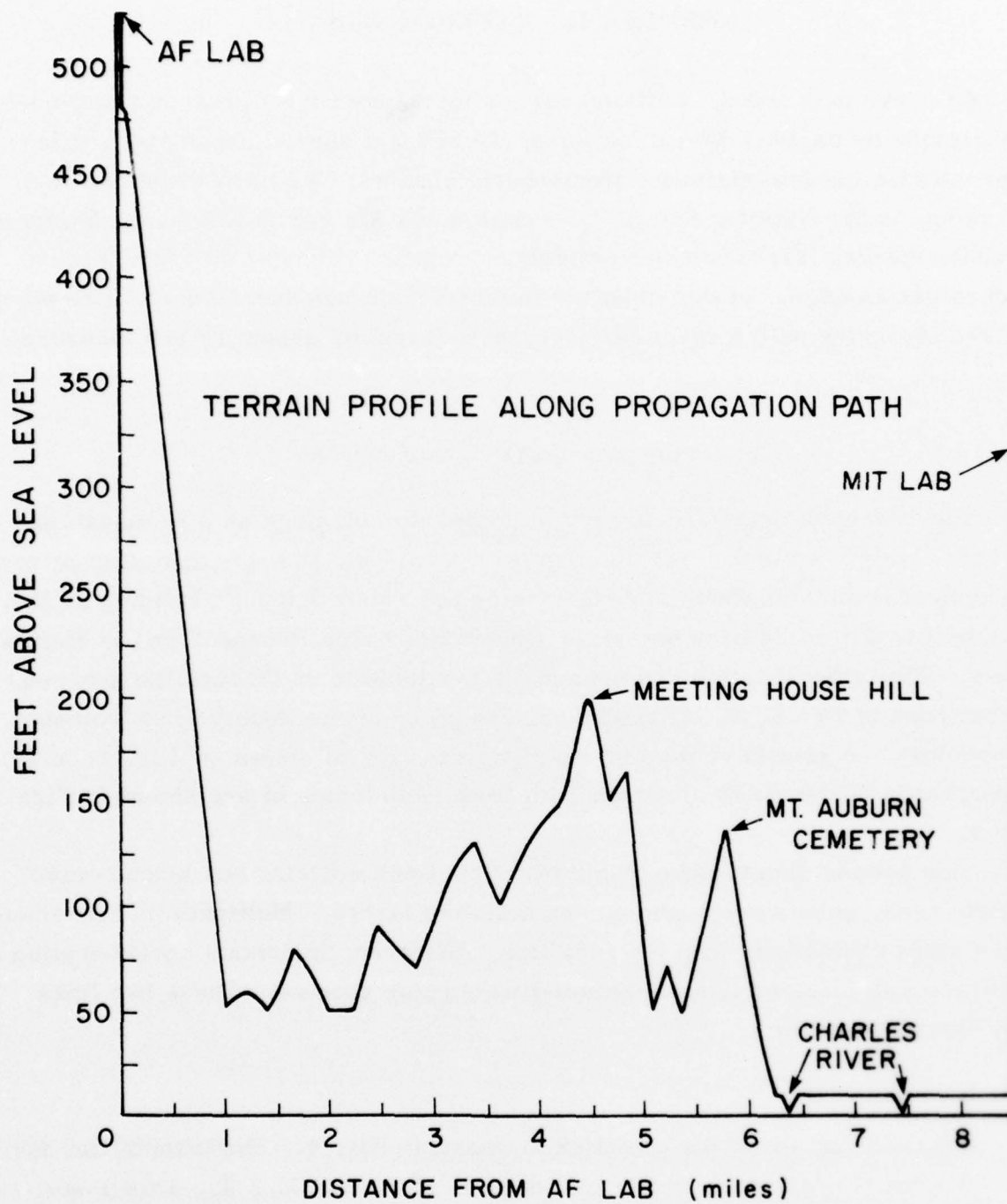


Fig. 1. Profile of terrain along propagation path.

Waltham Test Site

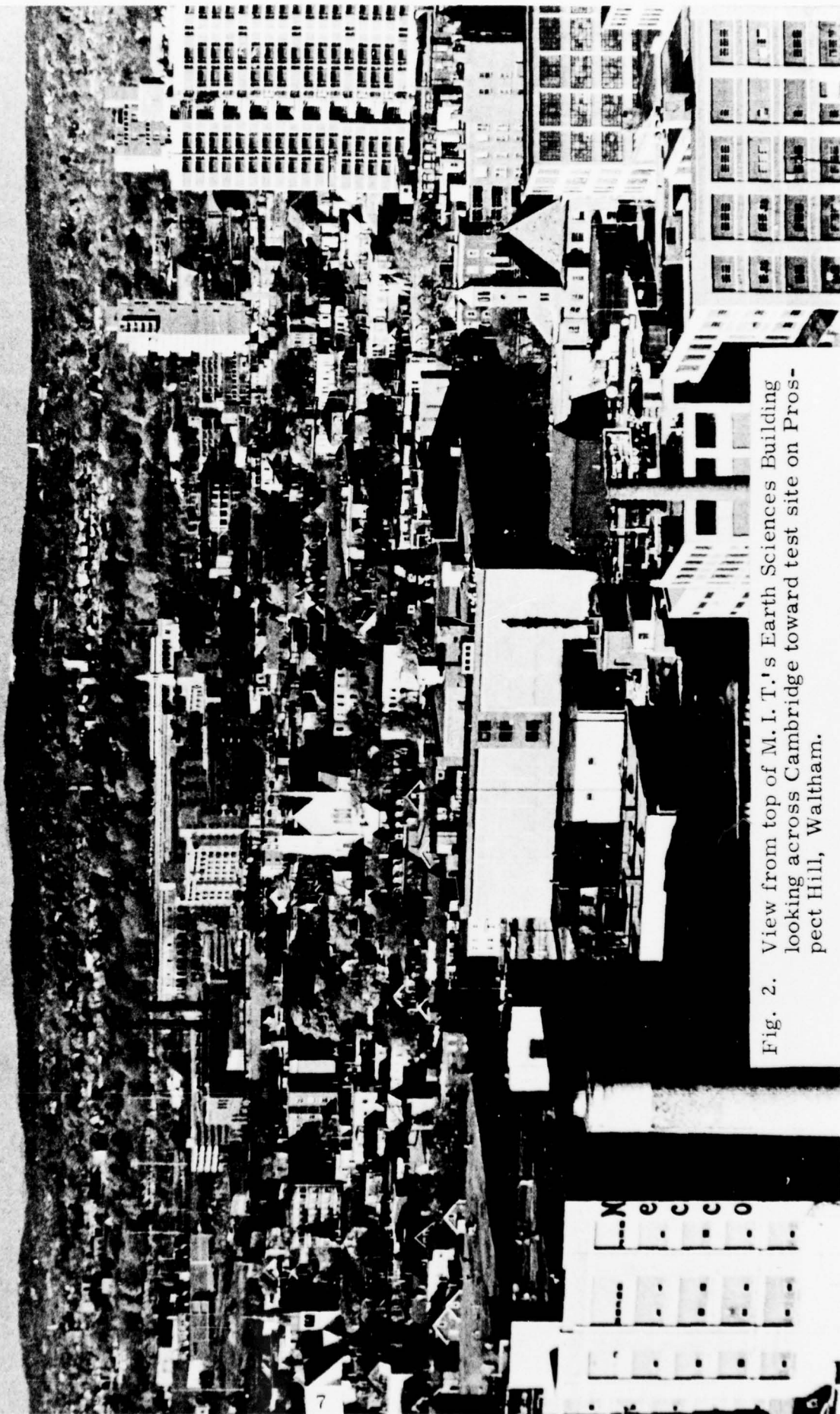


Fig. 2. View from top of M. I. T.'s Earth Sciences Building looking across Cambridge toward test site on Prospect Hill, Waltham.

M.I.T. Test Site

Fig. 3. View from Waltham test site looking towards M. I. T. and downtown Boston.

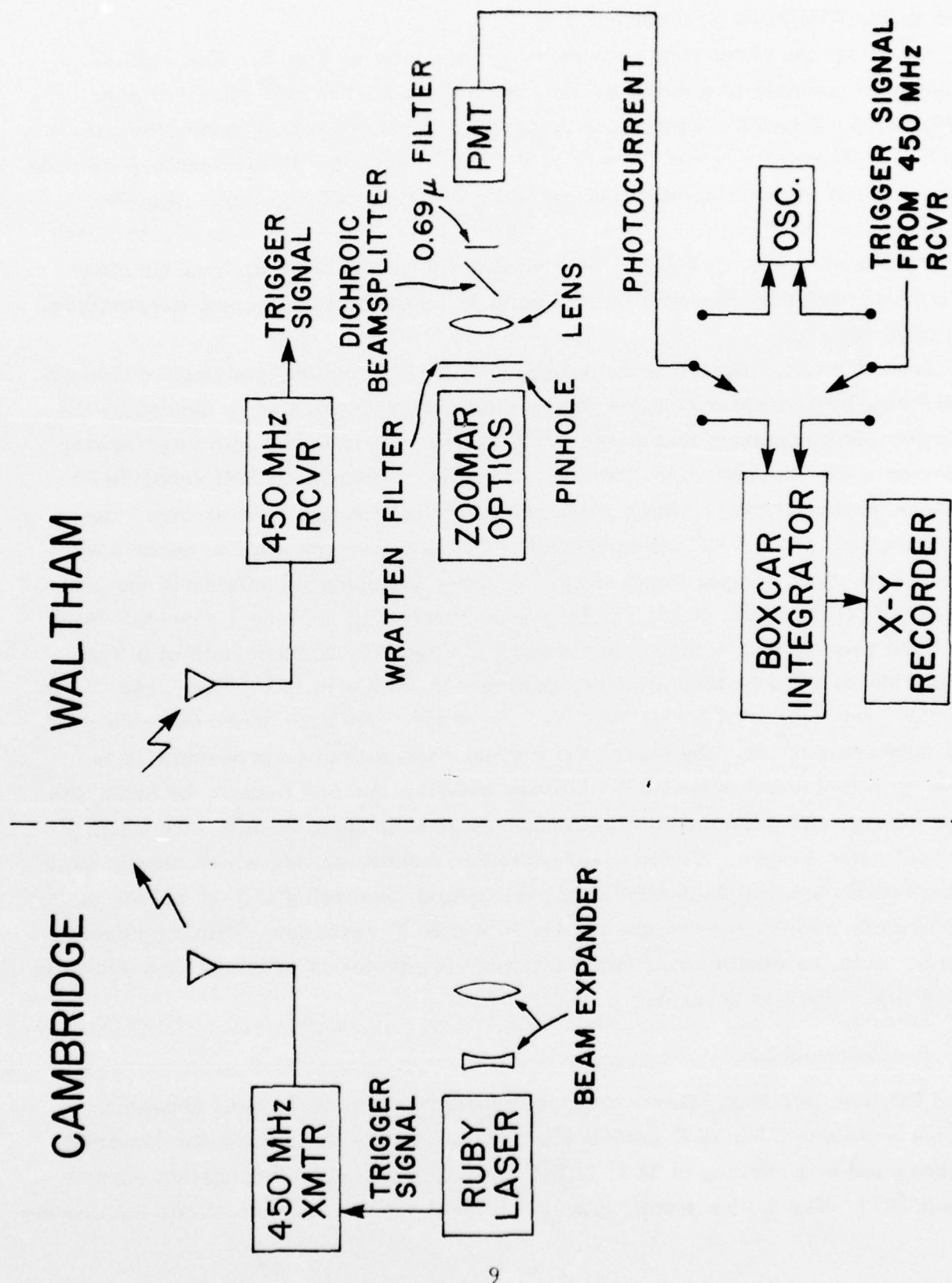


Fig. 4. Ruby-link block diagram.

a 10 mRad FWHM beam divergence.

A photograph of the ruby-link receiver is shown in Fig. 5. The optical subsystem consists of a modified Zoomar telescope (127 cm^2 effective aperture, $f/3.5$, Schmidt-Cassegrain) mounted on a pair of rotary tables for azimuth and elevation control. These tables are equipped with electronic resolvers which permit absolute aiming and resetting to 0.1 mRad. Pinholes may be inserted into the focal plane to select fields of view from 0.1 mRad to 20 mRad full cone angle. Kodak Wratten neutral density filters are employed (in clear-to modest-visibility weather) at this point in the system to prevent overloading the photodetector.

After the focal plane, the ruby light is recollimated and transmitted through a dichroic beamsplitter (which enables the telescope optics to be shared by the holmium-link receiver) and a 1 nm linewidth 694.3 nm wavelength interference filter onto the photodetector. The ruby receiver employs an EMI 9558B S-20 cathode photomultiplier which has a responsivity of 0.018 A/W at 694.3 nm and a current gain of 10^6 (as operated). The detector has a mean anode dark current (at room temperature) of 10^{-9} A, and, including the effects of the post-detection electronics, yields single-photon events with a 30 nsec rise-fall time.

The post-detection signal processing for the ruby link consists of a Tektronix Model 466 100 MHz storage oscilloscope, and a P. A. R. Model 162 boxcar integrator with Model 9002 X-Y recorder. Because of the extremely low duty cycle of the ruby laser, the normal data-collection procedure is to view each individual pulse on the storage oscilloscope and record, by hand, the peak voltage and time duration. Permanent photographic records are made of unusual pulse shapes. Under severe weather conditions, for which oscilloscope observations are insufficiently sensitive, boxcar averaging of 5-20 pulses is performed, and the results are plotted by the X-Y recorder. Timing information for both the oscilloscope and the boxcar integrator is provided by a 450 MHz radio link, which is described in section A. 3.

2. Holmium Link

The holmium link, shown in block diagram in Fig. 6, is built around a 2.06μ wavelength Ho:YLF pulsed laser developed by the Center for Materials Science and Engineering at M. I. T. for use in atmospheric propagation experiments [23]. The 2.06μ wavelength has several virtues for optical communication

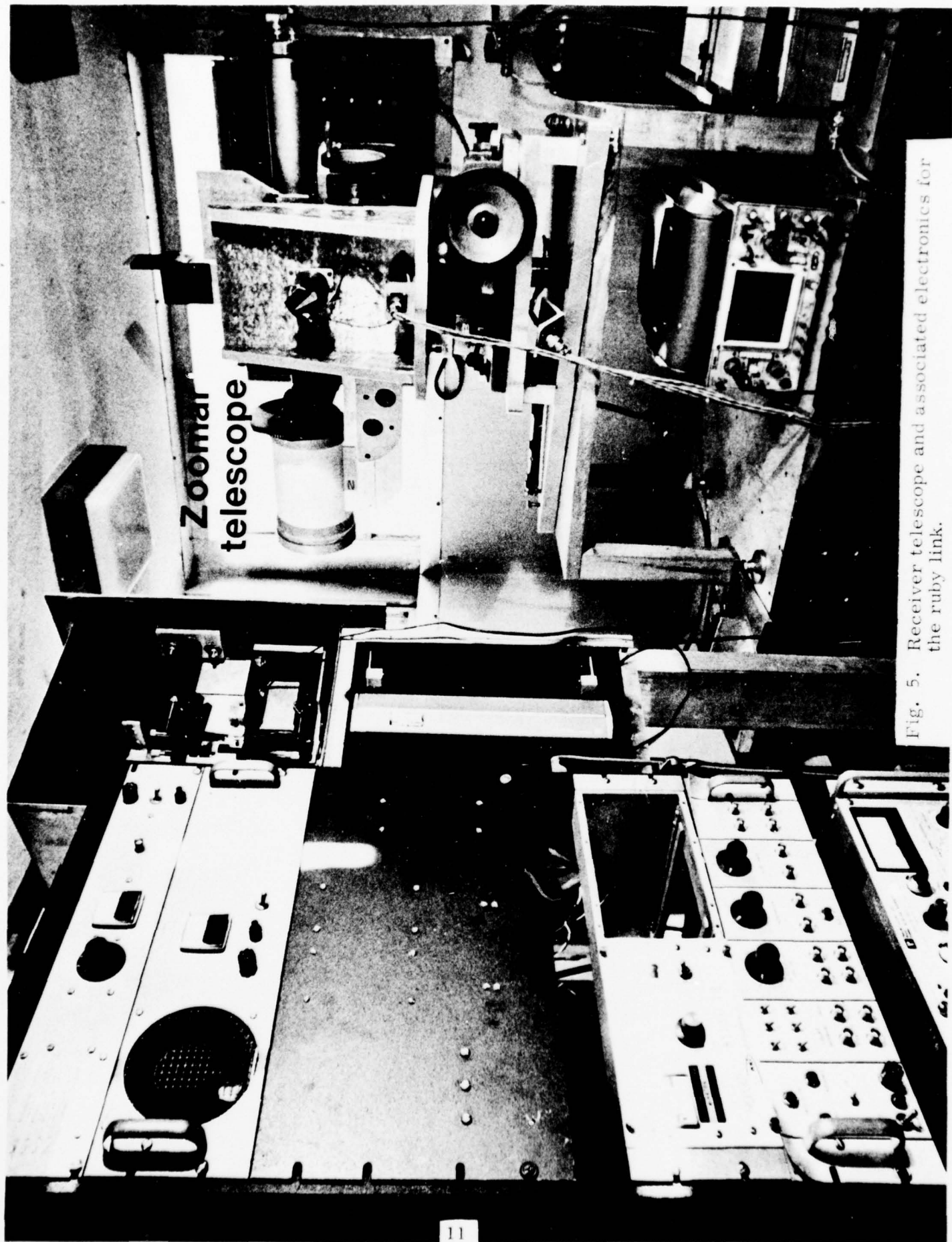
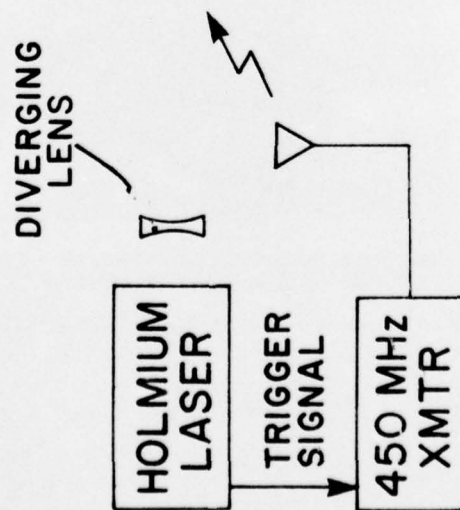


Fig. 5. Receiver telescope and associated electronics for the ruby link.

CAMBRIDGE



WALTHAM

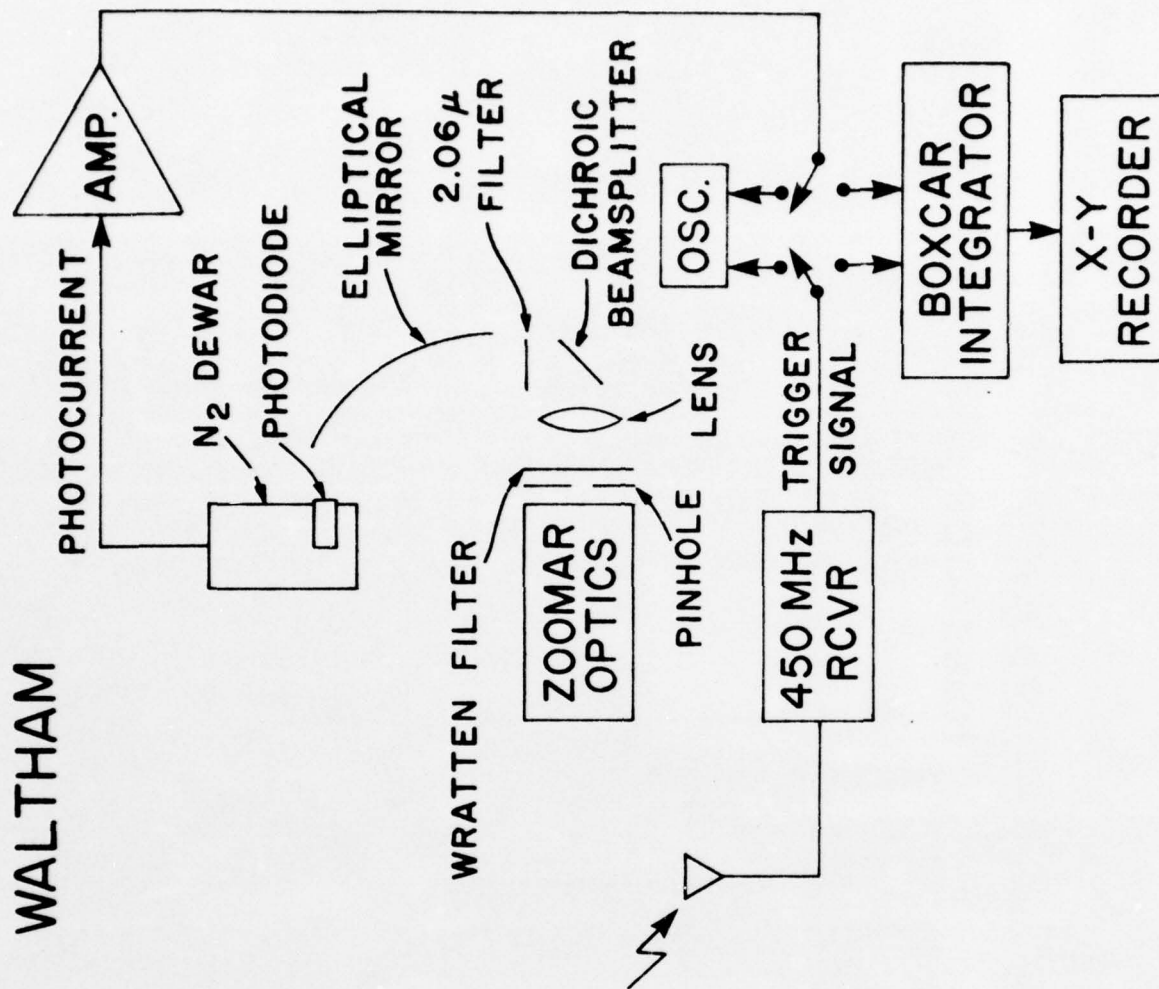


Fig. 6. Holmium-link block diagram.

in the atmosphere. Most notably, because this wavelength is strongly absorbed by the cornea and aqueous humor of the eye, it is relatively "eyesafe" in that the energy brought to focus on the retina is reduced considerably compared, for example, to the $1.06\ \mu$ wavelength radiation of a Nd:YAG laser. The holmium laser used in the propagation studies is located at M. I. T., and operates in the long-pulse mode. It delivers pulses of nominal energy 0.1 J and 150 μ sec duration at a rate of 5 per second. Early measurements were made using the 2 mRad FWHM natural beam divergence of the laser. Later measurements were made, using a diverging lens, with a 5.5 mRad FWHM beam divergence.

The holmium-link receiver shares its principal optical components and post-detection signal processing with the ruby-link receiver. Specifically, the holmium light is brought to focus by the Zoomar optics, with the same azimuth, elevation, and field of view control cited in section A.1. In clear to modest visibility weather, Kodak Wratten neutral density filters (which have been calibrated at $2.0\ \mu$ wavelength) are inserted in the focal plane to prevent overloading the photodetector. After the focal plane, the holmium light is recollimated, and reflected by the dichroic beamsplitter through a 33.5 nm linewidth, $2.06\ \mu$ wavelength interference filter off a 6:1 demagnification elliptical mirror and onto the photodetector. The holmium receiver uses a Judson J-12 InAs photodiode mounted in a liquid nitrogen dewar. This detector has a responsivity of 0.12 A/W at $2.06\ \mu$ and a 1.0 μ sec time constant. Its output is coupled to a low-noise preamplifier whose nominal current gain is 10^6 , and whose root mean square (RMS) noise current is 1 mA (both measurements made with a 50 ohm load). The preamplifier output may be monitored on the Tektronix 466 oscilloscope. Normal data taking procedure, however, involves boxcar averaging of 20 pulses and X-Y recording; longer pulse trains are averaged in the poorest visibility weather. Synchronization is provided by the 450 MHz radio link described below.

3. Synchronization Link

Timing information for both the ruby and holmium links is provided by a 450 MHz radio link [24], which consists of two Motorola U44 transceivers modified for pulsed operation. Trigger pulses from either laser are transmitted from Cambridge to Waltham. A transmitter output power of approximately one watt and six-element Yagi antennas at both ends of the line-of-sight path give a

signal-to-noise ratio in excess of 20 dB prior to pulse regeneration. The use of regulated power supplies at both terminals renders long-term timing drift negligible after a 30 minute warmup period. The short-term timing jitter has been measured at ± 100 nsec or less (see Fig. 7). For the ruby link, the sync pulse arrives approximately 3 μ sec before the optical pulse; for the holmium link, the sync pulse arrives approximately 240 μ sec before the optical pulse.

B. Propagation-Link Predictions

The impetus for propagation experiments derives from the dearth of available theoretical or experimental results for the crucial atmospheric spread parameters. Perhaps the only prior effort at characterizing a low-visibility optical communication channel was the work done on cloud propagation channels by Bucher et al. at the M. I. T. Lincoln Laboratory [18, 19, 25]. This program, which sought to determine the viability of satellite optical-frequency downlinks in the presence of cloud cover at the ground station, included a cloud-propagation experiment and a Monte-Carlo cloud-propagation computer simulation. In this section we shall apply the scaling laws obtained in the foregoing computer simulation in an attempt to characterize, a priori, the behavior of our propagation link under low-visibility conditions. We recognize that, because conditions present on our link violate a number of premises made in the Lincoln Laboratory simulation, there is no guarantee that the following predictions will be borne out in the experiment. We feel, however, that the Lincoln Laboratory work provides a useful setting in which to discuss our experimental results.

1. Lincoln Laboratory Simulation

We may succinctly summarize Bucher's Monte Carlo cloud simulation as follows. The atmosphere was modeled as a plane-parallel slab of homogeneously distributed scatterers. The slab had thickness L and was infinitely wide. The particles were assumed to be nonabsorbing (unity albedo), with a common scattering function which was taken variously to be a Mie pattern, a Henyey-Greenstein function, or a "megaphone" (unique scattering angle). The parameters of each of these scattering functions were adjusted to yield an average cosine of the scattering angle, $\langle \cos \theta \rangle$, of 0.875.

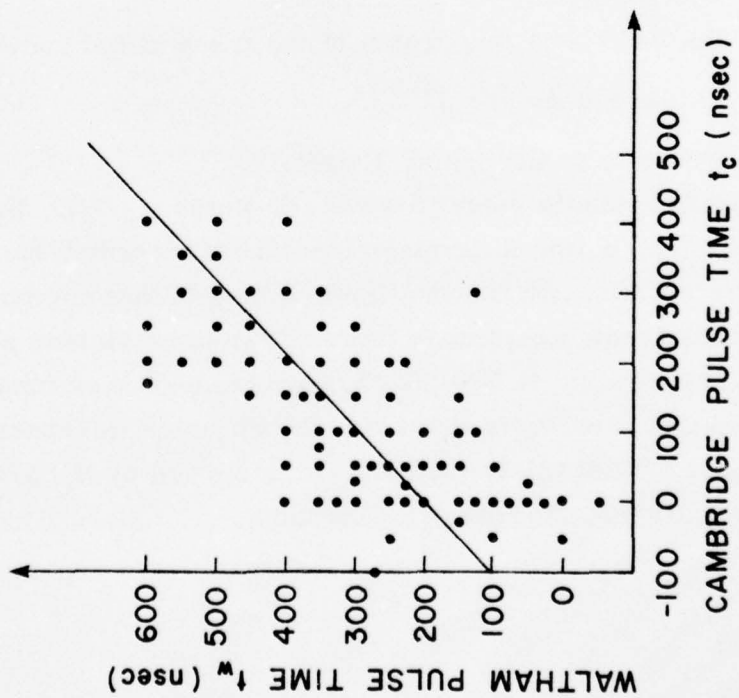


Fig. 7. Timing jitter measurement. This scatter diagram was obtained by simultaneously recording the time delays between the trigger pulse and the optical pulse at Cambridge and Waltham. There are 213 points in this figure; multiple points with the same t_c , t_w values are not indicated. The solid line is a least-squares fit to the data, from which it is found that the RMS synchronization-link jitter is 74.5 nsec.

For a ray source normally incident on the atmospheric slab, the distribution of transmitted rays emerging from the slab was determined by a Monte Carlo procedure. Significantly, it was found that the output distribution in space, angle, and time was, for thick enough slabs, independent of which scattering function was employed in the simulation. Bucher argues that this behavior is characteristic of propagation when multiple-scattering predominates. He deduces the following scaling laws for the multiple-scattering limit:

- i) the fraction of the incident radiation that is transmitted through the slab, T , satisfies

$$T \approx 1.69/(\tau_d + 1.42), \quad (1)$$

where $\tau_d \equiv \alpha L(1 - \langle \cos \theta \rangle)$;

- ii) the light transmitted through the slab exits as a circular spot of median diameter, d_s , which satisfies

$$d_s \approx 1.56 L/\tau_d^{0.07}; \quad (2)$$

- iii) the angular spectrum of the transmitted radiation is quite broad, it is concentrated within a $\pi/4$ Rad full cone-angle field of view with no sharp peaks to the distribution;

- iv) the RMS time dispersion of the transmitted radiation, σ_t , satisfies

$$\sigma_t \approx 0.64 L(\tau_d)^{0.82}/c, \quad (3)$$

where c is the speed of light.

The foregoing results apply to slabs for which $\tau_d \geq 3$. Bucher attaches the term diffusion regime to propagation conditions which satisfy the above criterion. His justification for this terminology is that computer simulation of pure diffusion (isotropic scatter) in three dimensions yielded scaling laws for d_s and σ_t that were similar to Eqs. (2, 3) when compared as functions of τ_d (rather than τ). The parameter τ_d is therefore the diffusion thickness of the slab, i.e., it is the usual optical thickness, $\tau = \alpha L$, modified by the predilection of the particles to scatter in the forward direction.

2. Transmission-Fraction Analysis

Let us apply Bucher's scaling laws to the Cambridge-to-Waltham propagation path. We shall suppose that these laws are valid for all values of $\langle \cos \theta \rangle$. Moreover, we shall not attempt to account for atmospheric inhomogeneity, particle absorption, or boundary (ground) losses, that are obviously present to some extent in our experiment, but were not included in the computer simulation. Our primary concern herein will be to delineate two asymptotic propagation regimes for this path: the clear-weather regime wherein unscattered radiation dominates the received signal, and the very low visibility regime wherein diffuse radiation (governed by the scaling laws of section B.1) dominates the received signal. In particular, we shall determine the crossover optical thickness at which these two asymptotes are equal. However, because of factors neglected in this analysis, we cannot argue that the calculated crossover optical thickness (which under some circumstances does not exist) accurately characterizes the Cambridge to Waltham path. Indeed, we cannot deny the possibility that there is another mode of scatter propagation which renders the above crossover-thickness calculation valueless. Putting these caveats aside, let us begin by considering the unscattered radiation.

The fraction, T_u , of the transmitter signal that reaches the plane containing the receiver's entrance pupil as unscattered light is given by the Bouguer-Lambert extinction law

$$T_u = \exp(-\tau). \quad (4)$$

Of the unscattered light reaching the receiver entrance-pupil plane, only a fraction $A_r/(\theta_t L)^2$ is intercepted by the entrance pupil, where A_r is the effective pupil area and θ_t is transmitter beam divergence (full cone angle). Thus T_u^r , the fraction of the transmitter signal that is intercepted as unscattered radiation by the receiver pupil, satisfies

$$T_u^r = A_r \exp(-\tau)/(\theta_t L)^2. \quad (5)$$

When the transmitter and receiver are in boresight alignment, essentially all of the unscattered radiation entering the receiver pupil will pass through the focal-plane pinhole and onto the photodetector if the receiver field of view (determined by the pinhole) exceeds the nominal clear-weather blur circle of the telescope. This blur circle would have a full cone angle of the order

of $\lambda/A_r^{1/2}$ Rad at wavelength λ for a diffraction-limited instrument. Telescope aberrations, atmospheric turbulence, and platform vibration may typically increase the blur circle full cone angle to 0.1 mRad.

Let us now consider the diffusion regime. When the visibility is low enough to satisfy $\tau_d \geq 3$, the fraction, T , of the transmitter signal that reaches the plane containing the receiver's entrance pupil will be assumed to satisfy Eq. (1). In Fig. 8 we have plotted T_u and T versus optical thickness, $\tau = \alpha L$, for various values of $\langle \cos \theta \rangle$. The T curves all begin at $\tau_d = 3$. Figure 8 shows, in essence, what was suggested in Chap. I, i.e., for a lossless scattering medium the transmission of scattered radiation may enormously exceed the unscattered transmission.

Of the scattered light reaching the receiver entrance-pupil plane, the fraction that is collected by the pupil will be assumed to be A_r/d_s^2 , where d_s satisfies Eq. (2). Thus, the fraction of the transmitter light that (in the diffusion regime) is collected by the receiver pupil, T^r , is

$$T^r \approx 0.696 A_r (\tau_d)^{0.14} / L^2 (\tau_d + 1.42). \quad (6)$$

In Fig. 9 we have plotted T_u^r and T^r versus optical thickness for various values of $\langle \cos \theta \rangle$ using $A_r = 127 \text{ cm}^2$, $\theta_t = 10 \text{ mRad}$, and $L = 13.6 \text{ km}$. Evidently, for sufficiently large $\langle \cos \theta \rangle$ values (e.g., $\langle \cos \theta \rangle = 0.8$ in Fig. 9) there will not be a crossover optical thickness at which the unscattered-light and the diffusion-regime receiver-pupil transmission fractions are equal, i.e., for sufficiently large $\langle \cos \theta \rangle$ we have $T_u^r < T^r$ at $\tau_d = 3$. However, when there is a crossover optical thickness in Fig. 9, it occurs in the vicinity of $\tau = 11$, an optical thickness for which the diffusion-regime receiver-plane transmission fraction greatly exceeds the corresponding transmission fraction for unscattered light, c.f. Fig. 8. This is due to the enormous spatial spreading of the multiply-scattered light as opposed to the small spatial extent of the highly collimated unscattered beam. The crossover point shifts to higher optical thicknesses (lower visibilities) when the effect of receiver field of view is included. For a receiver field of view whose full cone angle, θ_r , exceeds the full cone angle of the clear-weather blur circle, all of the unscattered light intercepted by the receiver pupil reaches the photodetector. On the other hand, if $\theta_r \leq \pi/4$, only a fraction $\sin^2(\theta_r/2)/\sin^2(\pi/8)$ of the diffusion-regime light collected by the receiver pupil reaches the photodetector. In Fig. 10 we have

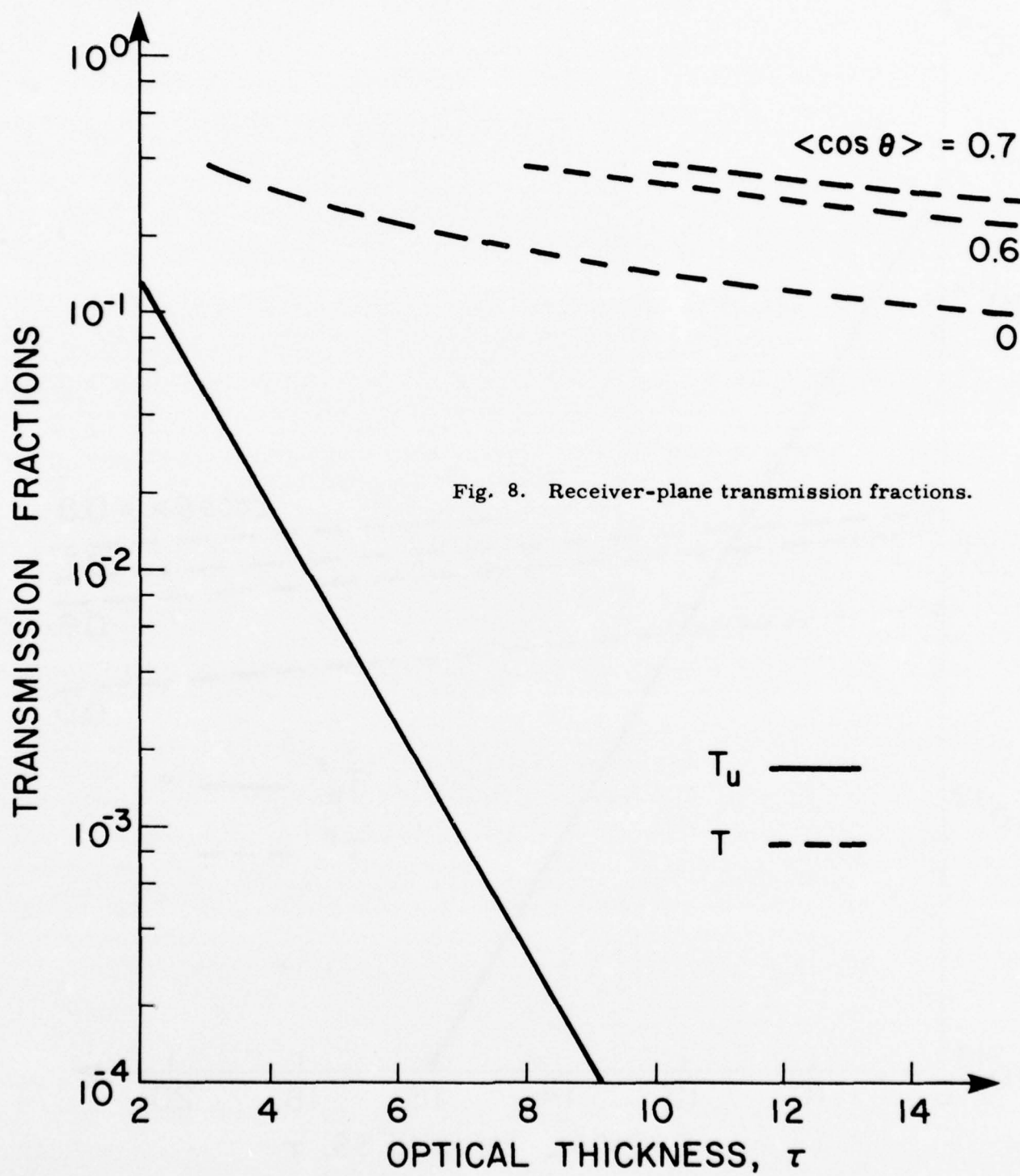


Fig. 8. Receiver-plane transmission fractions.

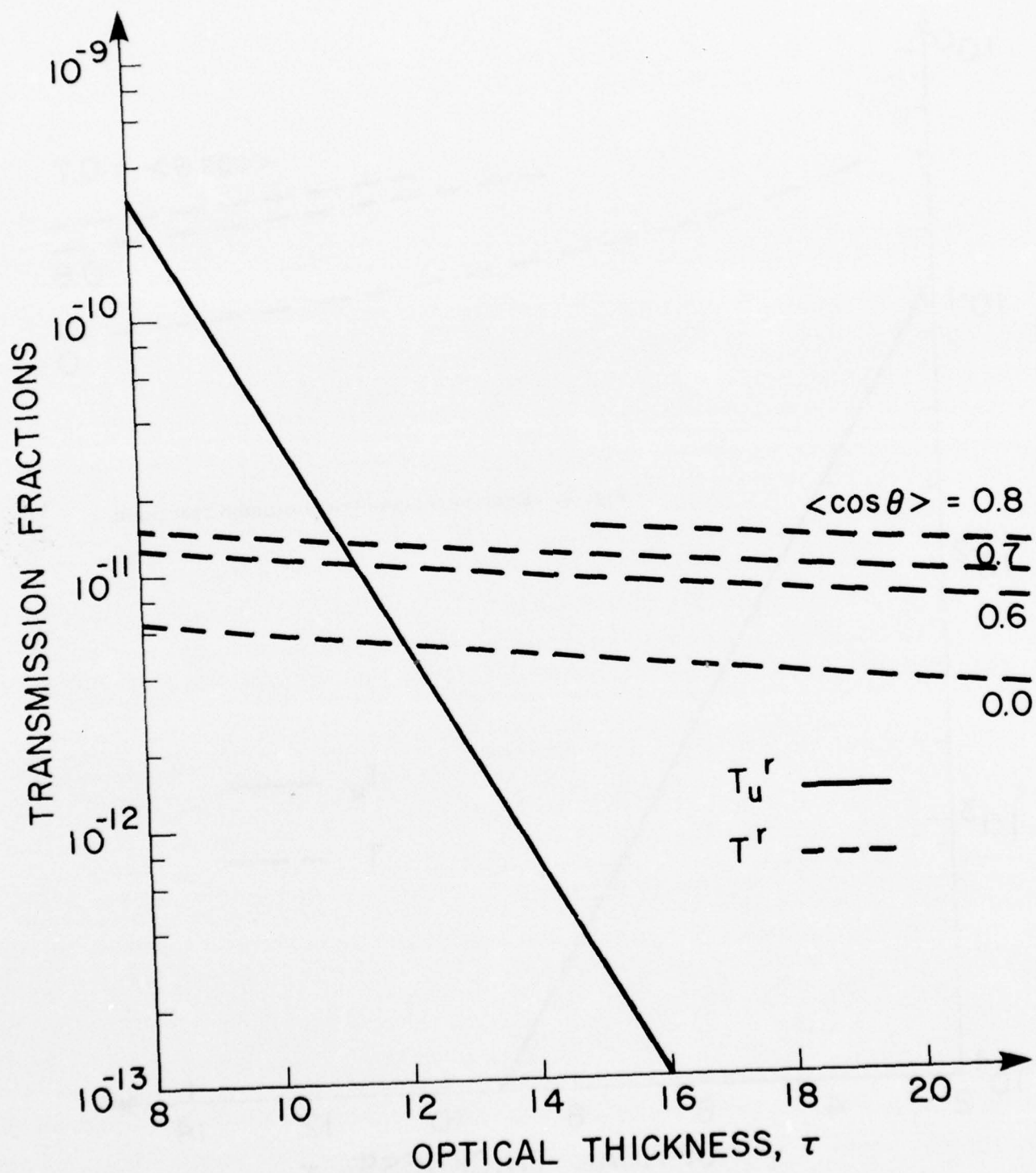


Fig. 9. Receiver-pupil transmission fractions.

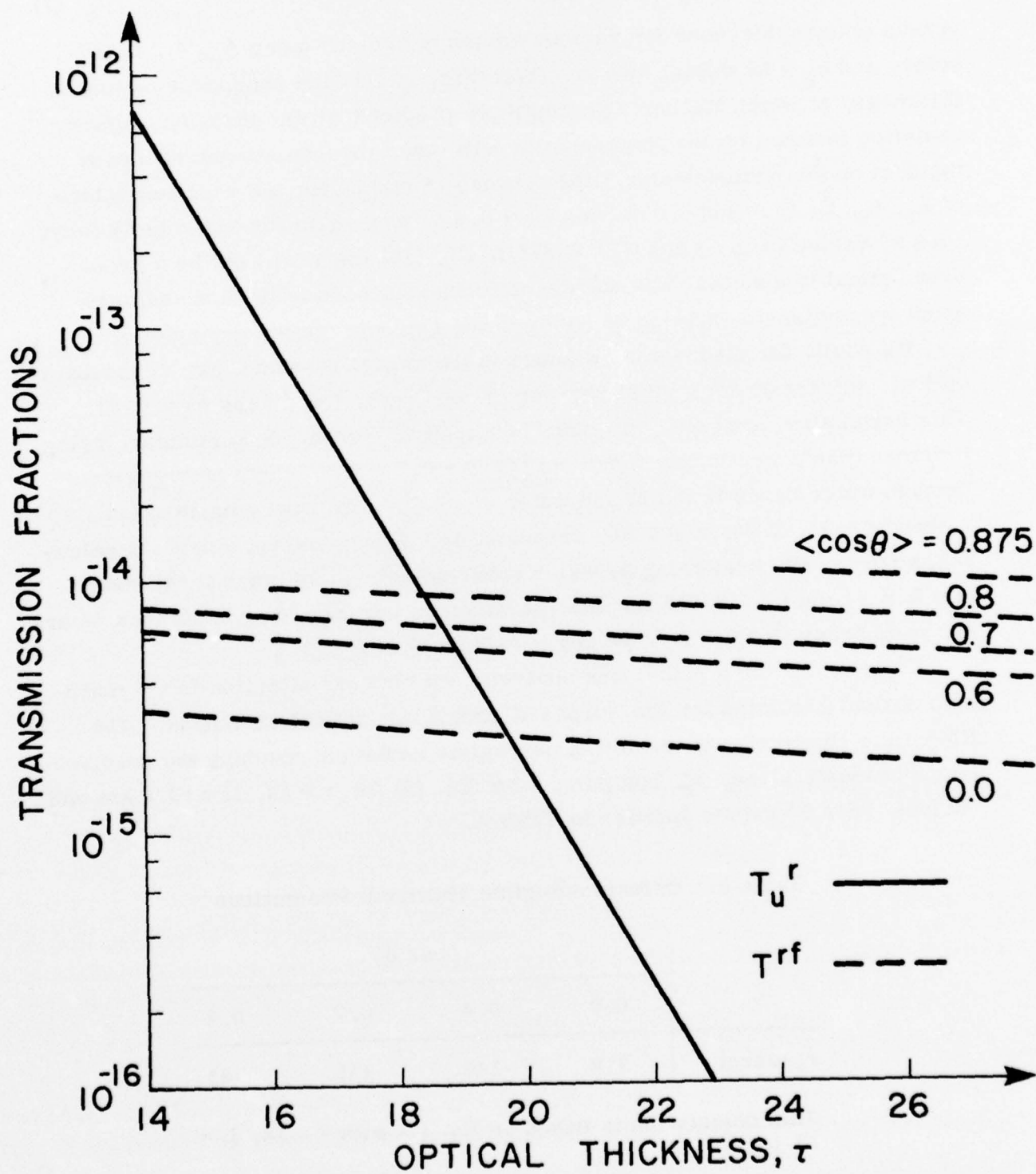


Fig. 10. Receiver focal-plane transmission fractions.

plotted T_u^r and

$$T^{rf} \equiv T^r \sin^2(\theta_r/2)/\sin^2(\pi/8), \quad (7)$$

versus optical thickness for various values of $\langle \cos \theta \rangle$ using A_r , θ_t , L as before and $\theta_r = 20$ mRad. We see from Fig. 10 that the crossover optical thickness, at which Bucher's scaling laws predict that the diffusion-regime radiation incident on the photodetector will equal the unscattered radiation incident on the photodetector, lies between 18 and 20 for the assumed values of A_r , θ_t , L , θ_r , and $0.0 \leq \langle \cos \theta \rangle \leq 0.8$. Once again for sufficiently large $\langle \cos \theta \rangle$ values (e. g., $\langle \cos \theta \rangle = 0.875$ in Fig. 10) there will not be a crossover optical thickness. For such $\langle \cos \theta \rangle$ values there is little we can say about transmission-fraction behavior in the gap between the asymptotes.

We shall, for discussion purposes in the sequel, assume that a crossover optical thickness does exist for our experiment, i. e., $\langle \cos \theta \rangle \leq 0.83$. This assumption need not, however, be physically valid. In particular, using Deirmendjian's scattering functions [26] for 0.7μ wavelength propagation through water hazes H and M and water cloud C.1, we have computed $\langle \cos \theta \rangle$ values of 0.74, 0.79, and 0.84, respectively. Furthermore, Bucher's calculation [25] of Mie scattering by water spheres (refractive index 1.34) shows that $0.8 \leq \langle \cos \theta \rangle \leq 0.875$ for Mie parameters between 30 and 200 such as are known to occur (for 0.7μ wavelength radiation) in fog [27].

To conclude the a priori link analysis, we turn our attention to the multipath spread predicted for the supposed crossover optical thickness. The RMS time dispersion of the diffusion-regime radiation reaching the receiver entrance-pupil plane, σ_t , computed from Eq. (3) for $\tau = 18$, $L = 13.6$ km and various $\langle \cos \theta \rangle$ values appears in Table 1.

Table 1. Diffusion-Regime Multipath Predictions

	$\langle \cos \theta \rangle$			
	0.0	0.6	0.7	0.8
σ_t (μ sec)	310	146	115	83

This calculation is based on Eq. (3) with $\tau = 18$, $L = 13.6$ km.

C. Propagation-Link Measurements

The preceding transmission-fraction analysis suggests that the following behavior should be encountered in our ruby-link measurements. Under clear to modest-visibility conditions, the detected boresight ruby signal should be dominated by unscattered radiation. We should thus observe an exponential extinction with decreasing visibility, a sharply peaked angular spectrum (perhaps 0.1 mRad full cone angle), and negligible time dispersion. As the visibility decreases, the detected boresight ruby signal should eventually be dominated by the diffusion-regime light. Assuming our receiver is sufficiently sensitive to make measurements in this regime, we should observe an algebraic decay of transmission with further decreases in visibility, an angular spectrum whose full cone angle is order of magnitude 1 Rad, and time dispersion (multipath spread) well in excess of 1 μ sec.

We do not know from the transmission-fraction analysis whether the transition from the unscattered to the diffusion behavior will occur abruptly or gradually. It may be that the boresight detected signal follows the unscattered transmission-fraction curve all the way to the crossover optical thickness, at which point an immediate changeover to the diffusion regime occurs. On the other hand, it is possible that, due at first to single scatter and later to low-order multiple scatter, the measured boresight transmission fraction gradually changes from the unscattered result (at very low optical thicknesses) to the diffusion-regime result (at very high optical thicknesses). In the former case, we should expect to see little or no angular spread or multipath spread as the visibility decreases until the crossover thickness is reached, at which point very large angular spread and multipath spread are suddenly apparent. In the latter case, we should expect to see gradual increases in both the angular and multipath spread of the boresight signal with decreasing visibility, i. e., no dramatic changes in the received signal will be manifested as the crossover optical thickness is exceeded.

The data we have obtained are somewhat equivocal with regard to the above possibilities. The observed multipath spread was never more than 50-350 nsec, and angular spectra were at most a few mRad full cone angle, in concert with the hypothesis that our measurements were dominated by unscattered radiation. However, there was a tendency for the width of the

observed angular spectrum to increase with decreasing visibility. Furthermore, the near-absence of multipath and the narrow angular spectrum persisted when measurements were made with the receiver purposefully misaligned to reduce the level of received unscattered radiation. These observations suggest a gradual transition from unscattered transmission to the diffusion regime, such as might be due to multiple forward scatter (cf. [25]). Finally, it appears that our links are not sufficiently sensitive to reach the crossover optical thickness calculated in section B. 2. Thus it is not too surprising that very large angular and multipath spreads were not observed, i. e., when the visibility was low enough to put our links into the diffusion regime, we were unable to measure any signal.

The details of the experiments are presented below; in section C. 1 we describe the data, in section C. 2 we compare the experimental results with the transmission-fraction analysis of section B. 2.

1. Multipath and Angular Spread

Under clear-weather conditions (visibility 10 miles or greater), the ruby laser pulse appears at the receiver to be of 150 nsec duration (see Fig. 11). We believe that the transmitter produces a 70 nsec pulse; a pulse monitor in Cambridge shows a 100 nsec duration limited by the monitor electronics. We ascribe the excess pulse duration observed in clear weather at Waltham to the finite bandwidth of the post-detection electronics; a single-photon event has a rise-fall time of 30 nsec. In low-visibility weather (visibility < 6 miles), three types of received-pulse behavior have been observed on the ruby link:

- i) pulse shape and duration identical with that seen in clear weather;
- ii) pulse duration comparable to that seen in clear weather, but with internal structure (see Fig. 12);
- iii) pulse duration 50-350 nsec longer than that seen in clear weather; pulse has a sharp rising edge and a slow decay (see Fig. 13).

In Table 2 we have summarized our multipath observations, using the designations i), ii), and iii) to categorize pulse behavior as described above. These observations were made with the transmitter and receiver in boresight alignment. Measurements taken on or before 7/21/76 were made using a 1.8 mRad FWHM transmitter beam divergence; measurements taken after

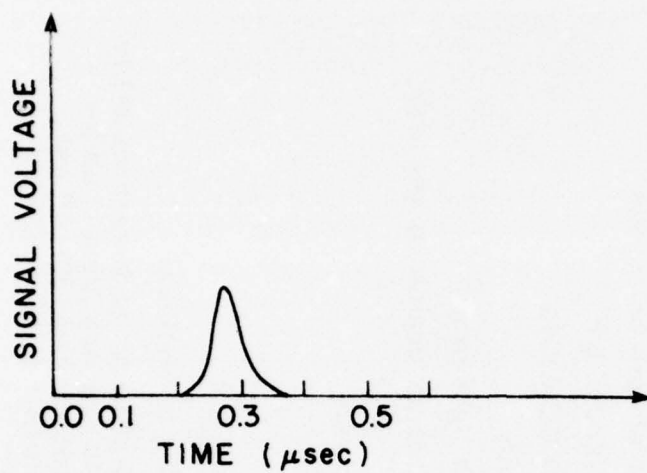


Fig. 11. Clear-weather ruby pulse.

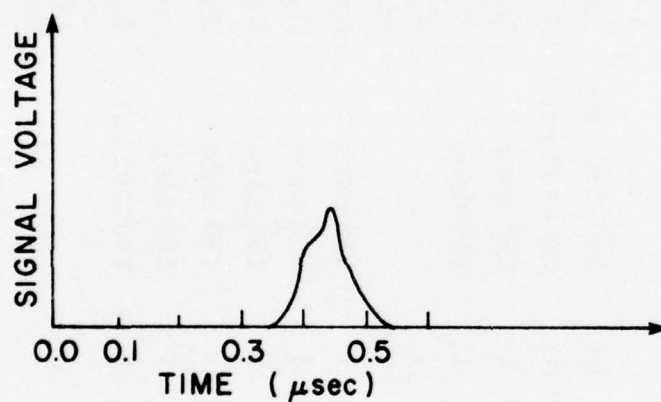


Fig. 12. Type ii ruby pulse.

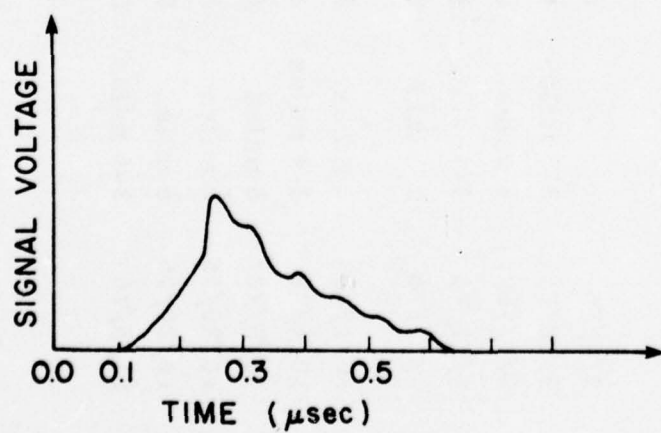


Fig. 13. Type iii ruby pulse.

Table 2. Ruby Laser Multipath Observations

Date	Visibility		Pulse Characteristics		Weather Conditions
	from Cambridge	from Waltham	type	duration	
11/21/75	3 miles	3 miles	i	150 nsec	heavy rain
2/18/76	1 mile	0.25 mile	-	-	heavy fog with light rain; unable to see any signal
3/3/76	2 miles	2 miles	i	150 nsec	fog with light snow; signal faded out as visibility decreased to ≤ 1 mile at both terminals
3/5/76		5 miles	iii	300-500 nsec	fog in Cambridge
5/12/76	2-3 miles	4 miles	iii	200-400 nsec	fog with light rain
6/1/76	6 miles	6 miles	i	150 nsec	light rain
7/21/76	3-4 miles	2-3 miles	i	150 nsec	fog with light rain
9/17/76	0.5 mile	0.5 mile	-	-	fog and rain; unable to see any signal
10/1/76	6 miles	6 miles	i	150 nsec	haze and fog
10/6/76	3-4 miles	2 miles	i	150 nsec	fog
10/8/76	6 miles	6 miles	i	150 nsec	haze
10/20/76	6 miles	2-3 miles	i	150 nsec	fog and rain
10/20/76	6 miles	0.5-1 mile	i	150 nsec	heavy fog in Waltham
11/5/76	3-4 miles	0.1-1 mile	ii	150-200 nsec	fog in Waltham; at lowest visibility unable to see any signal, as fog lifted pulses had 150-200 nsec duration in 1 mile visibility
11/10/76	7 miles	5-6 miles	ii	150 nsec	haze

7/21/76 were made using a 10 mRad FWHM beam divergence. On all days, measurements were made with various receiver fields of view ranging from 1 mRad (or less) to 20 mRad full cone angle; on no occasion was a variation in time dispersion with field of view noted. On several days, measurements were made with the receiver aimed above the transmitter; no significant increase in time dispersion was found, nor was there any discernible differential time delay between on-axis and off-axis observations. (Because of synchronization jitter, differential delays of less than 100 nsec cannot be distinguished from timing errors.)

The near-total absence of multipath in the on-axis data is consistent with the hypothesis that these measurements are primarily sensing unscattered radiation. However, the absence of multipath or differential delay in the off-axis data indicates that the scattered radiation is itself largely free of time dispersion. It is of interest, therefore, to examine the angular spectrum measurements. An on-axis signal dominated by unscattered radiation will manifest a sharply peaked angular spectrum. An off-axis scattered signal that is essentially free of multipath and differential delay should also exhibit a narrow angular spectrum, for it would otherwise be likely for there to be excess path lengths (relative to on-axis unscattered transmission) of more than the 100 feet needed to be resolvable as 100 nsec dispersion or delay. We shall examine data from both the ruby and holmium links.

Under clear-weather conditions (visibility 10 miles or greater), both the ruby and holmium wavelength angular spectra are quite narrow; typical examples appear in Figs. 14 and 15. We believe that in clear weather the width of the ruby wavelength angular spectrum is due to atmospheric turbulence [12]. (Indeed, in a stable 8 mile visibility haze, narrower ruby angular spectra are observed than in, presumably more turbulent, 12 mile visibility clear windy weather.) We believe that the width of the clear weather holmium angular spectrum is due to telescope aberrations. (The Zoomar optics, and in particular, the Schmidt corrector plate, were not designed for use in the infrared.)

Under low-visibility conditions, the ruby and holmium angular spectra continue to have the general characteristics of Figs. 14, 15; typical examples appear in Figs. 16-19. These low-visibility observations are for coaxial transmitter-receiver alignment; thus they may be indicating nothing more

\bar{I} = 10 mile visibility in haze,
 10/26/76, dot is mean of
 10 pulses, bars show high-
 est and lowest values

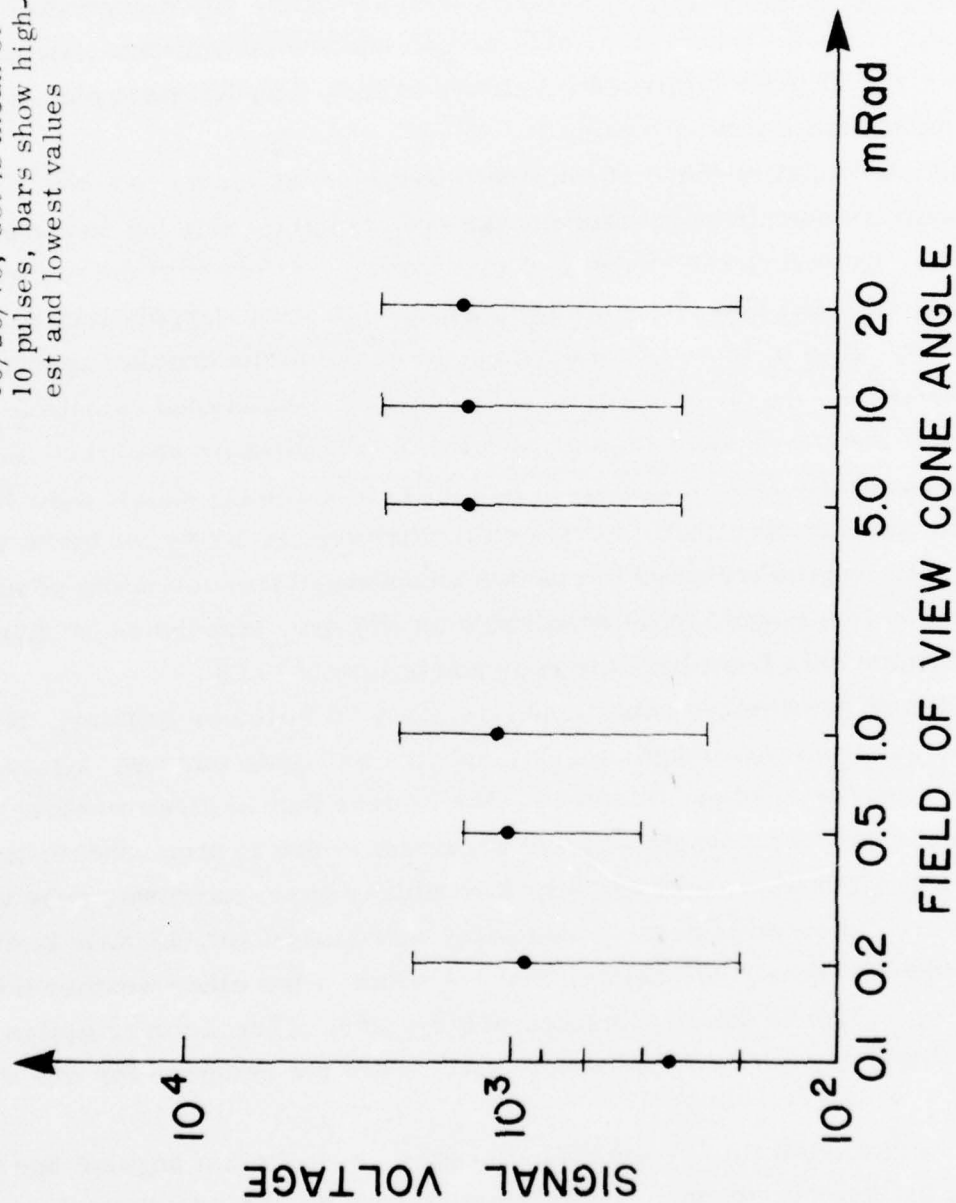


Fig. 14. Clear-weather ruby link signal vs receiver field of view.

I = 12 mile visibility, 10/18/76,
15 sec of boxcar averaging
with 4 sec effective time
constant

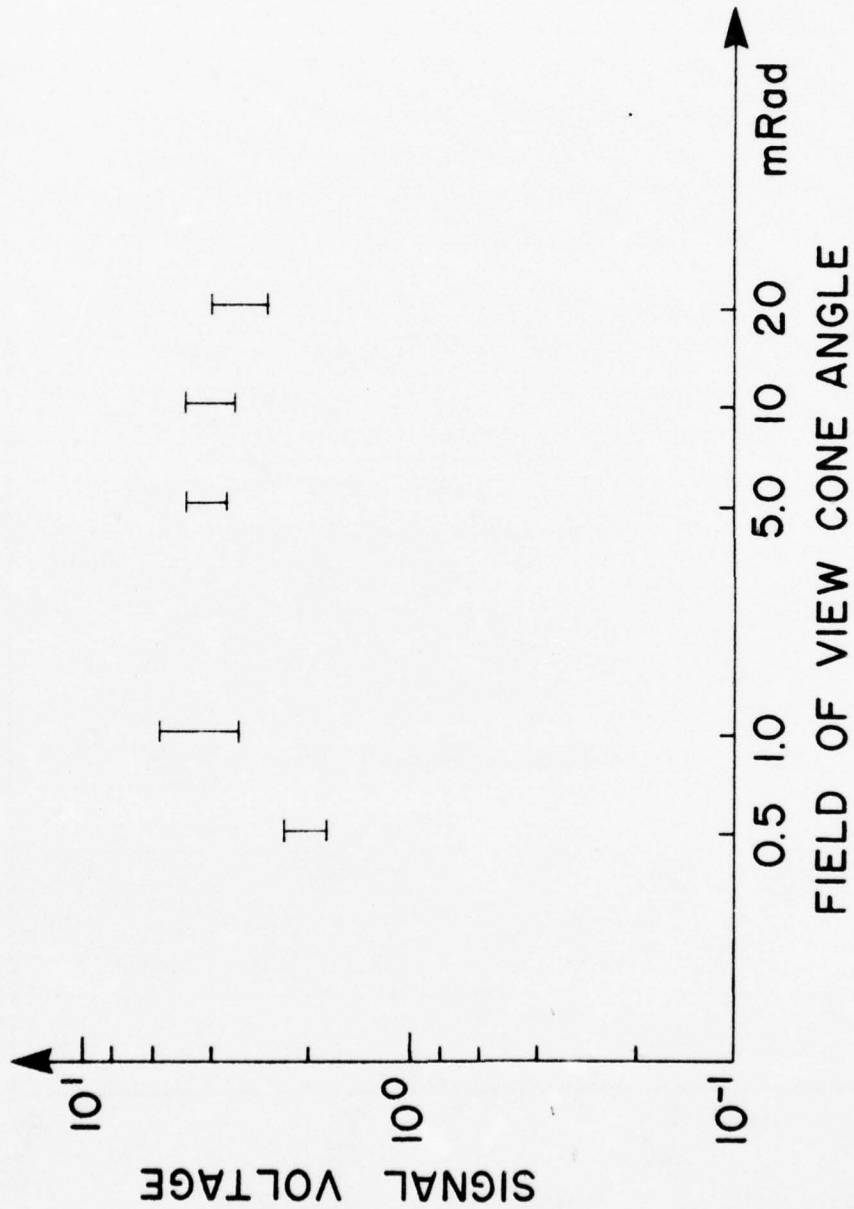


Fig. 15. Clear-weather holmium link signal vs receiver field of view.

\bar{I} = 2-4 mile visibility in fog,
 10/6/76, dot is mean of
 10 pulses, bars show high-
 est and lowest values

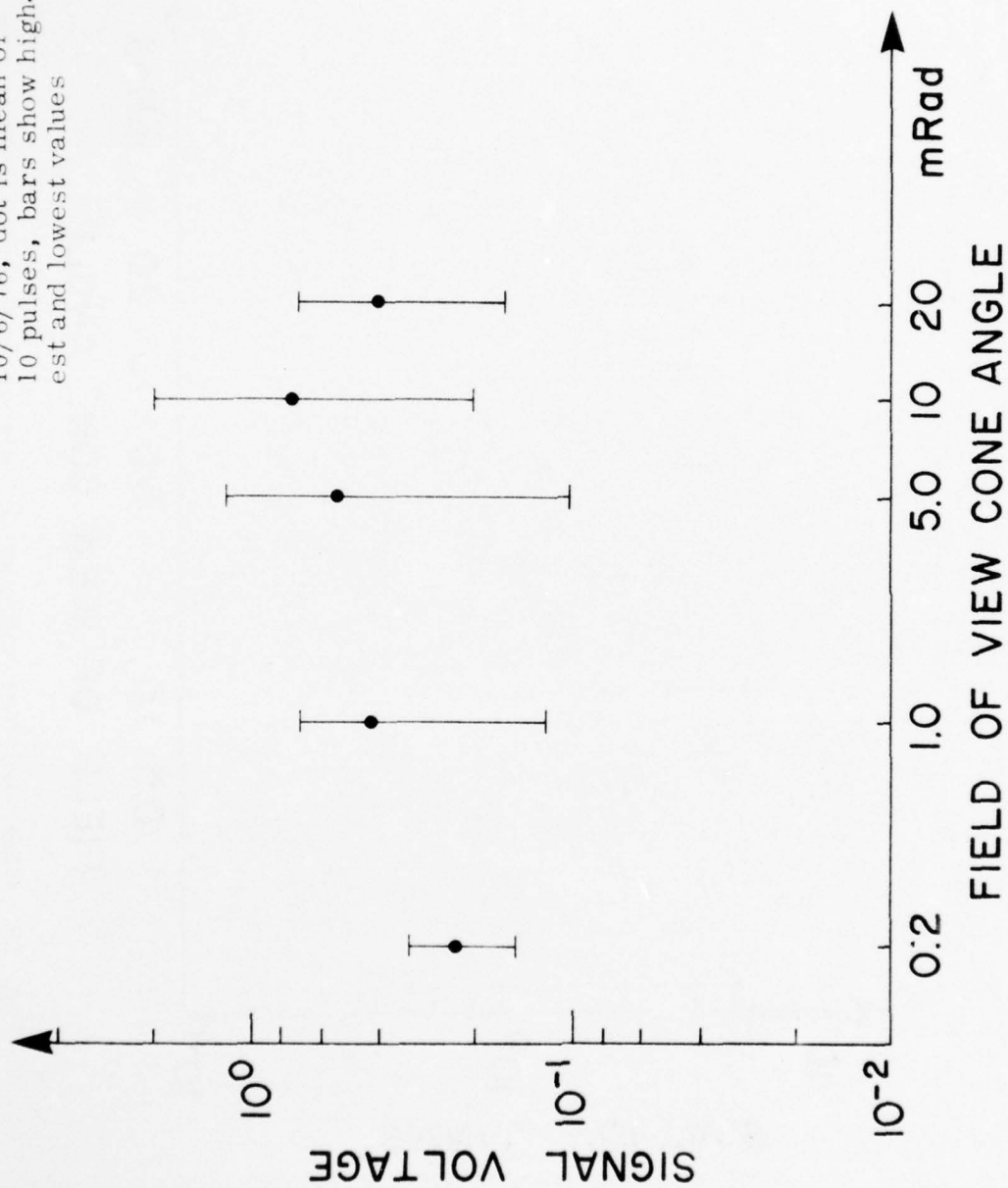


Fig. 16. Low-visibility ruby link signal vs receiver field of view.

$\bar{x} \pm \sigma$ = 3-4 mile visibility in fog,
 10/20/76, dot is mean of
 10 pulses, bars show high-
 est and lowest values

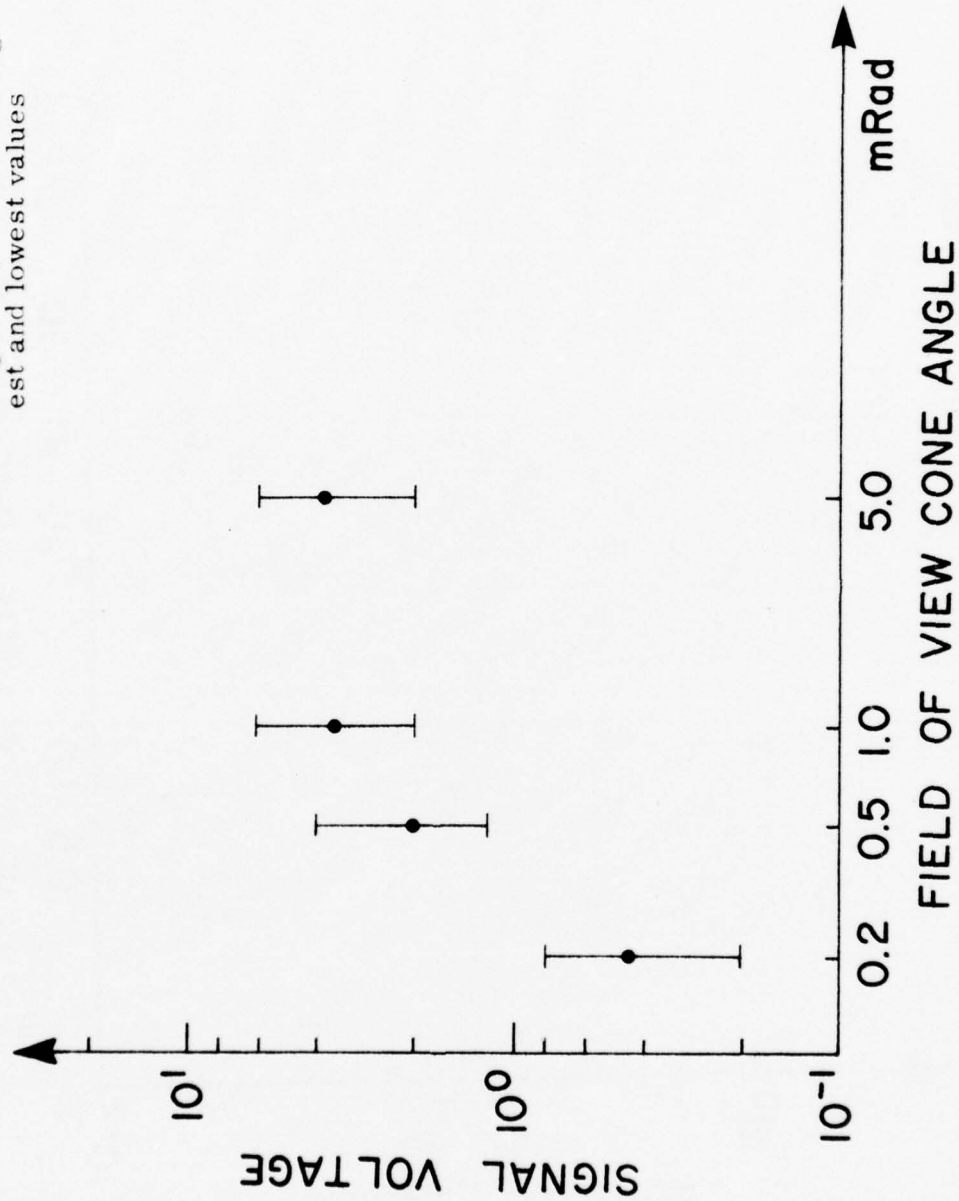


Fig. 17. Low-visibility ruby link signal vs receiver field of view.

I = 4-8 mile visibility, in rain,
 9/2/76, 15 sec of boxcar
 averaging with 4 sec effec-
 tive time constant

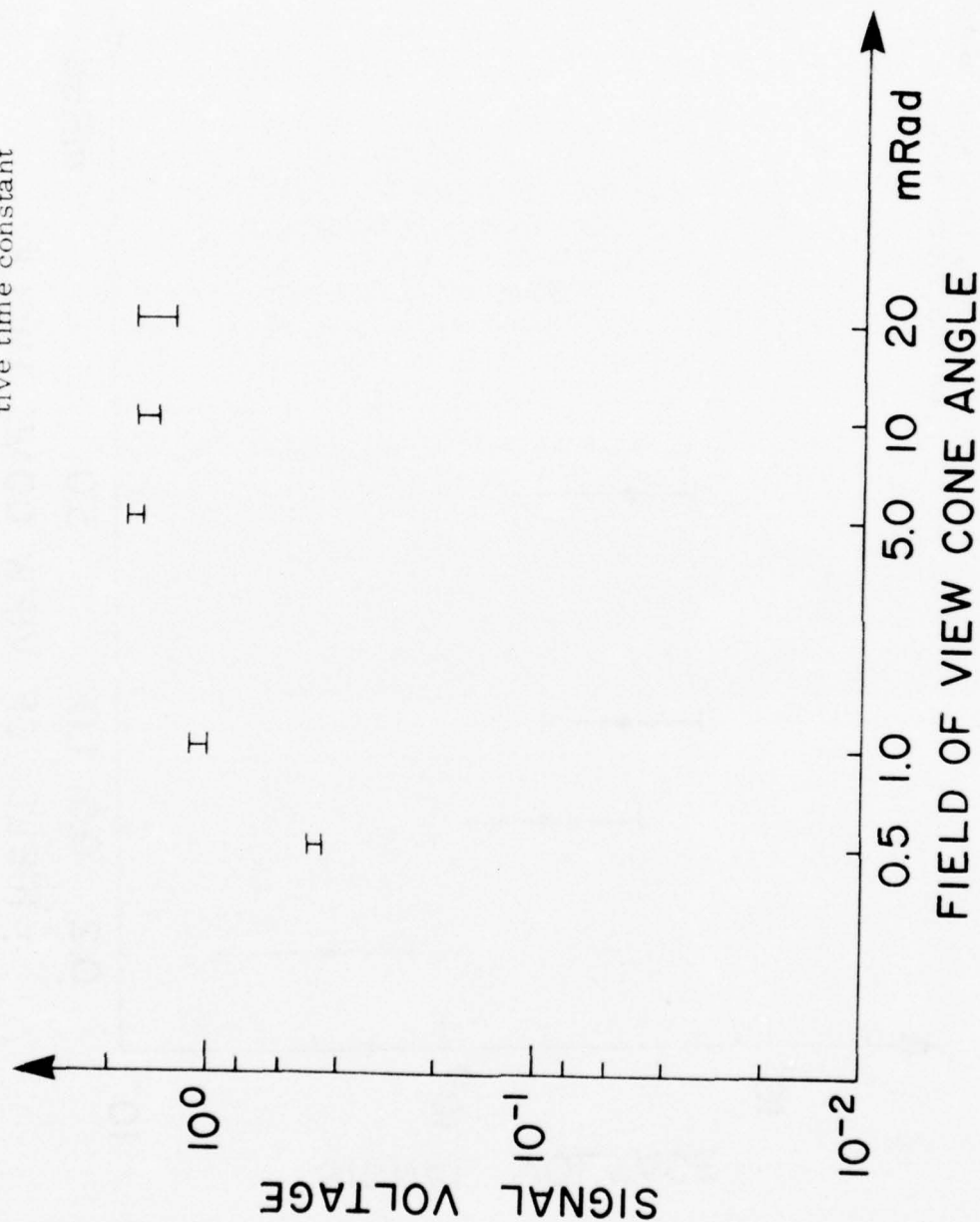


Fig. 18. Low-visibility holmium link signal vs receiver field of view.

$I = 2-4$ mile visibility in fog,
11/5/76, 15 sec of boxcar
averaging with 4 sec effec-
tive time constant

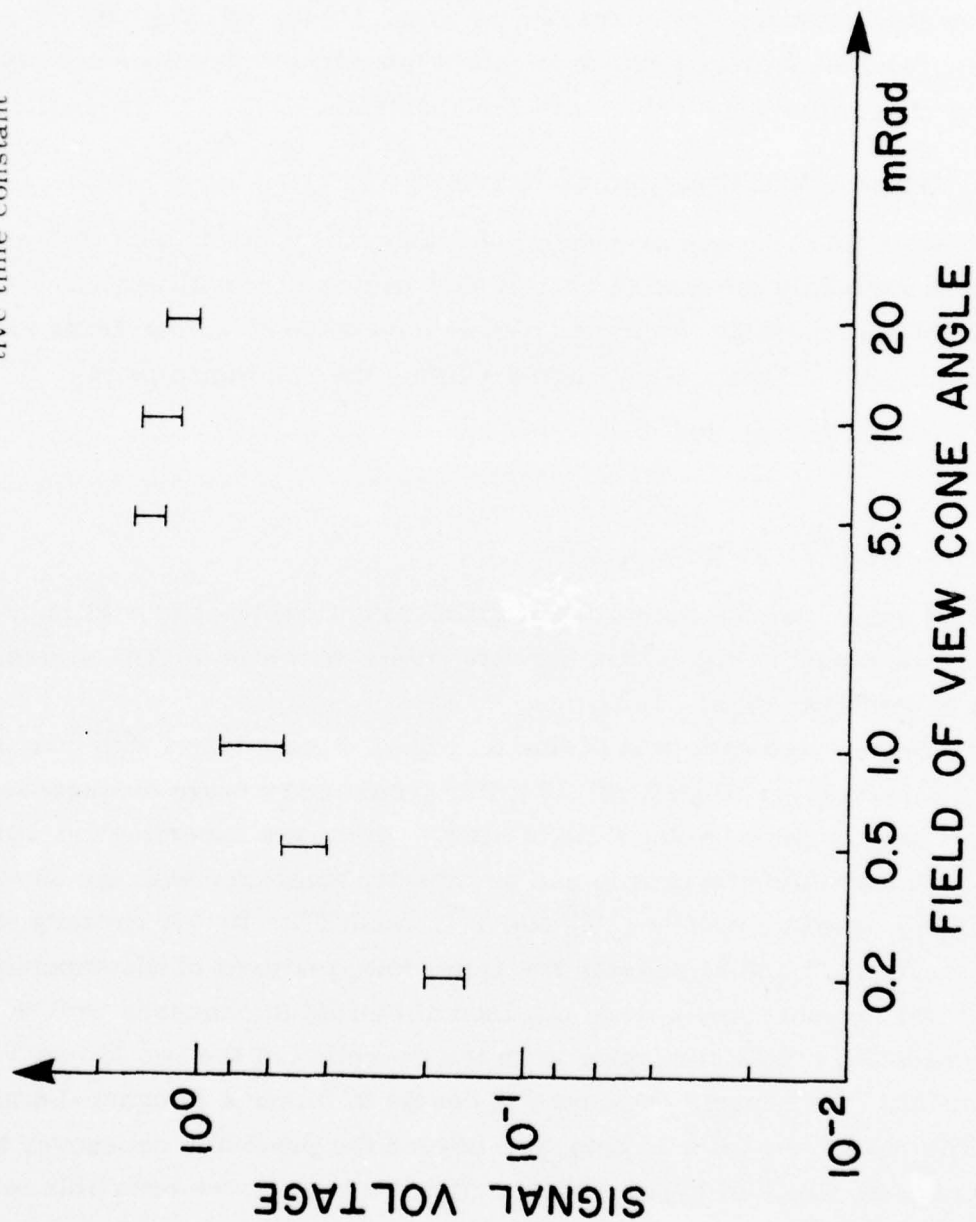


Fig. 19. Low-visibility holmium link signal vs receiver field of view.

than unscattered radiation. To a certain extent this conclusion is negated by the tendency of the angular spectra to broaden somewhat in the lowest visibilities. Moreover, angular spectrum measurements made with the transmitter purposefully misaligned (to reduce unscattered transmission to the photodetector) show the same general character as Figs. 16-19, cf. Fig. 20. Thus it would appear the scattered radiation intercepted by the receiver arrives with a narrow (few mRad cone angle) angular spectrum.

2. Transmission-Fraction Comparison

We shall conclude our propagation-measurement discussion with an attempt to reconcile the data of section C.1 with the transmission-fraction analysis of section B.2. In Tables 3-5 we have assembled our transmission data at ruby and holmium wavelengths. Using the relationships [4]

$$\tau = 26.7/V \quad \text{at } 694.3 \text{ nm}, \quad (8)$$

and

$$\tau = 16.8/V \quad \text{at } 2.06 \mu, \quad (9)$$

to convert visibility, V , measured in miles to optical thickness at ruby and holmium wavelengths, we obtain the data points shown in the transmission versus τ profiles, Figs. 21-23.

The ruby-wavelength data (Table 3, Fig. 21) were taken with coaxial transmitter-receiver alignment, 10 mRad transmitter beam divergence, and 20 mRad cone angle receiver field of view. Thus, the experimental ruby-wavelength transmission profile can be directly compared with the unscattered and diffusion-regime profiles, T_u^r and T^{rf} , from Fig. 10. A cursory examination of Figs. 10 and 21 reveals two immediate features of the experimental profile: no measurements were obtained at optical thicknesses well in excess of the predicted crossover point; with the exception of the two lowest visibility observations, the experimental profile seems to follow a Bouguer-Lambert law. The reason we have no data well beyond the predicted crossover thickness is unequivocally lack of system sensitivity; we have never been able to see the ruby signal in 1 mile or less visibility at both terminals. To explore the contention that the experimental transmission profile is explainable as an exponential extinction of unscattered light, we have least-squares fitted two

I = 4-6 mile visibility in rain and fog, 9/2/76, 15 sec boxcar averaging with 4 sec effective time constant

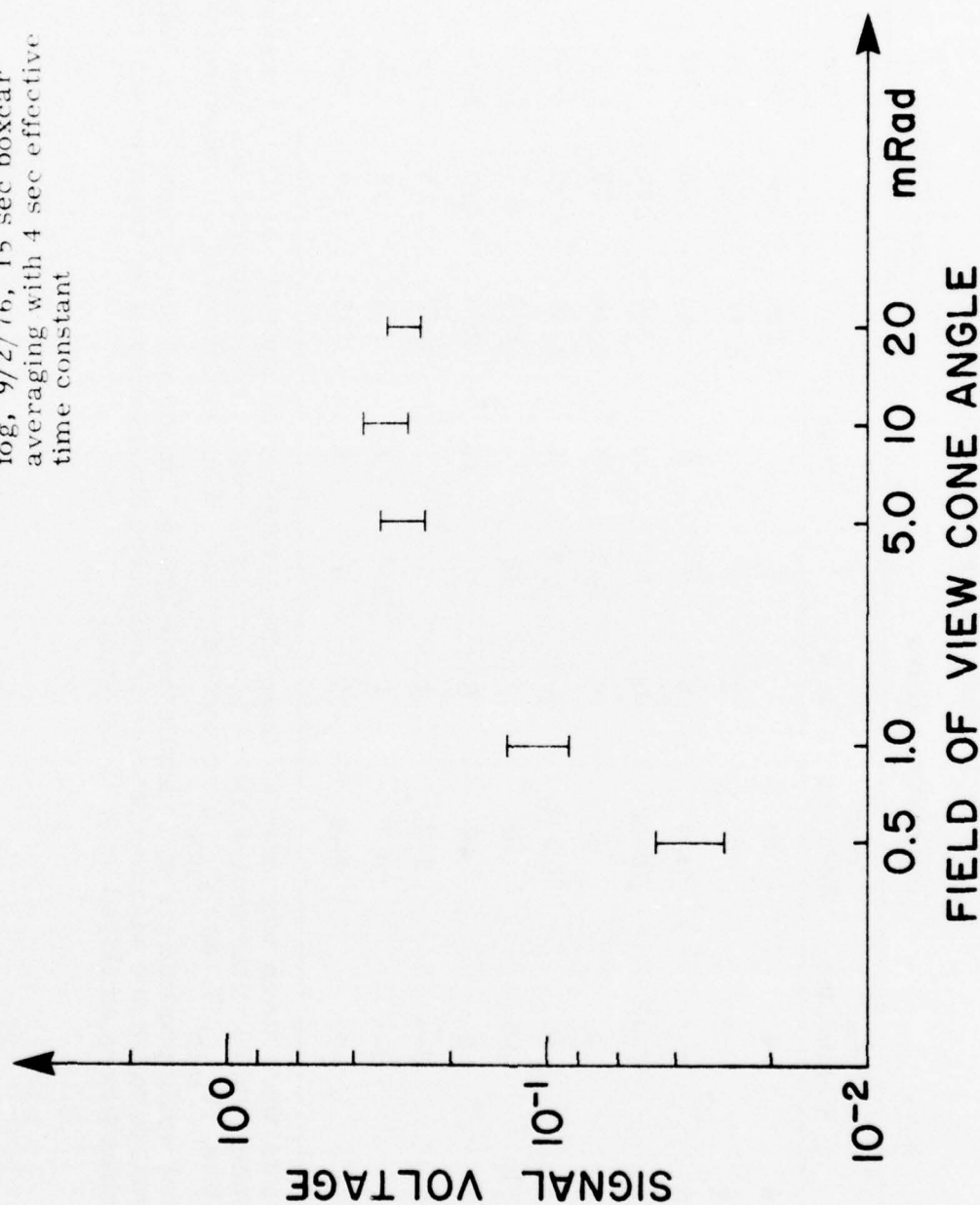


Fig. 20. Low-visibility holmium link signal vs receiver field of view, with transmitter aimed up 4 mRad.

Table 3. Ruby Laser Transmission Data

Date	Visibility in Miles				Signal Voltage		Point No.
	from Cambridge	from Waltham	V _{min}	V	V _{min}	V _{max}	
10/1/76	6	6		6	250	460	1
10/6/76	3-4	2	2	3	0.16	0.40	2
10/8/76	6-8	6-8	6	7	40	68	3
10/18/76	10-12	10-12	10	11	300	420	4
10/20/76	6	3	4	4.5	0.40	1.70	5
	6	0.5-1	2.6	3.3	2.00	3.80	6
10/22/76	10	10		10	200	600	7
10/26/76	8	10	8	9	200	1410	8
11/5/76	3-4	1-2	1	2	0.50	1.25	9
	3-4	0.1	1	1.5	.07	.12	10
11/10/76	7	5-6	5	6	75	130	11

These data were taken with coaxial transmitter-receiver alignment, 10 mRad transmitter beam divergence, and 20 mRad cone-angle receiver field of view. The minimum, nominal, and maximum visibilities, (V_{min} , V , and V_{max} respectively) are ad hoc estimates of a homogeneous-path visibility that would produce the same unscattered-light extinction as the Cambridge-to-Waltham path. The signal voltages are based on storage oscilloscope observation of ten laser pulses, corrected for the Wratten filters employed prior to detection.

Table 4. Holmium Laser Transmission Data: 1 mRad FOV

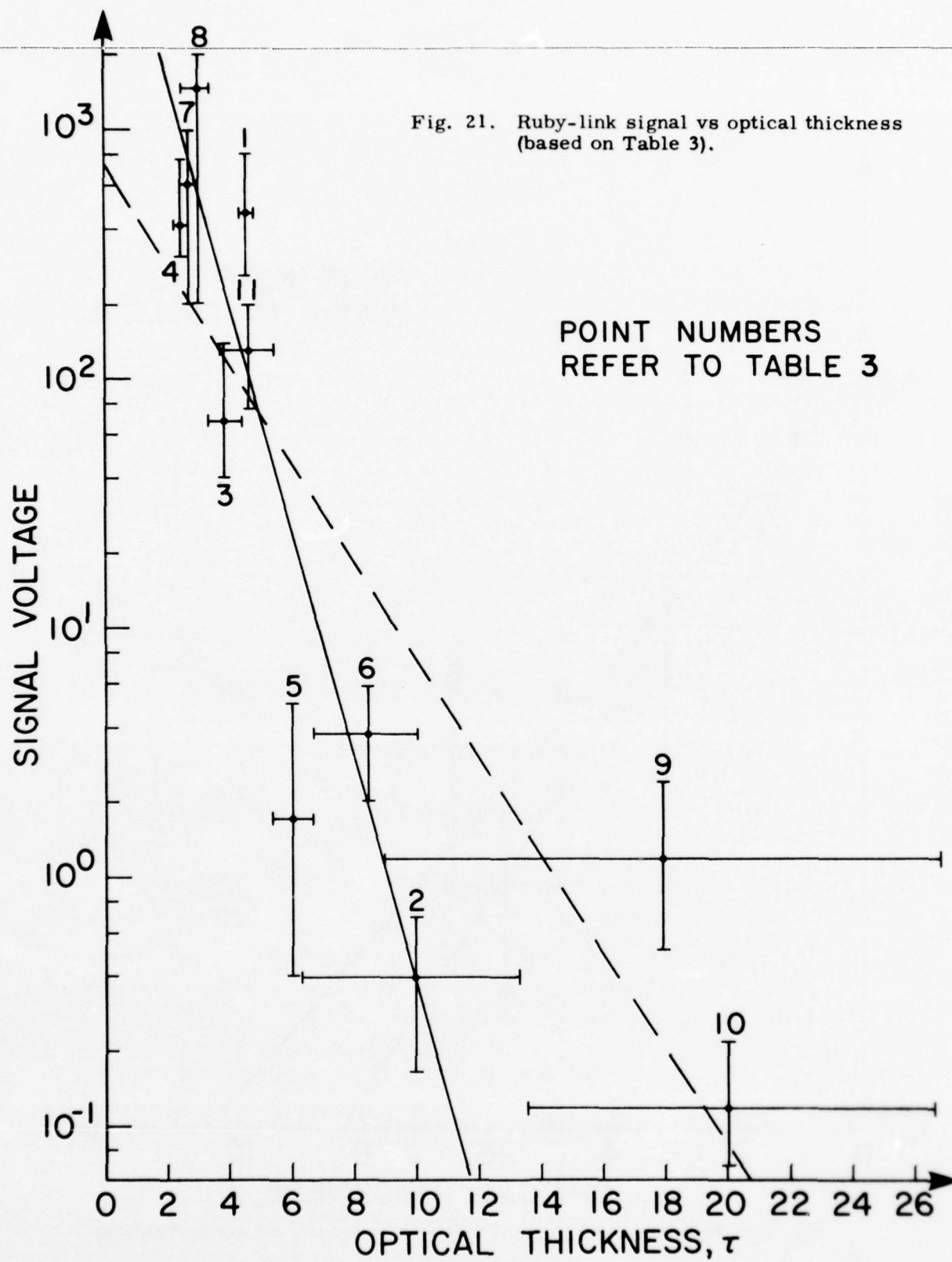
Date	Visibility in Miles				Signal Voltage			Point No.
	from Cambridge	from Waltham	V _{min}	V	V _{max}	V _{min}	V	V _{max}
8/26/76	8	8		8		2.10	3.95	5.80
9/2/76	6	4-8	4	6	8	0.11	0.48	0.85
	8	4	4	6	8	0.90	1.05	1.20
10/1/76	6	6		6		3.00	6.00	9.00
10/4/76	15	15		15		3.80	6.40	9.00
10/6/76	3-4	2	2	2.7	3.5	0.09	0.34	0.60
10/18/76	10-12	10-12	10	11	12	3.30	3.65	4.00
10/29/76	10	10		10		2.10	2.65	3.20
11/5/76	3-4	2-3	2.5	3	3.5	0.035	0.097	0.150

These data were taken with coaxial transmitter-receiver alignment, 5.5 mRad transmitter beam divergence, and 1.0 mRad cone-angle receiver field of view. The minimum, nominal, and maximum visibilities, (V_{\min} , V , and V_{\max} respectively) are ad hoc estimates of a homogeneous-path visibility that would produce the same unscattered-light extinction as the Cambridge-to-Waltham path. The signal voltages, v_{\min} and v_{\max} are the minimum and maximum levels (corrected for the Wratten filters) reached in 15 seconds of boxcar averaging with an effective time constant of 4 sec; $v \equiv (v_{\min} + v_{\max})/2$.

Table 5. Holmium Laser Transmission Data: 20 mRad FOV

Date	Visibility in Miles				Signal Voltage			Point No.
	from Cambridge	from Waltham	V _{min}	V	V _{max}	v _{min}	v	
8/26/76	8	8		8		3.30	3.95	1
9/2/76	6	4-8	4	6	8	0.70	0.82	2
	8	4	4	6	8	1.30	1.50	3
10/1/76	6	6		6		5.20	7.10	4
10/4/76	15	15		15		7.60	9.30	5
10/6/76	3-4	2	2	2.7	3.5	0.12	0.46	6
10/18/76	10-12	10-12	10	11	12	2.80	3.40	7
10/29/76	10	10		10		2.40	2.70	8
11/5/76	3-4	2-3	2.5	3	3.5	0.100	0.112	9

These data were taken with coaxial transmitter-receiver alignment, 5.5 mRad transmitter beam divergence, and 20 mRad cone-angle receiver field of view. The minimum, nominal, and maximum visibilities (V_{min} , V , and V_{max} , respectively) are ad hoc estimates of a homogeneous-path visibility that would produce the same unscattered-light extinction as the Cambridge-to-Waltham path. The signal voltages, v_{min} and v_{max} , are the minimum and maximum levels (corrected for the Wratten filters) reached in 15 seconds of boxcar averaging with an effective time constant of 4 sec; $v = (v_{min} + v_{max})/2$.



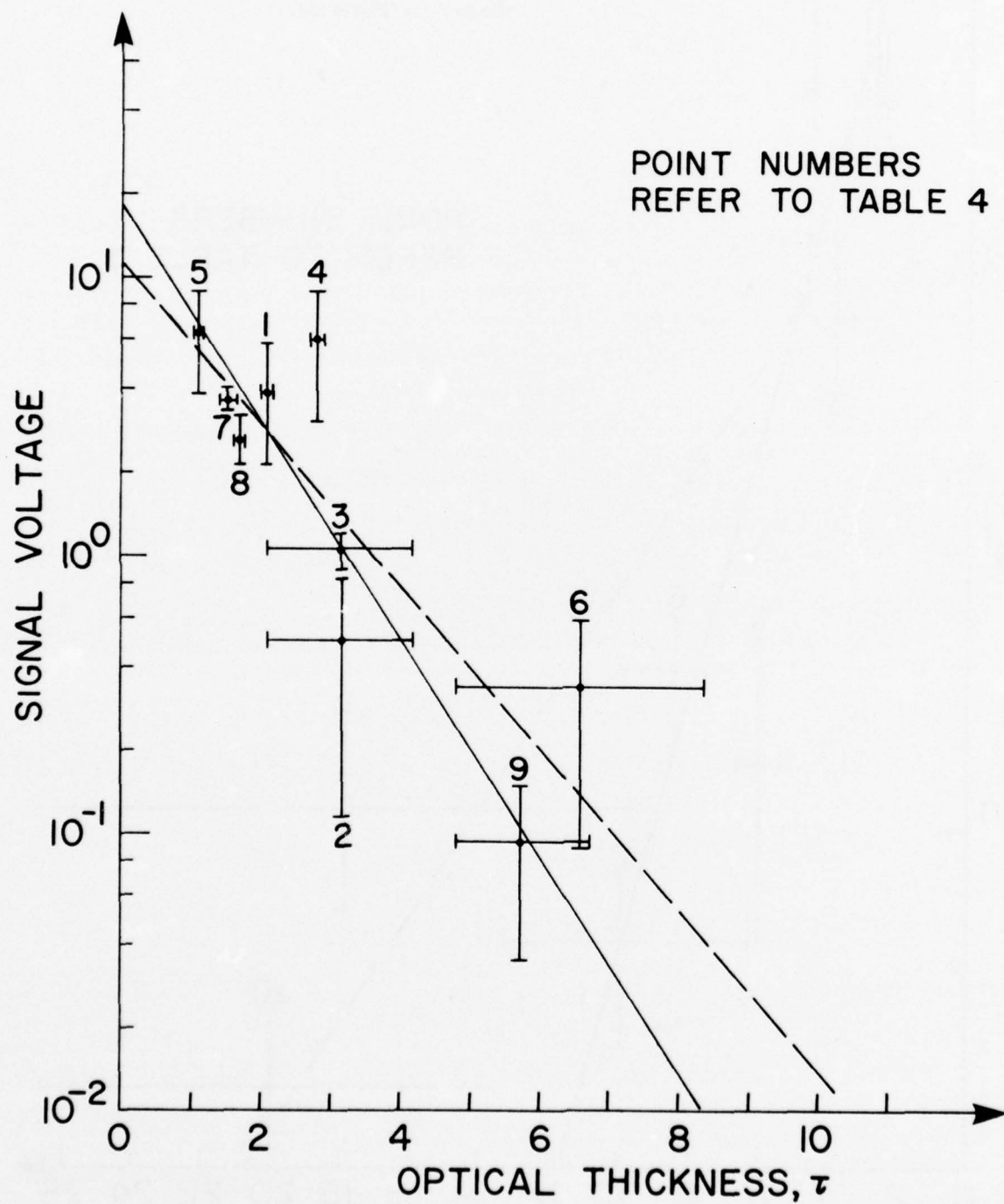


Fig. 22. Holmium-link signal vs optical thickness (based on Table 4).

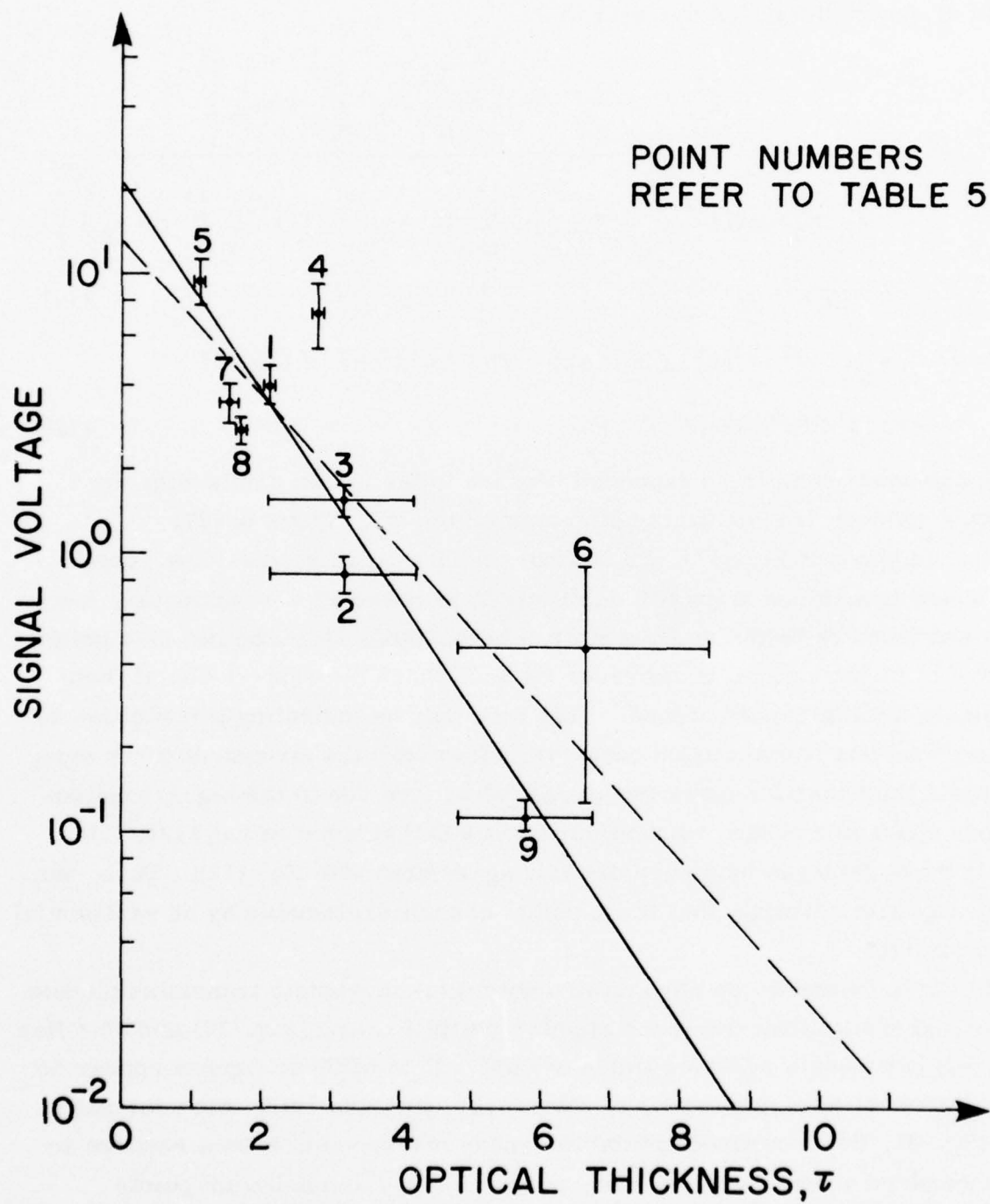


Fig. 23. Holmium-link signal vs optical thickness (based on Table 5).

exponential laws to the data. The dotted line in Fig. 21,

$$v = 7.09 \times 10^2 \exp(-0.46 \tau), \quad (10)$$

is a least-squares fit of an exponential curve to all 11 data points; the coefficient of determinism for Eq. (10) is

$$r^2 = \frac{\left[\sum_{n=1}^{11} \tau_n \ln v_n - (11)^{-1} \sum_{n=1}^{11} \tau_n \sum_{m=1}^{11} \ln v_m \right]^2}{\left[\sum_{n=1}^{11} \tau_n^2 - (11)^{-1} \left(\sum_{n=1}^{11} \tau_n \right)^2 \right] \left[\sum_{n=1}^{11} (\ln v_n)^2 - (11)^{-1} \left(\sum_{n=1}^{11} \ln v_n \right)^2 \right]} = 0.702 \quad (11)$$

where $\{(v_n, \tau_n): 1 \leq n \leq 11\}$ is the data. The solid line in Fig. 21,

$$v = 9.08 \times 10^3 \exp(-1.01 \tau), \quad (12)$$

is a least-squares fit of an exponential curve to the 9 data points with the lowest τ values; its coefficient of determinism, r^2 , equals 0.827.

On the basis of Eq. (12), we believe our 20 mRad field-of-view ruby-wavelength transmission profile definitely follows the $\exp(-\tau)$ extinction law for unscattered radiation at least to optical thickness 10. The two data points we have at higher optical thicknesses lie well above the $\exp(-\tau)$ line at their nominal optical thickness values. This data may be indicating a transition to diffusion-regime transmission behavior. However, the enormous error bars on optical thickness for these two points (which are due to the highly inhomogeneous character of the propagation conditions that were extant 11/5/76) permit these points to be placed in close agreement with Eq. (12). Thus, we cannot say with certainty that these points are not explainable by an exponential extinction law.

In Figs. 22 and 23 we have plotted holmium-wavelength transmission data for coaxial transmitter-receiver alignment with 1 mRad (Fig. 22) and 20 mRad (Fig. 23) cone-angle receiver fields of view. Both of these figures appear to follow exponential extinction laws. Moreover, they indicate, when compared with Fig. 21, the decreased optical thickness measured at 2.06μ relative to that measured at 694.3 nm (cf. ruby points 1, 2, 4, 9 and holmium points

4, 6, 7, 9). A least-squares fit of an exponential law to all 9 holmium data points yields the relationships

$$v = 1.11 \times 10^1 \exp(-0.66 \tau), \quad (13)$$

for the 1 mRad field of view, and

$$v = 1.24 \times 10^1 \exp(-0.63 \tau), \quad (14)$$

for the 20 mRad field of view. These equations (which are shown as dotted lines in Figs. 22 and 23) have coefficients of determinism 0.728 and 0.730, respectively. If we omit the data obtained on 10/6/76, because of its substantial error bars on optical thickness, we find the least-squares exponential curves (the solid lines in Figs. 22 and 23)

$$v = 1.87 \times 10^1 \exp(-0.90 \tau), \quad (15)$$

for the 1 mRad field of view, and

$$v = 2.05 \times 10^1 \exp(-0.86 \tau) \quad (16)$$

for the 20 mRad field of view, with coefficients of determinism 0.803 and 0.809, respectively. It might seem that there is a slightly slower than Bouguer-Lambert decay with optical thickness to our holmium data. Because of the small optical thicknesses in our data, however, it is more likely that Eq. (9), for obtaining 2.06μ optical thickness from visibility, is in error.

CHAPTER III. A THEORETICAL APPROACH

The angular spectra presented in Chapter II are at most a few milliradians wide, even for measurements made at about ten extinction lengths ($\tau = 10$). This narrowness could result from the field being dominated by unscattered light, but that explanation does not appear to be fully consistent with the data obtained when either the transmitter or the receiver are pointed off the optical axis (see Chapter II).

The observed narrowness and the uncertainty as to whether it was associated with the unscattered field led us to develop a theoretical approach for analyzing multiple-scatter propagation in the region where the fields possess such spectra. That approach, developed from the transport equation, is presented in this chapter. It differs from the approach that has been used so successfully to describe propagation in turbulence in that the particle scattering function is assumed to be either wide or smooth compared to the angular spectrum of the field.

The order of the chapter is as follows. In section A the description of photon propagation by the linear transport equation is briefly reviewed and the interpretation of the solution as a channel transfer function is given. In section B the equation is simplified by assuming that the angular spectrum of the field is narrow relative to the particle scattering function and the solution is reduced to the evaluation of inverse Fourier Transforms. Finally, in section C, the solution is obtained in detail for the isotropic scattering problem. This problem is probably not the one that best describes the scattering environment encountered in our measurements, but it does illustrate, in a relatively simple context, the approach that can be applied to that environment.

A. The Transport Equation

Our approach to multiple-scatter propagation is through the linear transport equation [28-30]. That is, the "field" is viewed as a collection of photons, each of which is characterized by its position \vec{r} and direction of propagation $\vec{\Omega}$ as functions of time t .

1. Formulation

The trajectory in $\vec{r}, \vec{\Omega}$ space followed by each photon as time evolves is realistically assumed to be a Markov process. That is, the statistical behavior of the trajectory for t greater than t' , given knowledge of the entire trajectory prior to t' , is identical to the behavior given only knowledge of the values of \vec{r} and $\vec{\Omega}$ at t' . Thus the probability density, $p(\vec{r}, \vec{\Omega}, t)$, for a photon to be at the position \vec{r} with a direction vector $\vec{\Omega}$ at the time t satisfies the Chapman Kolmogorov equation [31, 32]. Since changes in $\vec{\Omega}$ take place only at the discrete locations where a photon encounters a scattering particle, this equation reduces to the linear transport equation [28-30]

$$\left(\alpha + \frac{1}{c} \frac{\partial}{\partial t} + \vec{\Omega} \cdot \nabla \right) p(\vec{r}, \vec{\Omega}, t) = \int \beta S(\vec{\Omega} \cdot \vec{\Omega}') p(\vec{r}, \vec{\Omega}', t) d\vec{\Omega}'. \quad (17)$$

In Eq. (17) c is the velocity of light, ∇ is the gradient operator with respect to \vec{r} , $S(\vec{\Omega} \cdot \vec{\Omega}')$ is the particle scattering function and α and β are, respectively, the local extinction and scattering coefficients. In general both α and β can be functions of position but for simplicity we take them to be constant throughout the medium. Thus $\exp -\alpha r$ is the probability that the photon travels at least a distance r without encountering a particle, β/α is the probability that the photon will be scattered upon encountering a particle and $(\alpha-\beta)/\alpha$ is the probability that it will be absorbed.

The directional characteristics of the scattering particles are described by the scattering function $S(\vec{\Omega} \cdot \vec{\Omega}')$ which is the conditional probability density for a photon to be scattered in the direction $\vec{\Omega}$ given it is incident upon the scatterer with direction vector $\vec{\Omega}'$. Thus

$$\int S(\vec{\Omega} \cdot \vec{\Omega}') d\vec{\Omega} = 1, \quad (18)$$

where $d\vec{\Omega}$ denotes a differential surface element of the unit sphere. In spherical coordinates with $\vec{\Omega}'$ as the zenith direction

$$\int_0^{2\pi} d\phi \int_0^\pi d\theta \sin \theta S(\cos \theta) = 1 \quad (19)$$

In general, the scattering function can depend upon both $\vec{\Omega}$ and $\vec{\Omega}'$, rather than just upon their inner product and it can also depend upon position. The

assumption that it depends only upon $\vec{\Omega} \cdot \vec{\Omega}'$ is often realistic; the assumption that it is independent of position is made for simplicity.

For our purposes it is convenient to express Eq. (17) in terms of the Laplace transform, from t to s , of $p(\vec{r}, \vec{\Omega}, t)$ as an integral equation rather than an integro-differential equation. For photons produced at time $t = 0$ with an initial probability density in position and an angle of $P_0(\vec{r}, \vec{\Omega})$ the result is easily shown to be.

$$P(\vec{r}, \vec{\Omega}, s) = \beta \int_0^\infty d\nu \int d\vec{\Omega}' S(\vec{\Omega} \cdot \vec{\Omega}') P(\vec{r} - \nu \vec{\Omega}, \vec{\Omega}', s) \exp(-\nu \gamma) + S_u(\vec{r}, \vec{\Omega}) \quad (20a)$$

with

$$S_u(\vec{r}, \vec{\Omega}) \equiv \int_0^\infty d\nu P_0(\vec{r} - \nu \vec{\Omega}, \vec{\Omega}) \exp(-\gamma \nu) \quad (20b)$$

and

$$\gamma \equiv a + (s/c). \quad (20c)$$

Here $P(\vec{r}, \vec{\Omega}, s)$ is the Laplace transform of $p(\vec{r}, \vec{\Omega}, t)$:

$$P(\vec{r}, \vec{\Omega}, s) = \int_0^\infty dt p(\vec{r}, \vec{\Omega}, t) \exp(-st). \quad (21)$$

2. The Channel Frequency Response

In principle, the solution to Eq. (20a) can be inverse-transformed to obtain $p(\vec{r}, \vec{\Omega}, t)$ from which the multipath behavior of the channel can be inferred. However, it is simpler, and almost equally enlightening, to interpret the behavior in the s domain.

To develop that interpretation, suppose that the source produces photons at an instantaneous average rate of $\lambda(t)$ photons per second and that each generated photon is distributed in space and angle according to the probability density $P_0(\vec{r}, \vec{\Omega})$. Note that

$$\int d\vec{r} \int d\vec{\Omega} P_0(\vec{r}, \vec{\Omega}) = 1 \quad (22)$$

and that $\lambda(t)$ is nonnegative. We seek $\lambda(\vec{r}, \vec{\Omega}, t)$, the instantaneous average density of photons per second appearing at the position \vec{r} with a direction $\vec{\Omega}$ at the time t .

If $\lambda(t)$ were an impulse $\delta(t-\tau) \lambda(\tau)$ of area $\lambda(\tau)$ at time τ , $\lambda(\vec{r}, \vec{\Omega}, t)$ would be $\lambda(\tau) p(\vec{r}, \vec{\Omega}, t-\tau)$ where $p(\vec{r}, \vec{\Omega}, \cdot)$ is the inverse transform of $P(\vec{r}, \vec{\Omega}, s)$.

For the general time input $\lambda(t)$,

$$\lambda(\vec{r}, \vec{\Omega}, t) = \int d\tau \lambda(\tau) p(\vec{r}, \vec{\Omega}, t - \tau) \quad (23a)$$

or, in the transform domain,

$$\Lambda(\vec{r}, \vec{\Omega}, s) = \Lambda(s) P(\vec{r}, \vec{\Omega}, s) \quad (23b)$$

where $\Lambda(s)$ and $\Lambda(\vec{r}, \vec{\Omega}, s)$ are, respectively, the Laplace transforms of $\lambda(\tau)$ and $\lambda(\vec{r}, \vec{\Omega}, t)$. Thus $P(\vec{r}, \vec{\Omega}, s)$, the solution of Eq. (20), can be interpreted as the transfer function in the s domain, between the time variation in the average generation rate of the source and the average density of photons per second at \vec{r} with direction $\vec{\Omega}$.

Note that the interpretation of $P(\vec{r}, \vec{\Omega}, s)$ as the transfer function for the average photon rate does not require that different "photons" are independent. To the extent that they are independent, $P(\vec{r}, \vec{\Omega}, s)$ also determines the higher order moments of the flux. In particular, the variance of the local density of photons at $\vec{r}, \vec{\Omega}, t$ will be

$$\sigma^2(\vec{r}, \vec{\Omega}, t) = \lambda(\vec{r}, \vec{\Omega}, t). \quad (24)$$

More generally, in the low photon coherence approximation, the number of photons in the vicinity of $\vec{r}, \vec{\Omega}$ at the time t will be Poisson-distributed with a rate parameter $\lambda(\vec{r}, \vec{\Omega}, t)$ which is determined by $\lambda(t)$ through the transfer function $P(\vec{r}, \vec{\Omega}, s)$.

It should also be noted, for future reference, that $P(\vec{r}, \vec{\Omega}, 0)$ is just the time integral of $p(\vec{r}, \vec{\Omega}, t)$. Thus, from Eq. (23a), it is the ratio of the total average number of photons that are ever at the point \vec{r} with a direction vector $\vec{\Omega}$ to the total average number of photons emitted by the source. If these numbers are infinite, but their time averages are finite, $P(\vec{r}, \vec{\Omega}, 0)$ is the transfer function between these time-averaged quantities.

The transport equation is deceptively simple in appearance but has been solved for only isolated situations. Thus, to gain some insight into the experimental results discussed in section B, the approximation introduced at the beginning of this chapter will be developed.

B. An Approximation to the Transport Equation

The approximation to be employed was suggested by the observed narrowness of the width of $p(\vec{r}, \vec{\Omega}, t)$ in $\vec{\Omega}$ and will be developed in that way. A different condition which leads to the same result will then be described.

1. A Narrow Spectrum Approximation

Suppose that, in Eq. (20), $P(\vec{r} - \nu \vec{\Omega}, \vec{\Omega}', s)$ is concentrated in $\vec{\Omega}'$ about some direction $\vec{\Omega}_{\rho}$ which may depend upon $\vec{r} - \nu \vec{\Omega}$, denoted by $\vec{\rho}$. Specifically, suppose that the integrand in that equation vanishes when $\vec{\Omega}'$ and $\vec{\Omega}_{\rho}$ differ by an angle that is small with respect to the angular width of the particle scattering function $S(\cdot)$. To the extent that this is true, $P(\vec{r} - \nu \vec{\Omega}, \vec{\Omega}', s)$ behaves as an impulse in $\vec{\Omega}'$ relative to $S(\vec{\Omega} \cdot \vec{\Omega}')$ and the equation may be written as

$$P(\vec{r}, \vec{\Omega}, s) = \beta \int_0^\infty d\nu S(\vec{\Omega} \cdot \vec{\Omega}_{\rho}) P(\vec{r} - \nu \vec{\Omega}, s) \exp(-\nu \gamma) + S_u(\vec{r}, \vec{\Omega}) \quad (25a)$$

with

$$P(\vec{r}, s) \equiv \int P(\vec{r}, \vec{\Omega}, s) d\vec{\Omega} \quad (25b)$$

and, as before,

$$S_u(\vec{r}, \vec{\Omega}) = \int_0^\infty d\nu P_o(\vec{r} - \nu \vec{\Omega}, \vec{\Omega}) \exp(-\nu \gamma) \quad (25c)$$

Note that $P(\vec{r}, s)$ is the Laplace transform of $p(\vec{r}, t)$, the probability density that a photon generated at $t = 0$ will be at the point \vec{r} at the time t without regard to its direction of propagation. Equivalently $P(\vec{r}, s)$ is the transfer function relating $\lambda(t)$ to the average number of photons per unit volume at the position \vec{r} at the time t without regard to their direction of propagation.

It is instructive to note that $P(\vec{r}, \vec{\Omega}, s)$ will be narrow with respect to $\vec{\Omega}$, as claimed, only if the integral in Eq. (25a) vanishes whenever $\vec{\Omega}$ differs much from $\vec{\Omega}_{\rho}$, the direction about which $P(\vec{r}, \vec{\Omega}, s)$ is assumed to be concentrated. In particular, $P(\vec{r}, \vec{\Omega}, 0)$, the transfer function for average power or energy, will be narrow only if the nonnegative integrand satisfies

$$S(\vec{\Omega} \cdot \vec{\Omega}_{\rho}) P(\vec{r} - \nu \vec{\Omega}, 0) \exp(-\nu a) \approx 0 \quad \text{all } \nu \quad (26)$$

for any $\vec{\Omega}$ that differs from $\vec{\Omega}_{\vec{r}}$ by more than the nominal half-width, θ_c , of $P(\vec{r}, \vec{\Omega}, 0)$.

For large enough values of ν the required vanishing results from the exponential factor $\nu\alpha$. For smaller values of ν , in particular, for values of $\alpha\nu$ less than, say, five, either $S(\vec{\Omega} \cdot \vec{\Omega}_{\vec{r}})$ or $P(\vec{r} - \nu\vec{\Omega}, 0)$ must vanish whenever $\vec{\Omega}$ differs from $\vec{\Omega}_{\vec{r}}$ by more than θ_c . Since this width is assumed to be substantially less than that of $S(\cdot)$, the required vanishing can be caused by $S(\vec{\Omega} \cdot \vec{\Omega}_{\vec{r}})$ only if the angle between $\vec{\Omega}_{\vec{r}}$ and $\vec{\Omega}_{\vec{\rho}}$ nearly exceeds the halfwidth, θ_s , of $S(\cdot)$. Otherwise it must be $P(\vec{r} - \nu\vec{\Omega}, 0)$ that vanishes. These constraints are summarized in Fig. 24.

The requirements of Fig. 24 can be satisfied in a variety of ways, depending upon the geometry of the source and observation region. For the problems of interest here \vec{r} is typically located near the axis of symmetry of the source angular pattern. Were it not for scattering the position \vec{r} would be illuminated by the transmitted beam. For this situation, Fig. 24 requires that any "beam" that continues to exist in the presence of scattering must be such that the portions of it which lie outside the cone of half-angle θ_c and within a distance of a few α^{-1} of \vec{r} must be confined to the region where $\vec{\Omega}_{\vec{\rho}}$ and $\vec{\Omega}$ differ by more than θ_s .

For this requirement to be met exactly it is necessary that θ_c exceed θ_s — in violation of the assumption that led to Eq. (25). However, it will be approximately satisfied if the beam diameter is small with respect to the cone shown in Fig. 24, i. e., if the beam radius at \vec{r} is less than a few times $\alpha^{-1} \tan \theta_c$.

The foregoing argument suggests that the angular width of $P(\vec{r}, \vec{\Omega}, s)$ will be narrow as assumed only if the beam diameter is relatively small. This might in turn suggest that Eq. (25), which results from that approximation, is essentially a single scatter approximation. In fact, it is not. Indeed Eq. (25) is exactly the same as Eq. (20) for isotropic scatter; that is, when $S(\vec{\Omega} \cdot \vec{\Omega}')$ equals $1/(4\pi)$ for all values of $\vec{\Omega}$. Thus there is some reason to hope that Eq. (25) may provide a useful approximation to $P(\vec{r}, \vec{\Omega}, s)$ even when its angular width is not narrow.

That hope is reinforced by the fact that Eq. (25) can also be obtained from Eq. (20) when $S(\cdot)$ is sufficiently smooth. Specifically, the integral in Eq. (20)

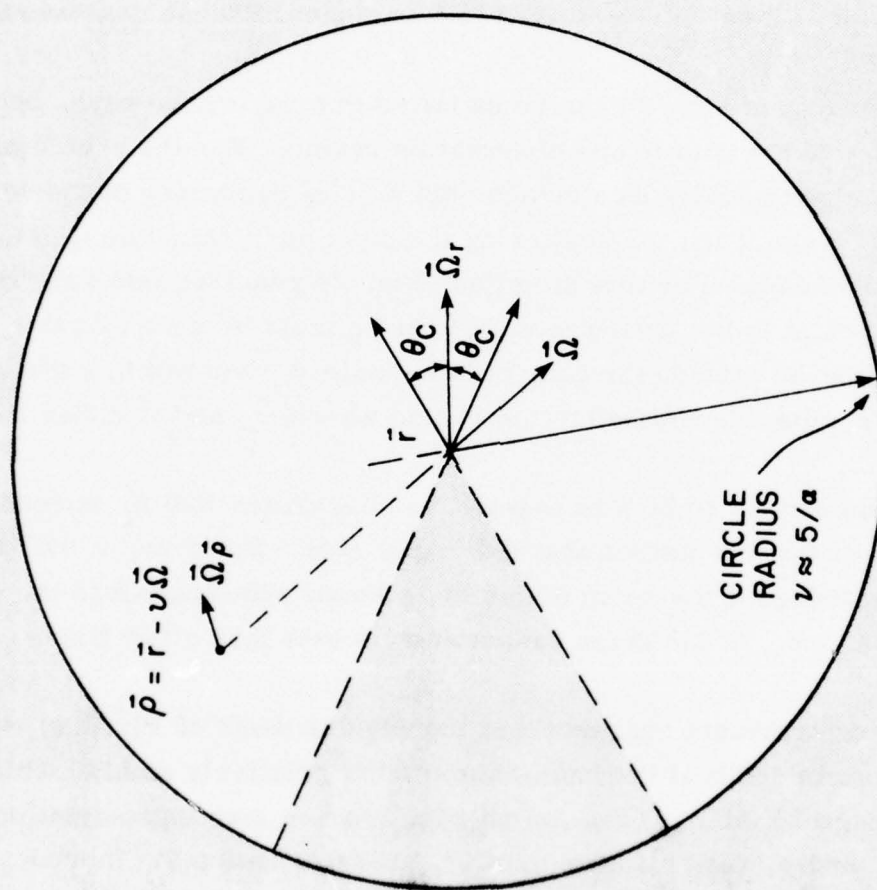


Fig. 24. Conditions for which $P(\vec{r}, \vec{\Omega}, 0)$ will be narrow. At each point $\vec{r} - v\vec{\Omega}$ outside the shaded region, either $\vec{\Omega}$ and $\vec{\bar{p}}$ must differ by more than θ_s or $P(\vec{r} - v\vec{\Omega}, 0)$ must be approximately zero.

can be evaluated by parts to yield an equation which differs from Eq. (25) only through the presence of an additional integral whose integrand involves products of the partial integral of $P(\vec{r}, \vec{\Omega}, s)$ with respect to $\vec{\Omega}$ and the partial derivatives of $S(\vec{\Omega} \cdot \vec{\Omega}')$ with respect to the components of $\vec{\Omega}'$. To the extent that the derivatives are negligible, Eq. (25) is obtained.

2. The Solution for $P(\vec{r}, s)$ and $P(\vec{r}, \vec{\Omega}, s)$

The principal advantage of Eq. (25) relative to Eq. (20) is that it can be solved more simply. In particular, a Fredholm integral equation for $P(\vec{r}, s)$ can be obtained by integrating Eq. (25) with respect to $\vec{\Omega}$. The result is, upon introducing $\vec{\rho} \equiv \vec{r} - v\vec{\Omega}$ and shifting to a volume integration,

$$P(\vec{r}, s) = \int d\vec{\rho} K(\vec{r} - \vec{\rho}) P(\vec{\rho}, s) + S_u(\vec{r}) \quad (27)$$

with

$$K(\vec{r} - \vec{\rho}) = \beta S(w) \frac{\exp -\gamma |\vec{r} - \vec{\rho}|}{|\vec{r} - \vec{\rho}|^2} \quad (28)$$

$$w = \frac{(\vec{r} - \vec{\rho})}{|\vec{r} - \vec{\rho}|} \cdot \frac{\vec{\Omega}}{\rho}$$

and

$$S_u(\vec{r}) = \int \frac{d\vec{\rho}}{\rho} \exp(-\gamma\rho) P_o(\vec{r} - \vec{\rho}, \vec{\rho}/\rho). \quad (29)$$

Since $\frac{\vec{\Omega}}{\rho}$ is the direction about which $P(\vec{\rho}, \vec{\Omega}, s)$ is concentrated in $\vec{\Omega}$, it must be determined before Eq. (27) can be solved for $P(\vec{r}, s)$. In principle, $\frac{\vec{\Omega}}{\rho}$ can be determined from Eq. (25), but for the beam geometries that will be considered here, it can reasonably be assumed to be along the nominal direction of the beam. We take that direction to be the positive z direction so that

$$\frac{\vec{\Omega}}{\rho} \approx \vec{I}_z. \quad (30)$$

With that choice Eq. (27) can be solved by Fourier transform techniques.

Specifically, let $\mathcal{P}(\vec{\omega}, s)$, $\kappa(\vec{\omega})$, and $S_u(\vec{\omega})$ be, respectively, the three-dimensional Fourier transforms of $P(\vec{r}, s)$, $K(\vec{r})$, and $S_u(\vec{r})$; e. g.,

$$\mathcal{P}(\vec{\omega}, s) = \int d\vec{r} P(\vec{r}, s) \exp(-j\vec{\omega} \cdot \vec{r}) \quad (31a)$$

and

$$P(\vec{r}, s) = \left(\frac{1}{2\pi}\right)^3 \int d\vec{\omega} \mathcal{P}(\vec{\omega}, s) \exp(j\vec{\omega} \cdot \vec{r}). \quad (31b)$$

In the transform domain Eq. (27) can be written as

$$\mathcal{P}(\vec{\omega}, s) = \kappa(\vec{\omega}) \mathcal{P}(\vec{\omega}, s) + \mathcal{S}_u(\vec{\omega}).$$

Thus

$$\mathcal{P}(\vec{\omega}, s) = \frac{\mathcal{S}_u(\vec{\omega})}{1 - \kappa(\vec{\omega})}$$

or, more conveniently for our purposes,

$$\mathcal{P}(\vec{\omega}, s) = \mathcal{S}_u(\vec{\omega}) + \frac{\kappa(\vec{\omega})}{1 - \kappa(\vec{\omega})} \mathcal{S}_u(\vec{\omega}) \quad (32)$$

It follows immediately from Eq. (32) that $P(\vec{r}, s)$ is given by

$$P(\vec{r}, s) = \mathcal{S}_u(\vec{r}) + \beta \int d\vec{\rho} h(\vec{r} - \vec{\rho}) \mathcal{S}_u(\vec{\rho}) \quad (33a)$$

with

$$h(\vec{r}) = \left(\frac{1}{2\pi}\right)^3 \int \frac{d\vec{\omega}}{\beta} \frac{\kappa(\vec{\omega})}{1 - \kappa(\vec{\omega})} \exp(j\vec{\omega} \cdot \vec{r}). \quad (33b)$$

The response function $h(\vec{r})$ can be interpreted as follows. Suppose the source function, $P_o(\vec{r}, \vec{\Omega})$, equals $\delta(\vec{r}) S(\vec{\Omega} \cdot \vec{\ell}_z)$, i. e., a point source with an angular pattern $S(\vec{\Omega} \cdot \vec{\ell}_z)$ is located at the origin. Then $\mathcal{S}_u(\vec{r})$ equals $K(\vec{r})/\beta$, $\mathcal{S}_u(\vec{\omega})$ equals $\kappa(\vec{\omega})/\beta$ and, for this source, $P(\vec{r}, s)$ equals $h(\vec{r})$ as defined by Eq. (33b). That is, $h(\vec{r})$ is $P(\vec{r}, s)$ for a point source located at the origin whose angular distribution is $S(\vec{\Omega} \cdot \vec{\ell}_z)$. It is as though the source is a single scatterer, located at the origin, illuminated by photons propagating along the z axis.

For a general source, the first term in Eq. (33a) is the contribution to $P(\vec{r}, s)$ of the photons that have not been scattered and the second term is the integral of the product of $\beta S(\vec{\rho})$, which is the probability that a source photon

is first scattered at the point $\vec{\rho}$ and $h(\vec{r} - \vec{\rho})$, which is the contribution of that "point" source to $P(\vec{r}, s)$.

Once $P(\vec{r}, s)$ has been determined through Eq. (33), $P(\vec{r}, \vec{\Omega}, s)$ can be evaluated from Eq. (25).

Time has not permitted an exploration of Eqs. (33) nor of the domain of validity of Eq. (25). However, the solution for the isotropic scatter problem has been obtained. For it, we will find that the angular spectrum will not be narrow when ar is much larger than one. Also, when ar is substantially larger than one, the bandwidth over which $P(\vec{r}, s)$ is constant in magnitude is limited to about $0.32 c\beta/(ar)^2$ rad/sec when $\alpha = \beta$ and about $1.8 c\sqrt{\beta/r} [(a/\beta) - 1]^{3/4}$ rad/sec when α and β are nearly, but not exactly, equal. Thus, as might be expected from the scattering characteristics of hazes and fogs [1, 9, 26], our experimental data are consistent with the theoretical results for isotropic scatter only when the field is dominated by unscattered radiation.

C. Isotropic Scatter

The isotropic scatter problem, for which $S(\vec{\Omega} \cdot \vec{\ell}_z)$ equals $1/4\pi$, has been considered by others, beginning apparently with Case et al. [33]. The results presented here differ from those earlier ones primarily through the presence of the Laplace variable s .

1. Isotropic Point Source

For isotropic scatter Eq. (28) becomes

$$S(\vec{\Omega} \cdot \vec{\ell}_z) = 1/4\pi$$

$$K(\vec{r}) = \frac{\beta \exp(-\gamma r)}{4\pi r^2} \quad (34)$$

$$\kappa(\vec{\omega}) = \frac{\beta}{2j\omega} \ln \frac{\gamma + j\omega}{\gamma - j\omega} \quad (35a)$$

or equivalently

$$\kappa(\vec{\omega}) = \frac{\beta}{\omega} \tan^{-1} \frac{\omega}{\gamma} \quad (35b)$$

Here ω denotes the magnitude of $\vec{\omega}$ and the branch of the logarithm is chosen so that $\kappa(\vec{\omega}) = \beta/\gamma$ for $\omega = 0$.

Introducing Eq. (35) into Eq. (33b) yields

$$h(\vec{r}) = \left(\frac{1}{2\pi}\right)^3 \int \frac{d\vec{\omega}}{\omega} \frac{\tan^{-1}(\omega/\gamma)}{1 - \frac{\beta}{\omega} \tan^{-1} \frac{\omega}{\gamma}} \exp(j\vec{\omega} \cdot \vec{r}). \quad (36)$$

For $s = 0$, the integral in Eq. (36) reduces to that evaluated by Case et al. [33]. The evaluation for general imaginary values, $j\omega_m$, of s is carried out in Appendix I. The result is, for nonnegative values of ω_m ,

$$h(\vec{r}) = \frac{A(\omega_m) \exp(j\omega_p r)}{2\pi r} + \epsilon(ar, j\omega_m) \frac{\exp(-ar)}{4\pi r^2} \quad (37)$$

where

$$A(\omega_m) = \begin{cases} \frac{\omega_p^2}{\beta \left[1 - \frac{\beta \gamma}{\gamma^2 + \omega_p^2} \right]} & \text{for } |\omega_m| \leq \omega_c \\ 0 & \text{for } |\omega_m| \geq \omega_c \end{cases} \quad (38a)$$

Here,

$$\gamma = a + \frac{s}{c} = a + j \frac{\omega_m}{c}, \quad (38b)$$

ω_c is the unique positive solution of

$$\frac{\beta}{a} \left(\frac{\pi a c}{2 \omega_c} \right) = \coth \left(\frac{\pi a c}{2 \omega_c} \right), \quad (39)$$

and ω_p is that unique solution of

$$\frac{1}{2(j\omega_p/\gamma)} \ln \frac{1 + (j\omega_p/\gamma)}{1 - (j\omega_p/\gamma)} = \frac{\gamma}{\beta} \quad (40)$$

whose imaginary part is nonnegative with the branch of the logarithm chosen so that $\ln(1)$ is zero. The function $\epsilon(ar, j\omega_m)$ is given by

$$\epsilon(ar, j\omega_m) = \gamma r (\exp ar) \int_1^\infty dv \left\{ \left[1 - \frac{\beta}{\gamma v} \coth^{-1} v \right]^2 + \left(\frac{\pi \beta}{2 \gamma v} \right)^2 \right\}^{-1} \exp(-\gamma r v). \quad (41)$$

Since $h(\vec{r})$ is the Fourier transform (from t to ω_m) of a real quantity, it possesses conjugate symmetry in ω_m . Thus the above results determine its value for negative values of ω_m as well as positive values.

The first term in Eq. (37) does not tend to zero as ω_m tends to ω_c . In fact, as shown in the appendix, ω_p then tends to $(\pi \beta \gamma c)/(2 \omega_c)$. Thus it might appear that $h(\vec{r})$ changes discontinuously at $\omega_m = \omega_c$. However, it can be shown that $\epsilon(ar, j\omega_m)$ also changes discontinuously as ω_m changes from ω_c^- to ω_c^+ and that $h(\vec{r})$ is continuous, as one would expect.

The term $\epsilon(ar, j\omega_m)[\exp(-\gamma r)]/[4\pi r^2]$ in the expression for $h(\vec{r})$ depends upon a, β, r and ω_m in a complicated way. However, it contributes little to $h(\vec{r})$ when ar is appreciably larger than one, so little that we will subsequently neglect it. To justify that neglect, note that $h(\vec{r})$ evaluated for $\omega_m = 0$ gives the total average number of photons that are ever in the vicinity of the point \vec{r} when the source is an impulse in time and gives the average number of photons per second there when an unmodulated source is employed. The contribution of the term in question to either of these averages is $\epsilon(ar, 0)[\exp(-ar)]/[4\pi r^2]$.

Examination of Eq. (41) shows that

$$\epsilon(ar, 0) \leq [ar \exp(ar)] \int_1^\infty dv \left(\frac{2av}{\pi\beta} \right)^2 \exp(-arv) \quad (42)$$

or, upon evaluating the integral,

$$\epsilon(ar, 0) \leq \left(\frac{2a}{\pi\beta} \right)^2 \left[1 + \frac{2}{ar} \left(1 + \frac{1}{ar} \right) \right]. \quad (43)$$

Thus the average energy or power carried by the term of Eq. (37) containing $\epsilon(ar, j\omega_m)$ decays with r at least as rapidly as the unscattered field. Moreover, its value is bounded by five times that of the unscattered field if ar exceeds one and β/a exceeds $2/\pi$. For the low absorption problems of interest to us β/a will always exceed $2/\pi$. Thus the term in question can be neglected almost as safely as can the unscattered field. Henceforth it will be.

To the extent that the second term of Eq. (37) is neglected,

$$h(\vec{r}) \approx \frac{A(\omega_m) \exp(-ar\eta)}{2\pi r} \quad (44)$$

where

$$\eta \equiv -j\omega_p/a.$$

In this approximation, $h(\vec{r})$ is zero for $\omega_m > \omega_c$ since $A(\omega_m)$ then equals zero. For $\omega_m < \omega_c$, the behavior of $h(\vec{r})$ is dominated by $\exp(-ar\eta)$ when ar is substantially greater than one. Note that since ω_p is that solution of Eq. (40) whose imaginary part is nonnegative, the real part of η is nonnegative.

For ω_m equal to zero η is real. Its value, as originally determined by Case et al. [33] is plotted as a function of β/a in Fig. 25. Note that η vanishes when a/β equals one, i. e., when there is no absorption. In that instance $h(\vec{r})$ does not decay exponentially with r but only as $1/r$. This corresponds to the diffusion mode discussed in Chapter II.

When both absorption and scattering are present ($a \neq \beta \neq 0$) $h(\vec{r})$ does decay exponentially with r but less rapidly than does the unscattered field. However, for the decay rate to be no larger than one fifth of the unscattered decay rate ($\eta < 0.2$), β/a must exceed 0.985. That is, only a small amount of absorption can be tolerated if the decay rate ηar is to be substantially less than that of the unscattered field.

The variation of ω_c , the frequency above which $A(\omega_m)$ vanishes, is shown in Fig. 26 as a function of β/a . As noted earlier, when ω_m equals ω_c , ω_p equals $(\pi\beta\gamma c)/(2\omega_c)$. Thus at $\omega_m = \omega_c$ the real part of η equals $(\pi\beta)/(2a)$ and the imaginary part equals $-(\pi\beta c)/(2\omega_c)$. Note that $\omega_c/(\beta c)$ is on the order of 1.4 for β/a greater than 0.5 and the imaginary part of η is then about one. For β nearly equal to a the real part of η is approximately 1.6.

In Figs. 27 and 28 the real and imaginary parts of η are plotted as functions of $\omega_m/(c\beta)$ for $a/\beta = 1, 1.04$, and 1.11 . These ratios correspond to ratios of absorption to scattering cross sections, $(a-\beta)/\beta$, of 0, 0.04, and 0.11. Note that as the absorption increases with β fixed the real and imaginary parts of η vary less rapidly with ω_m for $\omega_m/(\beta c) \lesssim 0.1$. Thus the useful bandwidth increases with adsorption as one expects.* However, this increase is obtained at the expense of an increased attenuation at all frequencies.

Although it is not apparent in the log-linear plot of Fig. 28, the imaginary part of η is a nearly linear function of ω_m for $\omega_m/(c\beta)$ less than about 0.04 and 0.11 when $(a-\beta)/\beta$ is, respectively, 0.04 or 0.11. This can be seen in Fig. 29 where part of Fig. 28 has been replotted on a linear scale.

The same conclusion is reached by noting that the asymptotic solution of Eq. (40) for $a \approx \beta$ and ω_m small yields

* The other factor, ar , in the exponent will increase somewhat with the increase in absorption just described, but for β/a near one the effect will not be significant.

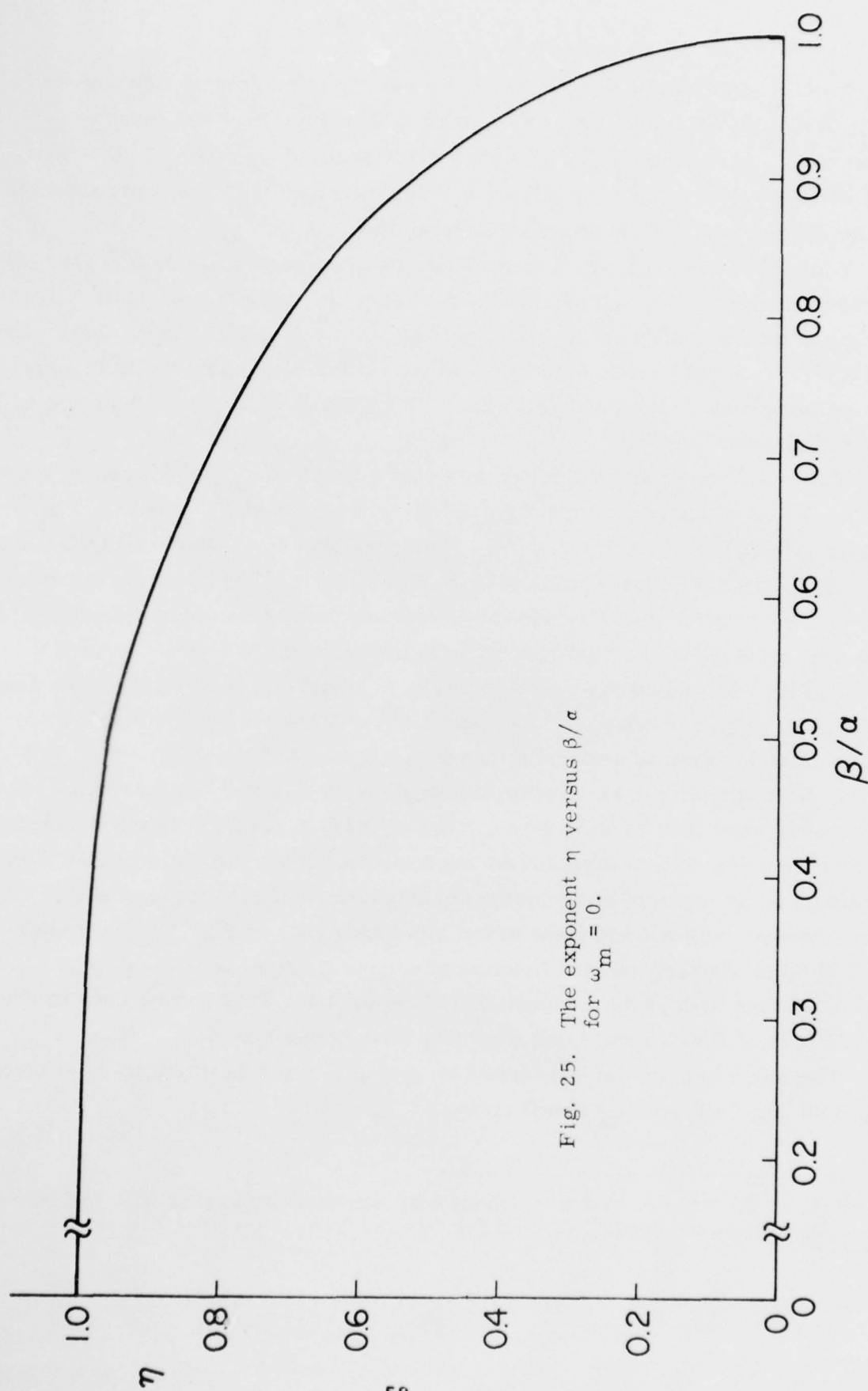


Fig. 25. The exponent η versus β/α
for $\omega_m = 0$.

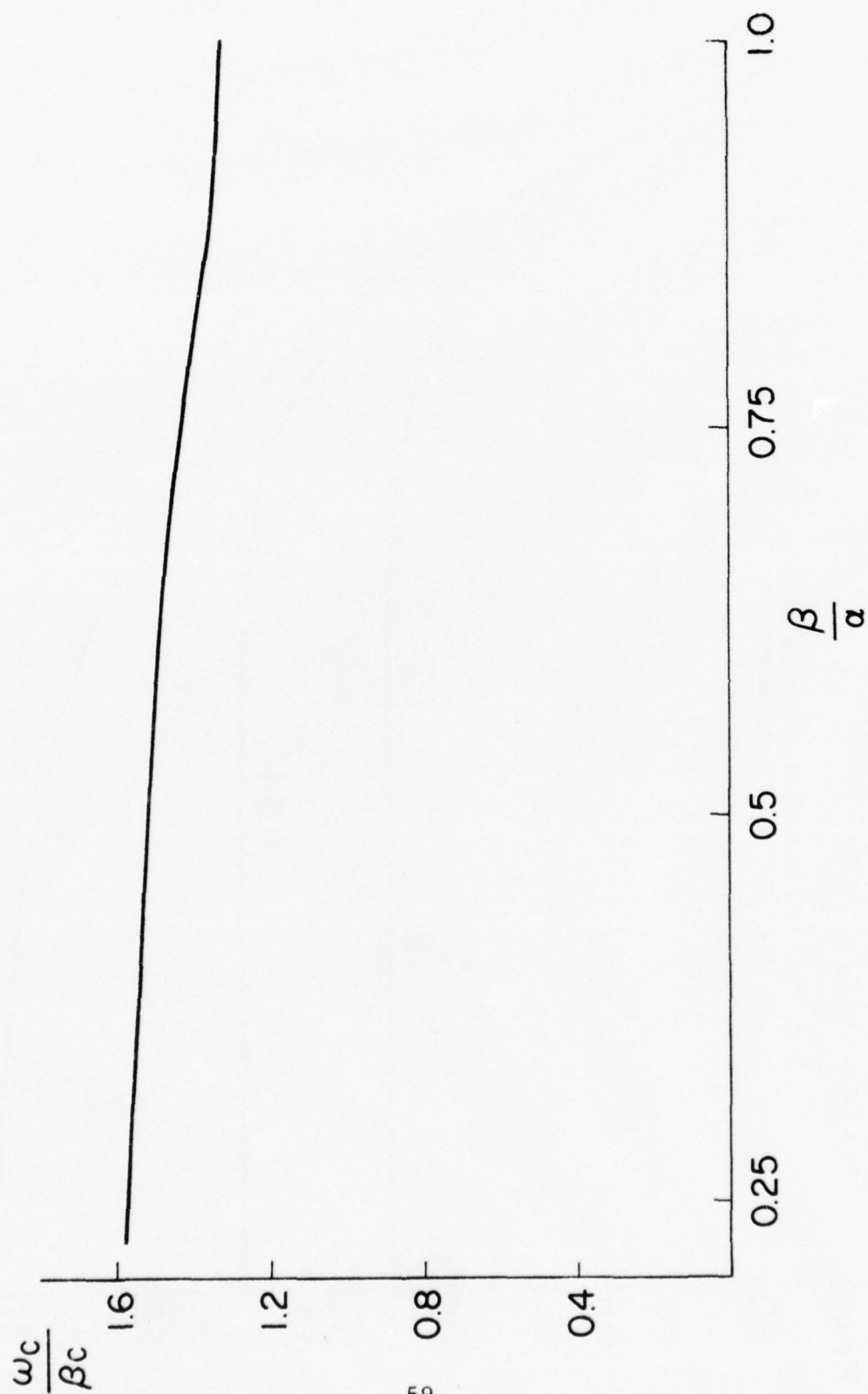


Fig. 26. The cutoff frequency ω_c/β_c versus β/a .

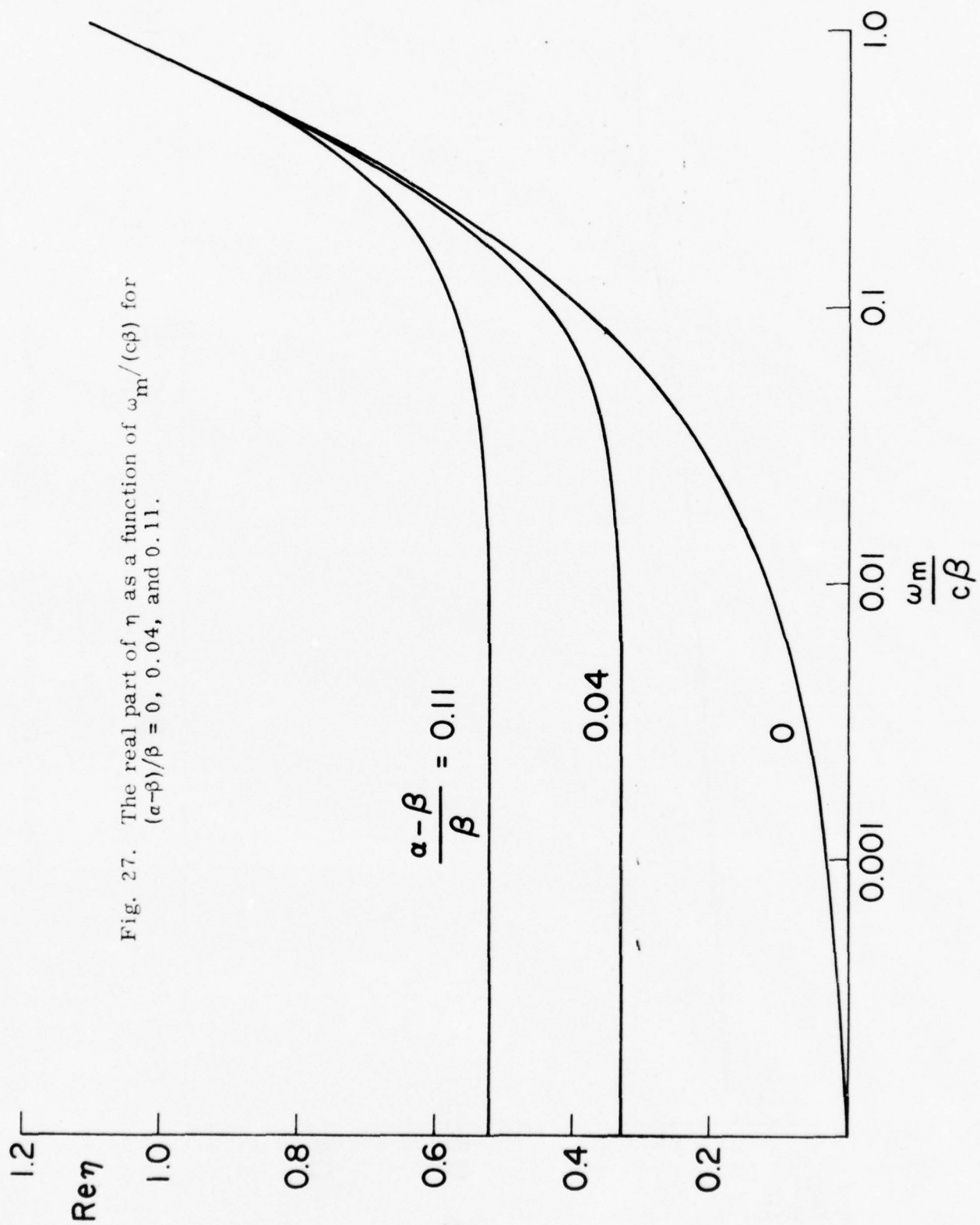


Fig. 27. The real part of η as a function of $\omega_m/(c\beta)$ for $(\alpha-\beta)/\beta = 0, 0.04$, and 0.11 .

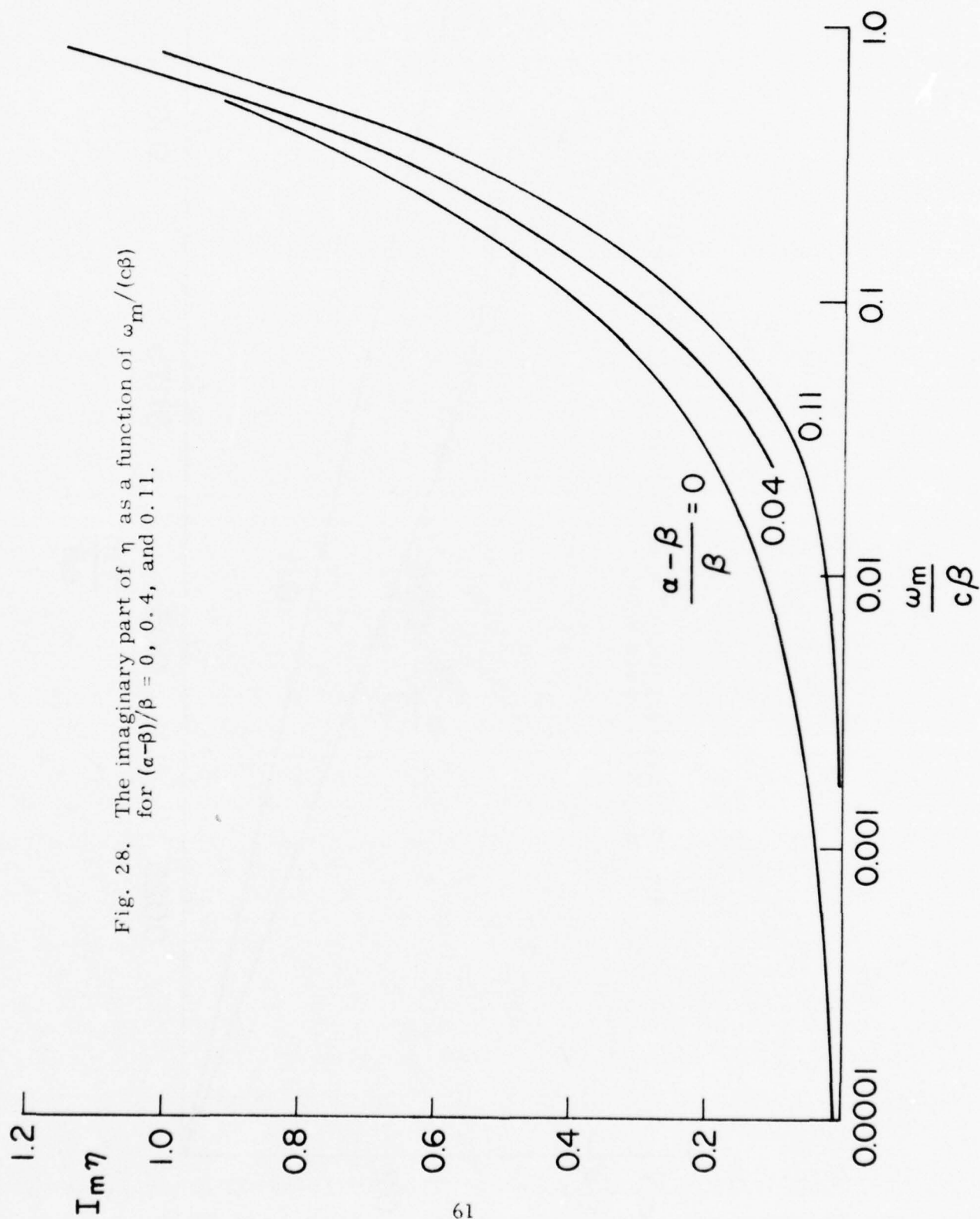


Fig. 28. The imaginary part of η as a function of $\omega_m/(c\beta)$ for $(\alpha - \beta)/\beta = 0, 0.4$, and 0.11 .

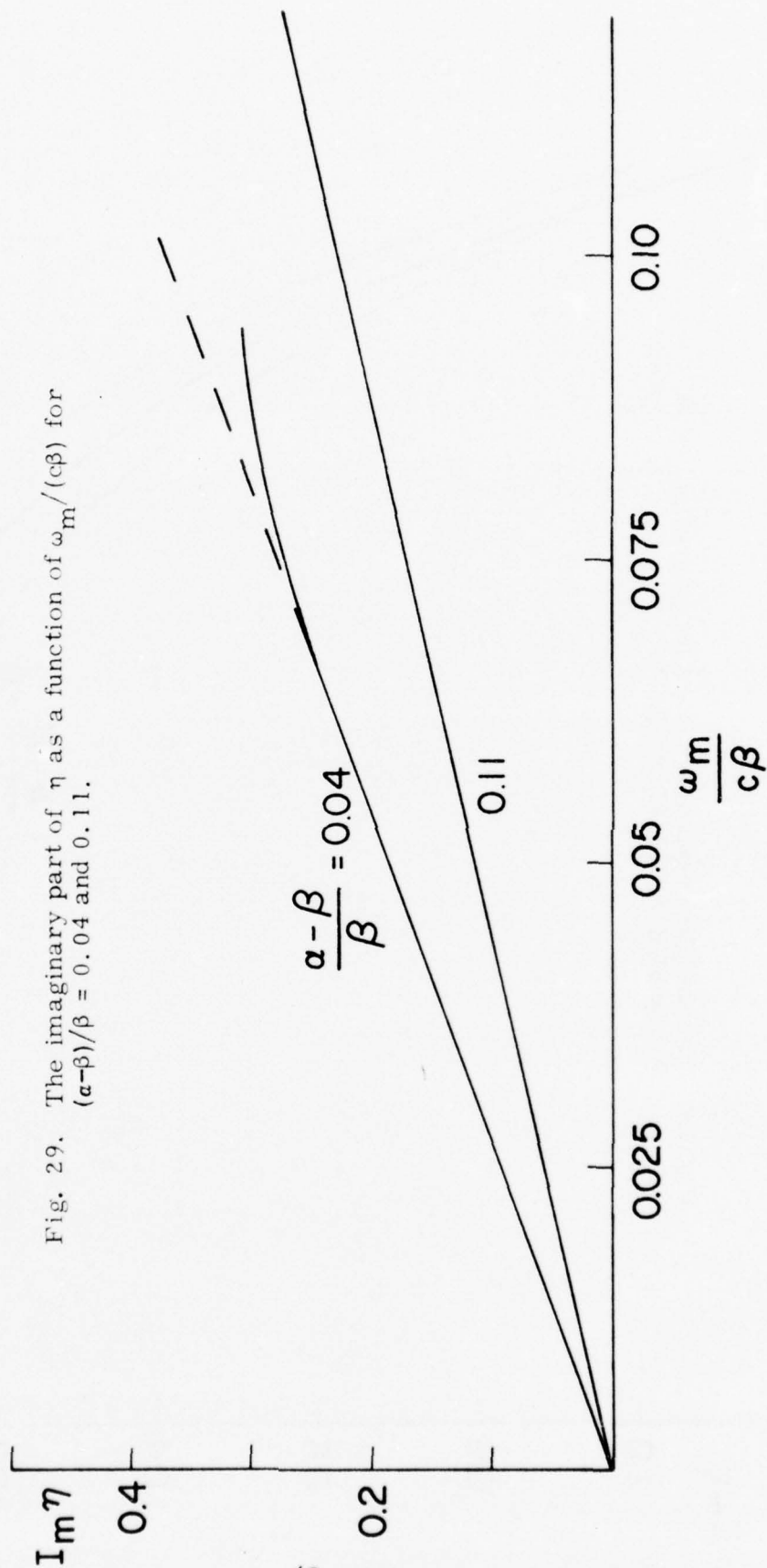


Fig. 29. The imaginary part of η as a function of $\omega_m/(c\beta)$ for $(\alpha-\beta)/\beta = 0.04$ and 0.11.

$$\eta = \frac{\beta}{\alpha} \sqrt{3} \sqrt{\frac{\alpha - \beta}{\beta} + j \frac{\omega_m}{c\beta}}. \quad (45)$$

Examination of this expression shows that the real part of η will be nearly constant and the imaginary part nearly linear in $\omega_m/(c\beta)$ when $\omega_m/(c\beta)$ is substantially less than $(\alpha - \beta)/\beta$, i. e., less than 0.04 and 0.011 for the two situations just discussed.

Equation (45) can also be used to estimate the nominal 3 dB bandwidth of the exponential factor $\exp(-\alpha r \eta)$ when αr is substantially larger than one. For then $\exp(-\alpha r \eta)$ will change by a factor of two when η changes only slightly, and the bandwidth can be estimated from

$$0.693 = (\alpha r) \frac{\beta}{\alpha} \sqrt{3} \left\{ - \sqrt{\frac{\alpha - \beta}{\beta}} + \operatorname{Re} \sqrt{\frac{\alpha - \beta}{\beta} + j \frac{\omega_b}{c\beta}} \right\}, \quad (46)$$

where ω_b denotes the value of ω_m for which the real part of $(\alpha r \eta)$ increases from its zero frequency value by 0.693.

When there is no absorption ($\alpha = \beta$) the solution of Eq. (46) is

$$\frac{\omega_b}{c\beta} = \frac{0.32}{(\alpha r)^2}.$$

On the other hand, if there is some absorption and αr is enough larger than one, the solution approaches

$$\frac{\omega_b}{c\beta} = \frac{1.8}{\sqrt{\alpha r}} \sqrt{\frac{\alpha}{\beta}} \left(\frac{\alpha - \beta}{\beta} \right)^{3/4}.$$

For large optical thicknesses, αr , the increase in bandwidth that results from the presence of a small amount of absorption is substantial.

2. Ray Source

The density $P(\vec{r}, s)$ is equal to $h(\vec{r})$ for a point source that radiates uniformly in all directions. For a point source with an angular radiation pattern $S_0(\Omega \cdot \vec{l}_z)$, $P(\vec{r}, s)$ is, by virtue of Eq. (33a),

$$P(\vec{r}, s) = S_u(\vec{r}) + \beta \int d\vec{\rho} h(\vec{r} - \vec{\rho}) S_u(\vec{\rho}),$$

where $S_u(\vec{r})$, the unscattered field is, from Eq. (29),

$$S_u(\vec{r}) = \frac{\exp(-\gamma r)}{r^2} S_o\left(\frac{\vec{r} \cdot \vec{\ell}_z}{r}\right). \quad (47)$$

We ignore the unscattered field term $S_u(\vec{r})$ in the expression for $P(\vec{r}, s)$ and focus on the remaining term. That term has a component involving the function $\epsilon(\cdot, j\omega_m)$ defined in Eq. (41). As discussed in conjunction with Eq. (43), its contribution is not significant when ar is large. Thus, as there, it will be neglected here. The remaining term is

$$P(\vec{r}, s) = \beta A(\omega_m) \int \frac{d\vec{\rho} S_u(\vec{\rho})}{2\pi |\vec{r} - \vec{\rho}|} \exp(j\omega_p |\vec{r} - \vec{\rho}|). \quad (48)$$

The properties of $P(\vec{r}, s)$ have already been determined, through $h(\vec{r})$, for an isotropic point source. To see the effect of source collimation, the other extreme of a ray source will be considered.

Specifically, suppose that $S_o(\vec{\Omega} \cdot \vec{\ell}_z)$ is an impulse in solid angle, in the direction $\vec{\ell}_z$. Then

$$S_u(\vec{r}) = \frac{\exp(-\gamma z)}{z^2} \delta(\vec{\rho}),$$

where $\delta(\cdot)$ is a two-dimensional impulse, $\vec{\rho}$ is the component of \vec{r} perpendicular to $\vec{\ell}_z$, and z is the projection of \vec{r} on $\vec{\ell}_z$. Consequently,

$$P(\vec{r}, s) \approx \frac{\beta A(\omega_m)}{2\pi} \int_0^\infty d\nu \frac{\exp(j\omega_p \sqrt{\rho^2 + (z-\nu)^2})}{\sqrt{\rho^2 + (z-\nu)^2}} \exp(-\gamma\nu), \quad (49)$$

where ρ is the length of $\vec{\rho}$.

The integral cannot be evaluated in closed form but its essential properties can be displayed through integration by parts. To this end, define

$$-\gamma\nu + j\omega_p \sqrt{\rho^2 + (z-\nu)^2} = f(\nu)$$

and write

$$P(\vec{r}, s) = -\frac{\beta A(\omega_m)}{2\pi} \int_0^\infty dv \frac{[f'(v) \exp f(v)]}{\gamma \sqrt{\rho^2 + (z-v)^2} + j\omega_p(z-v)},$$

where $f'(v)$ denotes the derivative of $f(v)$. Integration by parts yields

$$P(\vec{r}, s) = \frac{\beta A(\omega_m) \exp(j\omega_p r)}{2\pi(\gamma r + j\omega_p z)} (1 - \mathcal{R}) \quad (50a)$$

with

$$\mathcal{R} = (\gamma r + j\omega_p z) \int_0^\infty dv \frac{\left[\gamma(z-v) + j\omega_p \sqrt{\rho^2 + (z-v)^2} \right] \exp \left\{ j\omega_p \left[\sqrt{\rho^2 + (z-v)^2} - r \right] - \gamma v \right\}}{\sqrt{\rho^2 + (z-v)^2} \left[j\omega_p(z-v) + \gamma \sqrt{\rho^2 + (z-v)^2} \right]^2} \quad (50b)$$

where

$$r = \sqrt{\rho^2 + z^2}.$$

It is not difficult to show that, asymptotically,

$$\mathcal{R} \sim \frac{\gamma z + j\omega_p r}{(\gamma r + j\omega_p z)^2} \quad (51)$$

as z tends to plus infinity with either ρ or ρ/z fixed and nonzero. It can further be shown that when ω_p equals zero, \mathcal{R} is a function of only az and ρ/z .

The behavior of \mathcal{R} strongly suggests that $P(\vec{r}, s)$ approaches

$$\frac{\beta/(2\pi)}{\gamma + (j\omega_p z/r)} \cdot \left\{ \frac{A(\omega_m)}{r} \exp(j\omega_p r) \right\}$$

rapidly as γr exceeds unity – at least when ρ is not zero. The behavior for $\rho = 0$ is more complicated since $P(\vec{r}, s)$ contains some unscattered contribution along the z axis ($\rho = 0$). However, if this component is locally integrated over a small area about the axis, it is found that the result converges to the local

integral of the above expression. Since that expression is just $h(\vec{r})$ divided by $[(\gamma/\beta) + (j\omega_p z/\beta r)]$, the field differs from that produced by an isotropic point source only by $[(\gamma/\beta) + (j\omega_p z/\beta r)]$ once γr appreciably exceeds unity. Indeed, when $\alpha = \beta$ and $\omega_m = 0$, in which case $\omega_p = 0$, Eq. (50a) becomes

$$P(\vec{r}, s) \sim h(\vec{r}) \left(1 - \frac{z}{ar^2}\right).$$

3. The Angular Spectrum

Finally, let us determine $P(\vec{r}, \vec{\Omega}, s)$ from Eq. (25). Since $P(\vec{r}, s)$ for an isotropic point source and a ray source differ only slightly, an isotropic source will be considered. Also, the unscattered component of $P(\vec{r}, \vec{\Omega}, s)$ will be ignored and only the dominant term, $A(\omega_m)[\exp(j\omega_p r)]/(2\pi r)$, of $P(\vec{r}, s)$ will be used in the integral. Subject to these conditions, Eq. (25) becomes

$$P(\vec{r}, \vec{\Omega}, s) = \frac{\beta A(\omega_m)}{8\pi^2} \int_0^\infty dv \frac{\exp(j\omega_p |\vec{r} - v\vec{\Omega}|)}{|\vec{r} - v\vec{\Omega}|} \exp(-\gamma v). \quad (52)$$

Upon denoting by z the projection of \vec{r} on $\vec{\Omega}$ and by ρ the length of the component of \vec{r} perpendicular to $\vec{\Omega}$, Eq. (52) can be restated as

$$P(\vec{r}, \vec{\Omega}, s) = \frac{\beta A(\omega_m)}{8\pi^2} \int_0^\infty dv \frac{\exp(j\omega_p \sqrt{\rho^2 + (z-v)^2})}{\sqrt{\rho^2 + (z-v)^2}} \exp(-\gamma v)$$

The right-hand member of this equation differs from that of Eq. (49) only by a factor of 4π . Thus the argument that led from Eq. (49) to Eq. (50) can be repeated here. Specifically, if z tends to infinity with either ρ or ρ/z fixed, $P(\vec{r}, \vec{\Omega}, s)$ converges to

$$P(\vec{r}, \vec{\Omega}, s) \sim \frac{\beta A(\omega_m) \exp(j\omega_p r)}{8\pi^2 (\gamma r + j\omega_p z)} \left[1 - \frac{\gamma z + j\omega_p r}{(\gamma r + j\omega_p z)^2} \right]. \quad (53)$$

As with Eq. (50b), $P(\vec{r}, \vec{\Omega}, s)$ includes an impulsive term when $\rho = 0$ ($\vec{\Omega}$ in the direction of \vec{r}). However, if $P(\vec{r}, \vec{\Omega}, s)$ is integrated over a small solid angle

about the direction \vec{r} , the singularity is removed and the result is given by Eq. (53) integrated over the same solid angle.

Finally, it is convenient to express Eq. (53) in terms of the angle θ between $\vec{\Omega}$ and \vec{r} . Then $z = r \cos \theta$, $\rho = r \sin \theta$, and the conditions on Eq. (53) become that r increases with either θ or $r \sin \theta$ fixed. The evaluation itself becomes

$$P(\vec{r}, \vec{\Omega}, s) \sim \frac{\beta A(\omega_m) \exp(j\omega_p r)}{4\pi r(\gamma + j\omega_p \cos \theta)} \left[1 - \frac{\gamma \cos \theta + j\omega_p}{r(\gamma + j\omega_p \cos \theta)^2} \right]$$

or equivalently

$$P(\vec{r}, \vec{\Omega}, s) \sim \frac{\beta}{4\pi(\gamma + j\omega_p \cos \theta)} \left[1 - \frac{\gamma \cos \theta + j\omega_p}{r(\gamma + j\omega_p \cos \theta)^2} \right] P(\vec{r}, s). \quad (54)$$

Note that $P(\vec{r}, \vec{\Omega}, s)$ is a very weak function of θ whenever $j\omega_p$ differs substantially from γ . Indeed, if $\omega_m = 0$ and $\alpha = \beta$, in which case $\omega_p = 0$,

$$P(\vec{r}, \vec{\Omega}, s) \sim \frac{P(\vec{r}, s)}{4\pi} \left(1 - \frac{\cos \theta}{ar} \right)$$

and $P(\vec{r}, \vec{\Omega}, s)$ quickly becomes uniform in $\vec{\Omega}$ as ar exceeds one.

References

- [1] W. E. K. Middleton, Vision through the Atmosphere, Toronto: Univ. of Toronto Press, 1958.
- [2] T. S. Chu and D. C. Hogg, "Effects of Precipitation on Propagation at 0.63, 3.5, and 10.6 microns," *Bell Syst. Tech. J.*, Vol. 47, June 1968, pp. 723-761.
- [3] N. S. Kopeika and J. Bordogna, "Background Noise in Optical Communication Systems," *Proc. IEEE*, Vol. 58, Oct. 1970, pp. 1571-1577.
- [4] RCA Electro-Optics Handbook, Technical Series EOH-11, 1974, Chap. 7.
- [5] R. S. Kennedy, "Communications through Optical Scattering Channels: An Introduction," *Proc. IEEE*, Vol. 58, Oct. 1970, pp. 1651-1665.
- [6] R. S. Kennedy, "Low-Visibility Short-Haul Communication in the Atmosphere," Report of the NSF Grantee-User Semi-Annual Meeting on Optical Communications, Boulder, Colo., May 29-30, 1974.
- [7] J. R. Clark and J. R. Baird, "Optical Communication under Low-Visibility Conditions: Recent Experimental Results," in 1975 National Telecommun. Conf. Rec., Vol. 1, Dec. 1975, pp. 6-1 - 6-3.
- [8] S. R. Robinson, "Spatial Phase Compensation Receivers for Optical Communication," Ph.D. Thesis, Dept. of Elect. Eng. and Comput. Sci., M.I.T., Cambridge, May 1975.
- [9] R. M. Lerner and A. E. Holland, "The Optical Scatter Channel," *Proc. IEEE*, Vol. 58, Oct. 1970, pp. 1547-1563.
- [10] H. M. Heggstad, "Optical Communication through Multiple-Scattering Media," *Res. Lab. Electron., M.I.T., Cambridge, Tech. Rep. 472*, Nov. 22, 1968.
- [11] T. P. McGarty, "On the Structure of Random Fields Generated by Multiple Scatter Media," Ph.D. Thesis, Dept. of Elect. Eng., M.I.T., Cambridge, June 1971.
- [12] R. L. Fante, "Mutual Coherence Function and Frequency Spectrum of a Laser Beam Propagating through Atmospheric Turbulence," *J. Opt. Soc. Am.*, Vol. 64, May 1974, pp. 592-598.
- [13] A. Ishimaru and S. T. Hong, "Multiple Scattering Effects on Coherent Bandwidth and Pulse Distortion of a Wave Propagating in a Random Distribution of Particles," *Radio Science*, Vol. 10, June 1975, pp. 637-644.
- [14] R. S. Kennedy, Fading Dispersive Communication Channels, New York: Wiley, 1969.
- [15] J. H. Shapiro, "Optimal Power Transfer through Atmospheric Turbulence Using State Knowledge," *IEEE Trans. Commun. Technol.*, Vol. COM-19, Aug. 1971, pp. 410-414.

- [16] G. Q. McDowell, "Pre-distortion of Local Oscillator Wavefront for Improved Optical Heterodyne Detection through a Turbulent Atmosphere," Sc.D. Thesis, Dept. of Elect. Eng., M.I.T., Cambridge, April 1971.
- [17] J. W. Hardy, J. Feinleib, and J. C. Wyant, "Real-Time Phase Correction of Optical Imaging Systems," presented at the Opt. Soc. Am. Topical Meeting on Optical Propagation through Turbulence, Boulder, Colo., July 9-11, 1974.
- [18] E. A. Bucher, R. M. Lerner, and C. W. Niessen, "Some Experiments on the Propagation of Light Pulses through Clouds," Proc. IEEE, Vol. 58, Oct. 1970, pp. 1564-1567.
- [19] E. A. Bucher and R. M. Lerner, "Experiments on Light Pulse Communication and Propagation through Atmospheric Clouds," Appl. Opt., Vol. 12, Oct. 1973, pp. 2401-2414.
- [20] J. H. Shapiro, "Propagation Characteristics of Low-Visibility Atmospheres: An Experimental Program," Report of the NSF Grantee-User Semi-Annual Meeting on Optical Communications, Cambridge, Mass., June 8-9, 1976.
- [21] Air Force Electronic Systems Division Contract F19628-76-C-0054, "Coupled Measurements of Multipath and Angular Dispersion in Low-Visibility Optical Communication Channels."
- [22] National Science Foundation Grant ENG 74-00131-A01, "An Investigation of Optical Communication Systems for Low Visibility Communication."
- [23] M. S. Perlmutter, "Optimization of Multiply Sensitized Ho^{3+} : YLF as a Laser Material," S.M. Thesis, Dept of Elect. Eng. and Comput. Sci., M.I.T., Cambridge, Aug. 1975.
- [24] Woo H. Paik, "Operating Instructions for the 450 MHz Synchronization System," Res. Lab. of Electron., M.I.T., Cambridge, Internal Memorandum, Optical Propagation and Communication Group, Aug. 28, 1975.
- [25] E. A. Bucher, "Computer Simulation of Light Pulse Propagation for Communication through Thick Clouds," Appl. Opt., Vol. 12, Oct. 1973, pp. 2391-2400.
- [26] D. Deirmendjian, Electromagnetic Scattering on Spherical Polydispersions, New York: American Elsevier, 1969.
- [27] E. J. McCartney, Optics of the Atmosphere, New York: Wiley, 1976.
- [28] K. M. Case and P. F. Zweifel, Linear Transport Theory, Reading, Mass.: Addison-Wesley Publishing Co., 1967.
- [29] B. Davison and J. B. Sykes, Neutron Transport Theory, Oxford: Clarendon Press, 1957.
- [30] R. L. Rowell and R. S. Stein (Eds.), Electromagnetic Scattering, New York: Gordon and Breach, 1967.
- [31] R. D. Cox and H. D. Miller, The Theory of Stochastic Processes, New York: John Wiley and Sons, 1965.

- [32] E. Wong, Stochastic Processes in Information and Dynamical Systems, New York: McGraw-Hill Book Co., 1971.
- [33] K. M. Case, F. DeHoffmann, G. Placzek, Introduction to the Theory of Neutron Diffusion, Vol. I, Los Alamos Scientific Laboratory, Los Alamos, New Mexico, June 1953, U. S. Government Printing Office.

APPENDIX I

The task at hand is to evaluate Eq. (36) with $s = j\omega_m$ for $\omega_m > 0$. To this end it is convenient to restate that equation as

$$h(\vec{r}) = \frac{\exp(-\gamma r)}{4\pi r^2} + \frac{1}{\beta} \left(\frac{1}{2\pi}\right)^3 \int d\vec{\omega} \frac{\kappa^2(\omega)}{1 - \kappa(\omega)} \exp(j\vec{\omega} \cdot \vec{r}), \quad (\text{I-1})$$

where

$$\kappa(\omega) = \frac{\beta}{2j\omega} \ln \frac{\gamma + j\omega}{\gamma - j\omega} \quad (\text{I-2a})$$

or equivalently,

$$\kappa(\omega) = \frac{\beta}{\omega} \tan^{-1} \frac{\omega}{\gamma} \quad (\text{I-2b})$$

and γ equals $a + (j\omega_m/c)$. Here $\kappa(\vec{\omega})$ has been written as $\kappa(\omega)$ since it depends on $\vec{\omega}$ only through ω .

Upon expressing the integral in polar coordinates with \vec{r} as the zenith direction and evaluating the integrals on ϕ and θ , one obtains

$$h(\vec{r}) = \frac{2}{(2\pi)^2 \beta r} \int_0^\infty d\omega [\omega \sin(\omega r)] \frac{\kappa^2(\omega)}{1 - \kappa(\omega)} + \frac{\exp(-\gamma r)}{4\pi r^2}.$$

Since $\kappa(\vec{\omega})$ is defined and analytic in the strip $|\text{Im } \omega| < \text{Re } \gamma$, and since both $\omega \sin \omega r$ and $\kappa(\vec{\omega})$ are even functions of ω , this may also be written as

$$h(\vec{r}) = \frac{1}{(2\pi)^2 j\beta r} \int_{-\infty}^\infty d\omega \frac{\omega \kappa^2(\omega)}{1 - \kappa(\omega)} \exp(j\omega r) + \frac{\exp(-\gamma r)}{4\pi r^2}. \quad (\text{I-3})$$

The integral can be further reduced by contour integration in the complex ω plane. To that end, note that $\kappa(\omega)$, continued beyond the strip $|\text{Im } \omega| < a$, is analytic in the whole upper half-plane except for a branch point at $\omega = \gamma$ and for isolated poles at the zeros of $1 - \kappa(\omega)$. Moreover, $\omega \kappa^2(\omega)/[1 - \kappa(\omega)]$ vanishes as the imaginary part of ω goes to infinity. Thus the integral around the contour in the cut plane shown in Fig. I-1 equals the sum of the integral I_1 along the

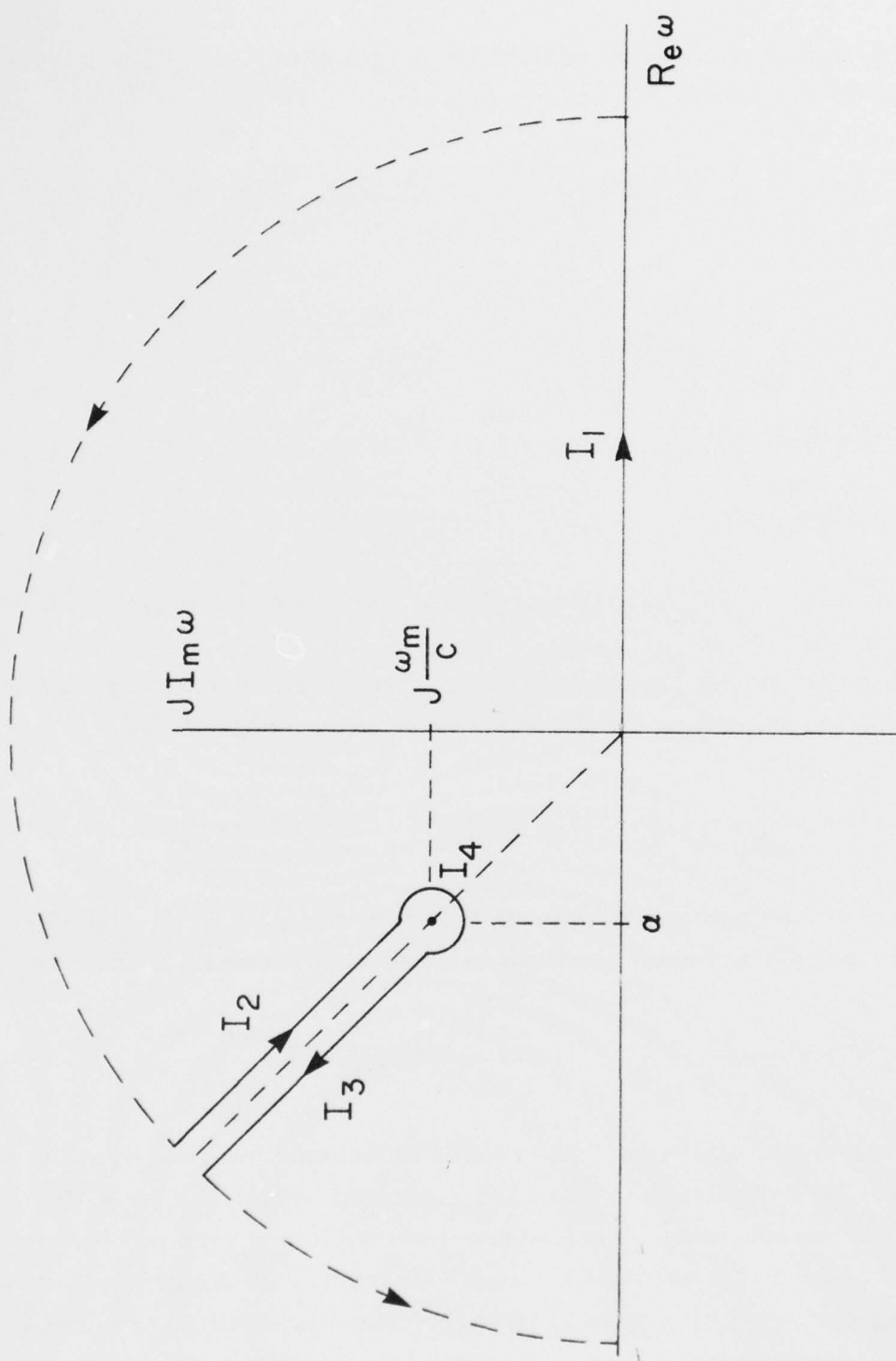


Fig. I-1. Contour of integration in the cut plane.

real ω axis, the integrals I_2 and I_3 along the cut and the integral I_4 around the branch point. Furthermore, the integral I_4 can be shown to vanish. Thus the integral around the contour reduces to $I_1 + I_2 + I_3$ where I_1 is the integral appearing in Eq. (I-3). This contour integral equals $2\pi j$ times the sum of the residues of the integrand. Thus

$$h(\vec{r}) - \frac{\exp(-\gamma r)}{4\pi r^2} = (I_2 + I_3) + 2\pi j \sum \text{Residue}(\omega_p) \quad (\text{I-4})$$

where the sum is over the poles, ω_p , of the integrand within the contour.

The integrals I_2 and I_3 differ only in that they are on opposite sides of the cut and are in opposite directions. When they are added one obtains

$$I_2 + I_3 = \frac{-\gamma}{4\pi r} \int_1^\infty dv \frac{\left\{ \left[1 - \frac{\beta}{\gamma v} \coth^{-1} v \right]^2 + \left(\frac{\pi\beta}{2\gamma v} \right)^2 - 1 \right\}}{\left[1 - \frac{\beta}{\gamma v} \coth^{-1} v \right]^2 + \left(\frac{\pi\beta}{2\gamma v} \right)^2} \exp(-\gamma r v)$$

or

$$I_2 + I_3 = -\frac{\exp(-\gamma r)}{4\pi r^2} + \frac{\gamma}{4\pi r} \int_1^\infty dv \left\{ \left[1 - \frac{\beta}{\gamma v} \coth^{-1} v \right]^2 + \left(\frac{\pi\beta}{2\gamma v} \right)^2 \right\}^{-1} \exp(-\gamma r v).$$

For ω_m equal to zero the last integral is essentially one encountered by Case et al. [1]. Following them we define

$$\epsilon(ar, j\omega_m) = \gamma r (\exp ar) \int_1^\infty dv \left\{ \left[1 - \frac{\beta}{\gamma v} \coth^{-1} v \right]^2 + \left(\frac{\pi\beta}{2\gamma v} \right)^2 \right\}^{-1} \exp(-\gamma r v) \quad (\text{I-5})$$

and write

$$I_2 + I_3 = -\frac{\exp(-\gamma r)}{4\pi r^2} + \frac{\epsilon(ar, j\omega_m)}{4\pi r^2} \exp(-ar). \quad (\text{I-6})$$

The function $\epsilon(ar, 0)$ is identical to the function $\epsilon(ar)$ used by Case [1].

It remains to evaluate the residue term in Eq. (I-4). The poles are the upper half-plane zeros ω_p of $1 - \kappa(\omega)$, i.e., they are the solutions of

$$\frac{1}{2(j\omega_p/\gamma)} \ln \frac{1 + (j\omega_p/\gamma)}{1 - (j\omega_p/\gamma)} = \frac{\gamma}{\beta} \quad (\text{I-7})$$

for which $\text{Im } \omega_p$ is positive. The number of such solutions is given by the number of times the γ/β point in the complex plane is encircled by the locus of $[2j(\omega/\gamma)^{-1} \ln \{ [1 - j(\omega/\gamma)] / [1 - (j\omega/\gamma)] \}]$ as ω varies around the contour shown in Fig. I-1. That locus has the general shape shown in Fig. I-2. Thus there will be one upper plane solution of Eq. (I-7) if γ/β falls in the shaded area and none if it does not.

There is always a solution when ω_m equals zero since γ/β is then real and positive and hence is contained in the shaded area. More generally, a solution will exist for small values of ω_m but not for large values. The transition occurs when ω_m is such that the point γ/β lies on the locus shown in Fig. I-2. The value of ω_m for which this occurs will be denoted by ω_c . It is the value of ω_m for which the solution ω_p of Eq. (I-7) lies on the left side of the cut in Fig. I-1. Thus ω_c is the real nonnegative solution of Eq. (I-7) for some ν greater than 1 when ω_p equals $j\nu$. Specifically,

$$-\frac{1}{2\nu} \ln \frac{1-\nu}{1+\nu} = \frac{\alpha}{\beta} + j \frac{\omega_c}{\beta c} \quad \text{with } \nu > 1$$

or

$$\frac{1}{2\nu} \ln \frac{\nu+1}{\nu-1} + \frac{j\pi}{2\nu} = \frac{\alpha}{\beta} + j \frac{\omega_c}{\beta c},$$

where the branch of the logarithm has been chosen to be on the left side of the cut. The imaginary part of this equation implies that

$$\frac{\pi}{2\nu} = \frac{\omega_c}{\beta c}. \quad (\text{I-8})$$

Using this result to eliminate ν from the real parts of the equation yields

$$\frac{\alpha}{\beta} \left(\frac{\pi\beta c}{2\omega_c} \right) = \frac{1}{2} \ln \frac{(\pi\beta c)/(2\omega_c) - 1}{(\pi\beta c)/(2\omega_c) + 1}$$

or, equivalently,

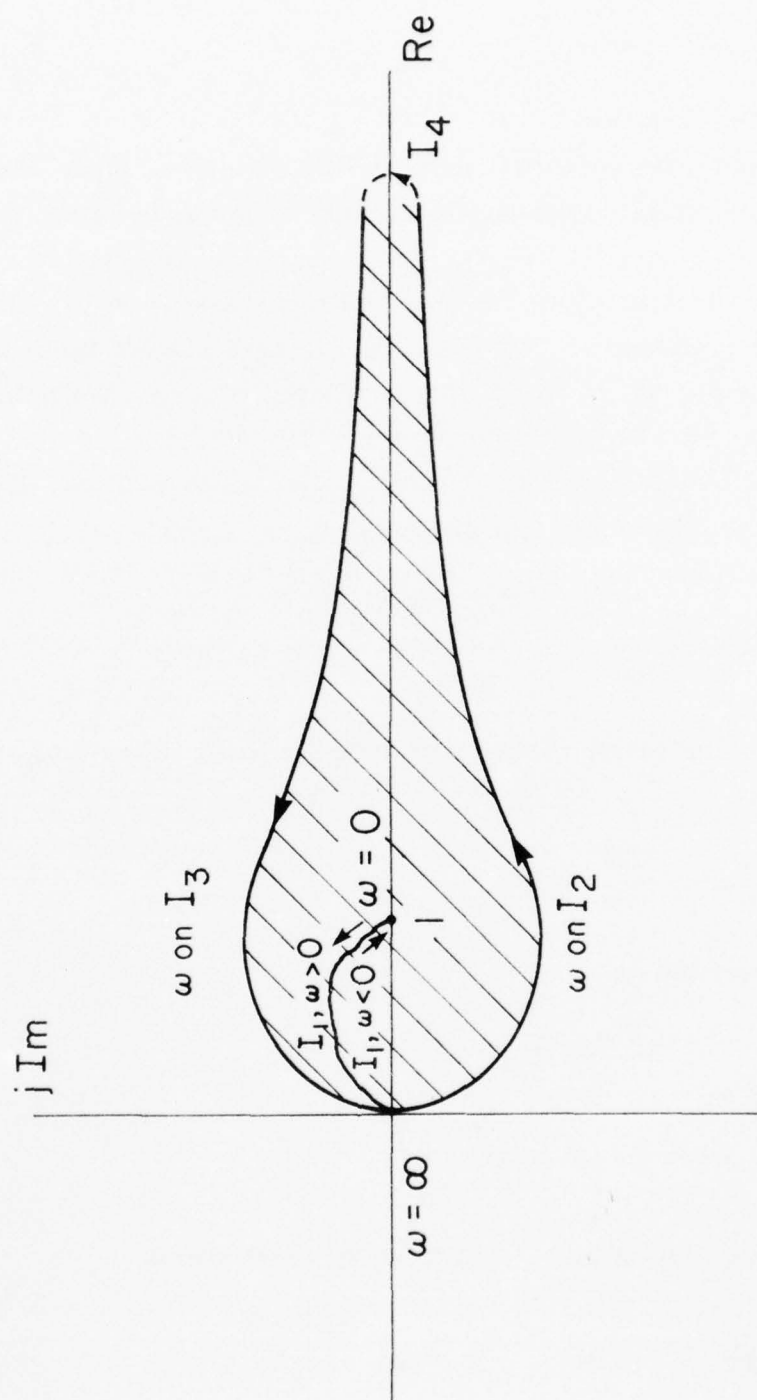


Fig. I-2. Locus of $[2j(\omega/\gamma)]^{-1} \ln \{[1 + (j\omega/\gamma)]/[1 - (j\omega/\gamma)]\}$ for ω on the contour of Fig. I-1.

$$\frac{\beta}{\alpha} \left(\frac{\pi a c}{2 \omega_c} \right) = \coth \left(\frac{\pi a c}{2 \omega_c} \right). \quad (I-9)$$

This is the defining equation for ω_c .

Since the hyperbolic cotangent varies from infinity to unity, Eq. (I-9) will possess a single positive solution. Thus there is a single value, ω_c , of ω_m for which the γ/β point in Fig. I-2 lies on the boundary of the shaded region. For all smaller values it lies within the shaded region, and $1 - \kappa(\omega)$ possesses a single upper half-plane zero. For all larger values the γ/β point is outside the shaded region and there is no upper half-plane zero. We note in passing that when $\omega_m = \omega_c$ the zero ω_p is located at $(\pi\beta\gamma c)/(2\omega_c)$.

It remains to evaluate the residue of ω_p that appears in Eq. (I-4). Since ω_p is a simple pole, its residue is given by

$$\text{Res } (\omega_p) = \frac{1}{(2\pi)^2 j\beta r} \frac{\omega_p^2 \kappa^2(\omega_p) \exp(j\omega_p r)}{-\kappa'(\omega_p)},$$

where $\kappa'(\omega)$ is the derivative of $\kappa(\omega)$ with respect to ω . Since $\kappa(\omega_p) = 1$ and since

$$\kappa'(\omega) = -\frac{1}{\omega} \kappa(\omega) + \frac{\gamma\beta}{\omega} \frac{1}{\gamma^2 + \omega^2},$$

this can also be written as

$$\text{Res } (\omega_p) = \frac{\omega_p^2 \exp(j\omega_p r)}{(2\pi)^2 j\beta r \left[1 - \frac{\gamma\beta}{\gamma^2 + \omega_p^2} \right]}. \quad (I-10)$$

Introducing Eqs. (I-6) and (I-10) into Eq. (I-4) yields

$$h(\vec{r}) = \frac{A(\omega_m)}{2\pi r} \exp(j\omega_p r) + \epsilon(ar, j\omega_m) \frac{\exp(-ar)}{4\pi r^2},$$

where

$$A(\omega_m) = \begin{cases} \frac{\omega_p^2}{\beta \left[1 - \frac{\beta \gamma}{\gamma^2 + \omega_p^2} \right]} & \text{for } 0 \leq \omega_m < \omega_c \\ 0 & \text{for } \omega_m > \omega_c \end{cases}$$

and $\epsilon(\omega, \omega_m)$, ω_p , and ω_c are given by Eqs. (I-5), (I-7), and (I-9).

References

- [1] K. M. Case, F. DeHoffmann, G. Placzek, Introduction to the Theory of Neutron Diffusion, Vol. I, Los Alamos Scientific Laboratory, Los Alamos, New Mexico, June 1953, U. S. Government Printing Office.

METRIC SYSTEM

BASE UNITS:

Quantity	Unit	SI Symbol	Formula
length	metre	m	...
mass	kilogram	kg	...
time	second	s	...
electric current	ampere	A	...
thermodynamic temperature	kelvin	K	...
amount of substance	mole	mol	...
luminous intensity	candela	cd	...

SUPPLEMENTARY UNITS:

plane angle	radian	rad	...
solid angle	steradian	sr	...

DERIVED UNITS:

Acceleration	metre per second squared	...	m/s
activity (of a radioactive source)	disintegration per second	...	(disintegration)/s
angular acceleration	radian per second squared	...	rad/s
angular velocity	radian per second	...	rad/s
area	square metre	...	m
density	kilogram per cubic metre	...	kg/m
electric capacitance	farad	F	A·s/V
electrical conductance	siemens	S	A/V
electric field strength	volt per metre	...	V/m
electric inductance	henry	H	V·s/A
electric potential difference	volt	V	W/A
electric resistance	ohm	...	V/A
electromotive force	volt	V	W/A
energy	joule	J	N·m
entropy	joule per kelvin	...	J/K
force	newton	N	kg·m/s
frequency	hertz	Hz	(cycle)/s
illuminance	lux	lx	lm/m
luminance	candela per square metre	...	cd/m
luminous flux	lumen	lm	cd·sr
magnetic field strength	ampere per metre	...	A/m
magnetic flux	weber	Wb	V·s
magnetic flux density	tesla	T	Wb/m
magnetomotive force	ampere	A	...
power	watt	W	J/s
pressure	pascal	Pa	N/m
quantity of electricity	coulomb	C	A·s
quantity of heat	joule	J	N·m
radiant intensity	watt per steradian	...	W/sr
specific heat	joule per kilogram-kelvin	...	J/kg·K
stress	pascal	Pa	N/m
thermal conductivity	watt per metre-kelvin	...	W/m·K
velocity	metre per second	...	m/s
viscosity, dynamic	pascal-second	...	Pa·s
viscosity, kinematic	square metre per second	...	m/s
voltage	volt	V	W/A
volume	cubic metre	...	m
wavenumber	reciprocal metre	...	(wave)/m
work	joule	J	N·m

SI PREFIXES:

Multiplication Factors	Prefix	SI Symbol
1 000 000 000 000 = 10 ¹²	tera	T
1 000 000 000 = 10 ⁹	giga	G
1 000 000 = 10 ⁶	mega	M
1 000 = 10 ³	kilo	k
100 = 10 ²	hecto*	h
10 = 10 ¹	deka*	da
0.1 = 10 ⁻¹	deci*	d
0.01 = 10 ⁻²	centi*	c
0.001 = 10 ⁻³	milli	m
0.000 001 = 10 ⁻⁶	micro	μ
0.000 000 001 = 10 ⁻⁹	nano	n
0.000 000 000 001 = 10 ⁻¹²	pico	p
0.000 000 000 000 001 = 10 ⁻¹⁵	femto	f
0.000 000 000 000 000 001 = 10 ⁻¹⁸	atto	a

* To be avoided where possible

*MISSION
of
Rome Air Development Center*

RADC plans and conducts research, exploratory and advanced development programs in command, control, and communications (C³) activities, and in the C³ areas of information sciences and intelligence. The principal technical mission areas are communications, electromagnetic guidance and control, surveillance of ground and aerospace objects, intelligence data collection and handling, information system technology, ionospheric propagation, solid state sciences, microwave physics and electronic reliability, maintainability and compatibility.

